Inaugural – Dissertation

zur
Erlangung der Doktorwürde

der
Naturwissenschaftlich - Mathematischen
Gesamtfakultät

der
Ruprecht - Karls - Universität
Heidelberg

vorgelegt von

Dipl.–Phys. Kim Dieter Kreim
geb. Brück
aus Wiesbaden

Tag der mündlichen Prüfung: 16. Juli 2013

Collinear Laser Spectroscopy of Potassium

Nuclear Charge Radii beyond $N = 28$

Gutachter: Prof. Dr. Klaus Blaum
Prof. Dr. Selim Jochim

Zusammenfassung

Grundzustandseigenschaften geben Aufschluss über die Struktur von Kernen. Dazu gehören Spin, Ladungsradius, magnetisches Dipol- und elektrisches Quadrupolmoment. Die Interpretation der gemessenen Größen innerhalb des Schalenmodells erlaubt eine detaillierte Beschreibung der zugrunde liegenden Struktur sowie der Grundzustandswellenfunktion. Im Vergleich mit modernen mikroskopischen Modellen können Vorhersagen für Spin und Ladungsradius getestet werden. Großes Interesse besteht an der Untersuchung der Nuklidkarte im Bereich der magischen Protonenzahl $Z = 20$, zu denen die Messungen dieser Arbeit beitragen. Die neuen Ergebnisse wurden am COLLAPS Experiment zur kollinearen Laserspektroskopie gewonnen, welches sich am Isotopenseparator ISOLDE am CERN befindet. Die Methode der "bunched-beam" Laserspektroskopie erlaubte zum ersten Mal die Vermessung der Hyperfeinstruktur der Kaliumisotope mit Massenzahl $A = 48 - 51$.

Der Spin des Grundzustands sowie die Isotopieverschiebung der untersuchten Isotope $^{48-51}$K konnten extrahiert und deren Einfluss auf die Entwicklung des $\pi d_{3/2}$ Orbitals jenseits des Schalenabschlusses bei der magischen Neutronenzahl $N = 28$ untersucht werden. Ladungsradien dieser Arbeit liefern Erkenntnisse über das systematische Verhalten der Ladungsradien im Bereich um Calcium. Während theoretische Modelle korrekte Vorhersagen über den Spin des Grundzustands machen, weisen Rechnungen auf dem neuesten Stand der relativistischen Hartree-Fock oder "Coupled-Cluster" Methode große Diskrepanz untereinander und zu diesen Daten auf.

Abstract

Nuclear ground-state properties, such as spin, charge radius, and magnetic dipole and electric quadrupole moments are important quantities to describe the nucleus. The comparison of experimental data to shell-model calculations gives insight in the underlying nuclear structure and composition of ground-state wave functions. Spins and charge radii can also be used to test the predictions of state-of-the-art microscopic models. This work contributes to these studies providing new measurements in the region of the nuclear chart around the magic proton number $Z = 20$. The data have been obtained at the collinear laser spectroscopy setup COLLAPS located at the radioactive-ion-beam facility ISOLDE at CERN. Using bunched-beam laser spectroscopy hyperfine structure spectra of the potassium isotopes with mass number $A = 48 - 51$ could be recorded for the first time.

Ground-state spins and isotope shifts could be deduced for $^{48-51}$K contributing to the evolution of the $\pi d_{3/2}$ orbital beyond the shell closure at the magic neutron number $N = 28$. Charge radii deduced from isotope shifts provide information towards the systematics of the charge radii in the calcium region beyond the $N = 28$ shell closure. While theoretical calculations predict the correct spins, the charge radii still provide a challenge even to the newest relativistic mean-field and coupled cluster models.

Contents

List of Figures

List of Tables

1 Motivation

High-resolution laser spectroscopy provides model-independent information on nuclear ground-state properties. Being fingerprints of the nucleus, the atomic hyperfine structure and isotope shift cast light on the underlying nuclear structure. Studying chains of isotopes yields structural information upon adding or removing neutrons. It can thus give insight in the behavior of nuclear ground-state properties at so called magic numbers or shell closures, at which nuclei generally are strongly bound and spherical. Likewise, changes in the shape of the nucleus can also be extracted. As the observables are obtained model-independently, a comparison with theory can, on the one hand, help to interpret experimental observations. Of special interest is the structural evolution far from the valley of β-stability. With growing neutron-to-proton asymmetry the structure of nuclei can change such that shell closures vanish or new magic numbers emerge. As model calculations diverge the more one advances from stability where knowledge of ground-state properties is scarce or non-existent, data on complementary observables are important. The data, on the other hand, can be used to test the validity of a theoretical description and in some cases test its predictive power. What theoretical model to choose depends highly on the mass region and covers a wide range of possibilities from phenomenological liquid drop or shell-model calculations to mean-field or ab-initio methods. High-resolution laser spectroscopy can in a unique way reveal properties on the nuclear level such as charge radii of the element under investigation using known atomic properties. While the atomic hyperfine structure (HFS) gives information on the spin and moments of the nucleus, the measured isotope shift (IS) is sensitive to small differential changes in size and shape of the nuclear charge distribution. Collinear laser spectroscopy (CLS) has proven to be the method of choice for the study of radioactive beams for more than three decades [1, 2]. Information on the development of CLS in general and focused on the recent developments at the collinear laser spectroscopy beam line COLLAPS at ISOLDE can be found in the following list of reviews [1–13].

Figure 1.1 gives an overview of the isotopes studied by optical spectroscopy. The plot is taken from the web site of the laser-spectroscopy group at the University of Mainz [14] and contains data published until 2012. It is evident from figure 1.1 that most of the data are available in the medium to heavy-mass region between Cu and Ra with some gaps. Here, long chains of charge radii have been studied to test theoretical models like the droplet model [15]. In the light-mass region starting from H up to Be, charge radii have been measured and compared with theoretical models, such as the no-core shell model (NCSM), fermionic molecular dynamics (FMD) and Greens Function Monte Carlo (GFMC) calculations [16–20]. In the medium-mass region, Ne to Fe, charge-radii data exist with theoretical calculations for Ne (FMD and Hartree-Fock) [21,22], Na (Hartree-Fock) [23], Mg (FMD) [24], Ar (Zamick-Talmi formula and spherical SGII Skyrme-type

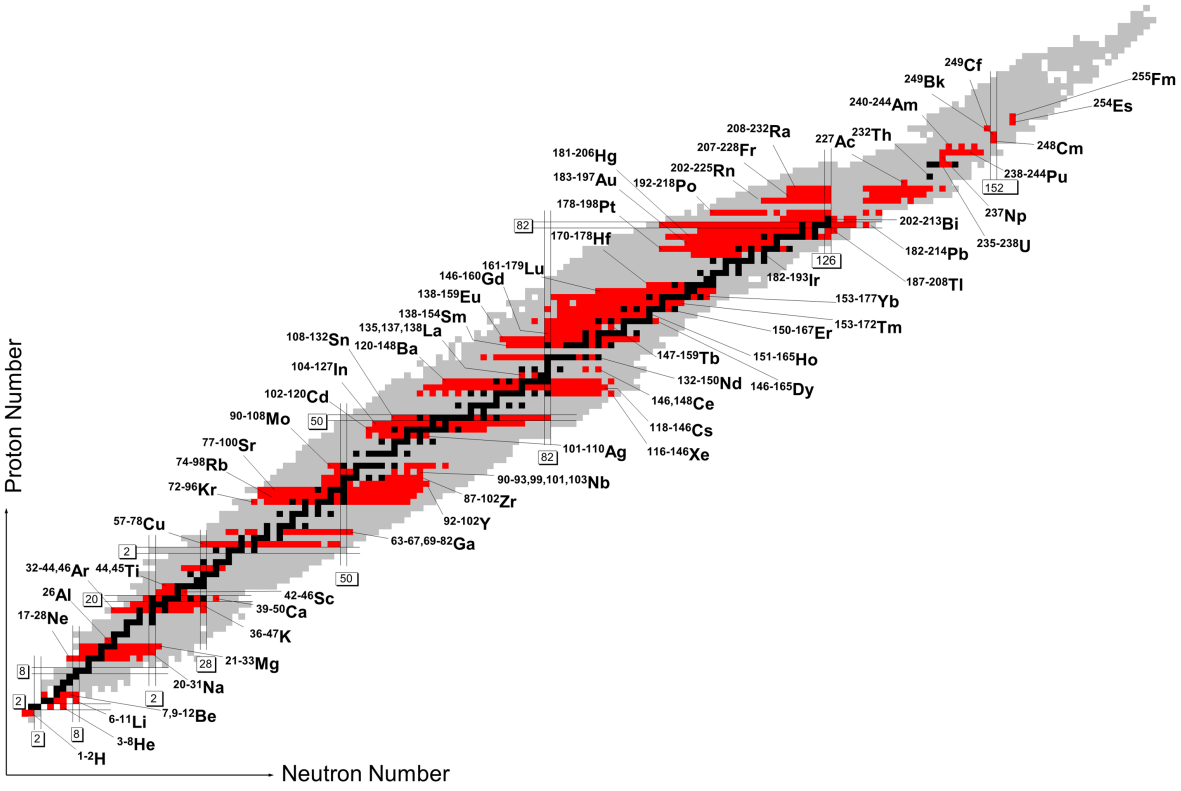

Figure 1.1: Chart of nuclides taken from Ref. [14]. Black squares represent stable nuclei. The light gray area indicates those nuclei which are known to exist. The neutron and proton shell closures are marked by double straight lines and the magic numbers are given in boxes. Red squares represent those isotopes which have been investigated by optical spectroscopy.

Hartree-Fock) [25], Ca (shell model [26]) [27–29], Sc (Zamick-Talmi formula) [30], and Ti (relativistic mean field [31,32]) [33]. For the odd-proton elements K [34,35] and Mn [36] no theoretical approach exists.

Figure 1.2 shows the root mean square (RMS) nuclear charge radii for the isotopes of elements with Z = 18-26, except Z = 23. The data for Cr was taken from [37] and for Fe from [38]. As a general trend, charge radii increase with proton number Z and with neutron number N. Yet, upon adding neutrons, the neutron magic numbers play an important role. All of the isotopic chains exhibit a decrease in the charge radius towards the neutron shell closure at N = 28. This illustrates the fact that nuclei are more bound and spherical at closed shells. The behavior of the charge radii in the Ca region is discussed in publications of Blaum *et al.* [25], Angeli *et al.* [39] and Avgoulea *et al.* [30]. Here, the main point is the difference in the specific behavior of the radii with changing proton number, from Ar(Z=18) to Ti(Z=22). In a shell-model picture [40,41], the nucleons are described as occupying different shells or orbitals, in analogy to the electron orbitals in atomic physics used to classify the elements on the periodic chart, for example. In the calcium region, Z = 20 marks the filling of all proton shells up to

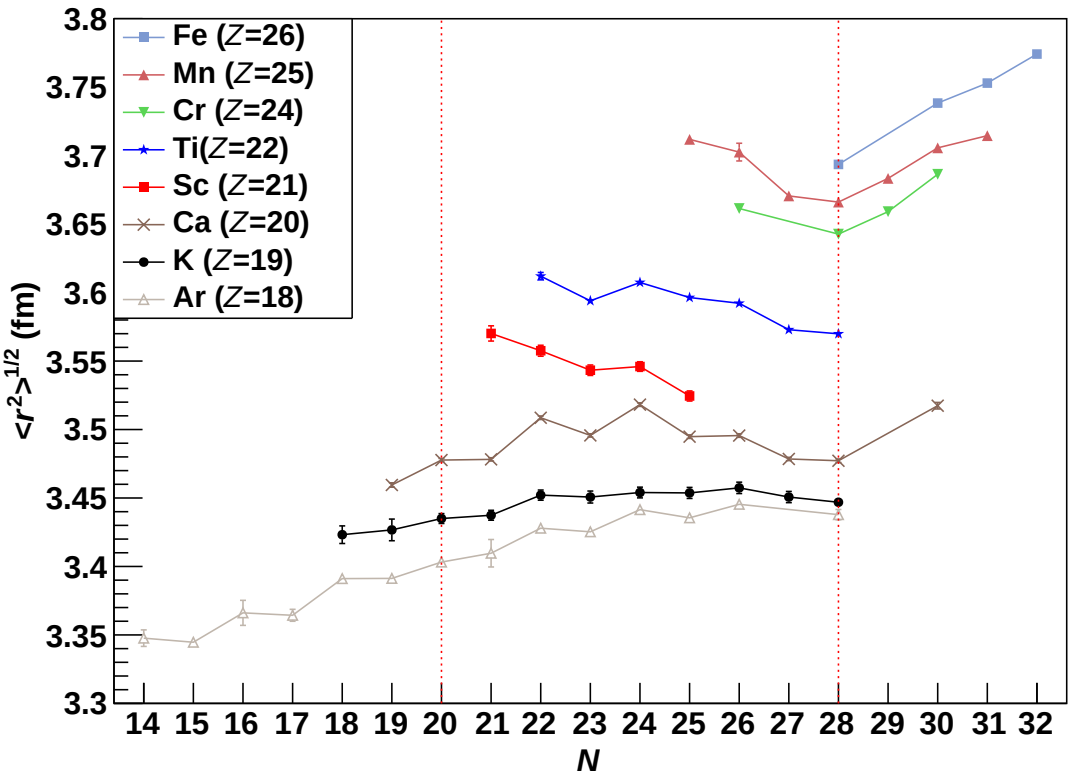

Figure 1.2: RMS nuclear charge radii versus neutron number for the isotopes of Ar, K, Ca, Sc, Ti, Cr, Mn and Fe. For details see text.

$\pi 1d_{3/2}$ and $N = 20$ the respective neutron shell $\nu 1d_{3/2}$. Existing high-resolution data cover the full neutron $f_{7/2}$ shell ($\nu f_{7/2}$) from $N = 21$ to $N = 28$, but only few charge radii have been measured for isotopes in the $\nu p_{3/2}$ shell ($N = 29$ to $N = 32$) on the neutron-rich side of the valley of stability. Furthermore, substantial structural changes are predicted in this region including the inversion and subsequent re-inversion of the $\pi 2s_{1/2}$ and $\pi 1d_{3/2}$ shell-model orbitals and the development of an $N = 32$ sub-shell closure as discussed in [42–44]. Whilst theoretical models of charge radii across the $\nu f_{7/2}$ have been reasonably successful in describing the observed trends, little is known about how this observable would be influenced by the anticipated structural evolution in the region beyond $N = 28$.

The inversion of the odd-A potassium nuclear ground-state spins from $I = 3/2^+$ ($\pi d_{3/2}$) in $^{39-45}$K to $I = 1/2^+$ ($\pi s_{1/2}$) for ^{47}K ($N = 28$) was reported by Touchard *et al.* [34] in 1982 and has subsequently been reproduced by the shell-model and mean-field calculations [45–47]. The parity is in both cases positive, indicated by the +.

Figure 1.3 shows the evolution of the experimental energy of the first excited state in the odd-K isotopes with respect to the $3/2^+$ ground state. Up to ^{45}K the first excited state has spin 1/2 and positive parity. At ^{47}K, the levels invert and the $1/2^+$ becomes

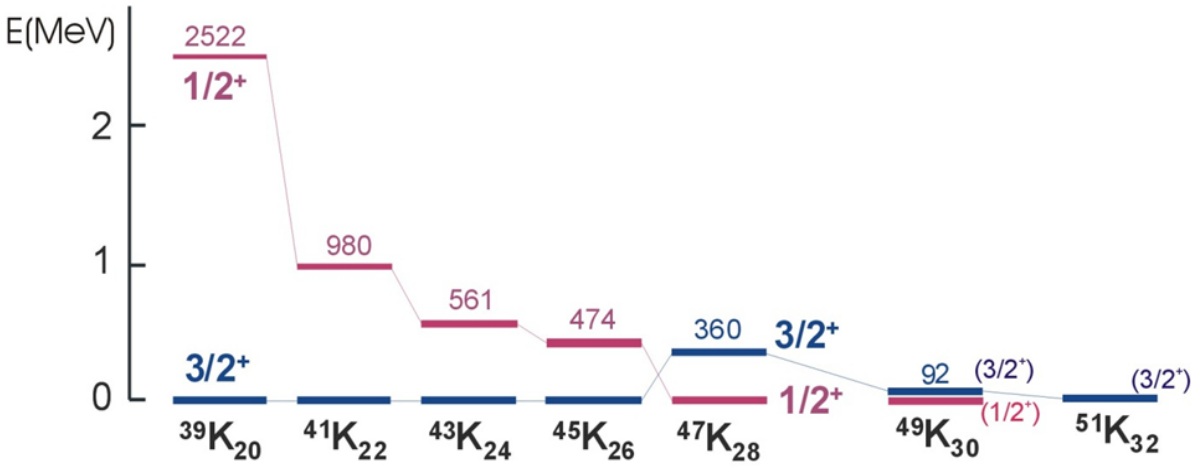

Figure 1.3: Evolution of the experimental energy of the first excited state ($1/2^+$ up to ^{45}K) with respect to the $3/2^+$ ground-state in the odd-K isotopes. Data up to ^{47}K were taken from [47], and for ^{49}K from [48]. For ^{51}K no excited states are known but β-decay studies suggest a ground-state with spin 3/2 and positive parity [49].

the ground state [34,47]. In the case of ^{49}K, experimental data confirm the inversion [48] while for ^{51}K a re-inversion is predicted [49]. A firm assignment of the ground-state spins of $^{48-51}$K is required to solve the contradictory assignments found in decay-spectroscopy data [48–54].

This work will focus on the measurement of the hyperfine structures of potassium isotopes $^{38,39,42,44,46-51}$K and the extracted spins and changes in mean square charge radii $\delta\langle r^2\rangle$. In chapter 2, the theory of hyperfine structure and optical isotope shifts, the basics of collinear laser spectroscopy and a short discussion on line shapes of optical transitions will be introduced. In chapter 3, the infrastructure used will be presented, the ISOLDE facility at CERN, the collinear laser spectroscopy setup COLLAPS, the laser systems, the new light-collection chamber, and the data acquisition system. In chapter 4, details are given on the two measurement campaigns including the observed line shapes and voltage calibrations by using existing isotope shift data. The assignment of the ground-state spins, the measured isotope shifts (IS), and A-factors extracted from the HFS will be discussed in chapter 5. In addition, the $\delta\langle r^2\rangle$ calculated from the measured isotope shifts and the calculated RMS charge radii ($\sqrt{\langle r^2\rangle}$) will be presented. In chapter 6, the evolution of the $\pi d_{3/2}$ level will be discussed with the measured ground-state spins. The extracted $\delta\langle r^2\rangle$ and $\sqrt{\langle r^2\rangle}$ values of potassium will be compared to the trends known in the Ca region. The last chapter will summarize the information obtained on the nuclear ground-state properties and provide an outlook on further measurements in the Ca region.

2 Basic Concepts of Laser Spectroscopy

When optical transitions are observed with an energy resolution better than 10^{-6}, it is found that the finite size, spin, magnetic dipole moment and electric quadrupole moment of the nucleus perturb the observed spectra. As the spin, magnetic dipole moment and electric quadrupole moment of a single isotope are responsible for its hyperfine structure, they also determine the specific shape of the hyperfine spectrum. The isotope shift (IS) in turn results from the finite size and mass of the nucleus. Since it depends on the number of nucleons, the IS can only be extracted by observing the differences along the isotopic chain of one element ($Z = const.$). By studying optical transitions with laser spectroscopy, the natural line width of the respective transition will be altered to some extend. The conditions of collinear laser spectroscopy thus have to be taken into account to determine the line profile best suited to describe the measured spectra. Finally, the nuclear properties can be extracted by combining the theoretical line shape resulting from the atomic hyperfine structure and the optical isotope shift with the well-understood experimental data.

2.1 Atomic Hyperfine Structure

The total angular momentum of the nucleus $\boldsymbol{I}$, with the quantum number I called the nuclear spin, is associated with the nuclear magnetic dipole moment $\boldsymbol{\mu}_I$

$$\boldsymbol{\mu}_I = \frac{g_I \mu_N \boldsymbol{I}}{\hbar} \tag{2.1}$$

with g_I being the nuclear g-factor and μ_N the nuclear magneton

$$\mu_N = \frac{e\hbar}{2m_p} = \frac{m_e}{m_p}\mu_B. \tag{2.2}$$

Here, m_e and m_p denote the electron and proton mass, respectively, and $\hbar$ Planck's constant. The electrons induce a magnetic field $\boldsymbol{B}_J$ at the nucleus which interacts with the magnetic moment $\boldsymbol{\mu}_I$. This results in a coupling of the angular momenta of the electrons $\boldsymbol{J}$ and of the nucleus $\boldsymbol{I}$ to a new angular momentum $\boldsymbol{F} = \boldsymbol{J} + \boldsymbol{I}$ analog to $\boldsymbol{LS}$ coupling for electrons. The quantum number F of the combined angular momentum $\boldsymbol{F}$ can take values according to the triangular condition $F = J+I, J+I-1 ... |J-I|$. The hyperfine interaction removes the degeneracy of the different F levels and produces a

splitting into $2J+1$ or $2I+1$ hyperfine-structure levels for $J < I$ and $J > I$, respectively. The additional energy V_{HFS} due to the hyperfine interaction is

$$V_{HFS} = -\boldsymbol{\mu}_I \cdot \boldsymbol{B}_J. \tag{2.3}$$

Following [55], this results in the energy ΔE_{HFS} of the magnetic hyperfine interaction

$$\Delta E_{HFS} = \frac{A}{2}[F(F+1) - I(I+1) - J(J+1)] \equiv \frac{A}{2}C \tag{2.4}$$

with the hyperfine constant or A-factor

$$A = \frac{g_I \mu_N B\hbar}{J}. \tag{2.5}$$

Figure 2.1 gives an example of the hyperfine splitting for a level with $I = 3/2$ and $J = 3/2$. Indicated is the splitting ΔE between hyperfine levels, which can be calculated

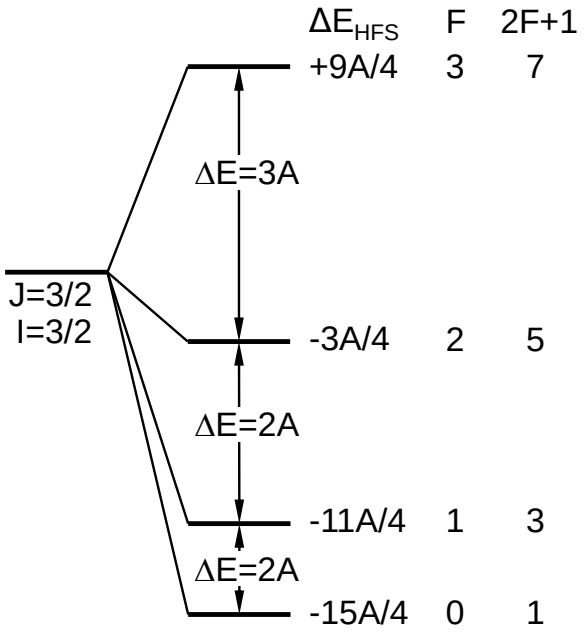

Figure 2.1: Example of hyperfine splitting for a level with I=3/2 and J=3/2. Given is the hyperfine Energy ΔE_{HFS}, the quantum number F, the multiplicity of the hyperfine levels and the splitting ΔE between the hyperfine levels in terms of A.

from Eq. (2.4) to

$$\Delta E_{F+1} - \Delta E_F = \Delta E = A(F+1). \tag{2.6}$$

Also given is the hyperfine energy ΔE_{HFS} in terms of A, the quantum number F and the multiplicity of the magnetic sub levels m_F, which are $(2F+1)$-times degenerate

in absence of an external magnetic field. The intensities of the individual peaks in the optical hyperfine spectrum are proportional to $(2F+1)$. Since in most cases both levels have hyperfine splitting the optical spectrum is more complicated and the relative intensities can be calculated using Eq. (2.16).

If the nucleus exhibits an electric quadrupole moment the energies of the hyperfine levels are additionally shifted. The electric field gradient induced by the electrons then interacts with the electric quadrupole moment resulting in an energy shift of

$$\Delta E_{Q_e} = B\frac{3C(C+1) - 4I(I+1)J(J+1)}{8I(2I-1)J(2J-1)}, \tag{2.7}$$

where $B = eQ_e\left\langle \frac{\delta^2 V_e}{\delta z^2}\right\rangle$ defines the electric quadrupole interaction constant Q_e with the electric field gradient $\langle \delta^2 V_e/\delta z^2\rangle$. Equation (2.7) is non zero only if $I, J \geq 1$. In the presented potassium data we used the D1 transition from the $4s^2S_{1/2} \rightarrow 4p^2P_{1/2}$ level which is a $J_g = 1/2 \rightarrow J_e = 1/2$ transition and therefore has no electric hyperfine structure. The analysis is done only with Eq. (2.4).

The probability for spontaneous emission from an excited state $|i\rangle$ to a final state $|f\rangle$ is given by the Einstein coefficient $\mathcal{A}_{if}$, which is connected to the lifetime of the excited state (for the used D1 line in K the $p_{1/2}$ state has a lifetime of $\tau \approx 26.3\,\mathrm{ns}$ [56]) via $\mathcal{A}_{if} = 1/\tau_i$. If the decay is possible into a number of final states $|f_j\rangle$ this changes to the sum of the partial $\mathcal{A}_{ij}$

$$\sum_j \mathcal{A}_{ij} = \sum_j \frac{1}{\tau_{ij}} = \frac{1}{\tau_i}. \tag{2.8}$$

The decay rate between the magnetic components $|JIFM\rangle$ of the hyperfine structure is given by [57, 58]

$$\mathcal{A}_{if} = C\nu^3 \left|\left\langle J_f I F_f M_f \left|\hat{D}_{\lambda\mu}\right| J_i I F_i M_i\right\rangle\right|^2, \tag{2.9}$$

where $\hat{D}_{\lambda\mu}$ ($\lambda = 1, \mu = M_f - M_i$) represents the spherical components of the electric dipole moment $\boldsymbol{D}$ and $C = 4(2\pi)^3/(3c^3\hbar)$. Applying the Wigner-Eckart theorem

$$\left|\left\langle J_f I F_f M_f \left|\hat{D}_{1\mu}\right| J_i I F_i M_i\right\rangle\right|^2 = \begin{pmatrix} F_f & 1 & F_i \\ -M_f & \mu & M_i \end{pmatrix}^2 \left|\left\langle J_f I F_f \left\|\hat{D}_1\right\| J_i I F_i\right\rangle\right|^2 \tag{2.10}$$

and using the reduced matrix element

$$\left|\left\langle J_f I F_f \left\|\hat{D}_1\right\| J_i I F_i\right\rangle\right|^2 = (2F_i+1)(2F_f+1) \times \begin{Bmatrix} J_f & F_f & I \\ F_i & J_i & 1 \end{Bmatrix}^2 \left|\left\langle J_f \left\|\hat{D}_1\right\| J_i\right\rangle\right|^2, \tag{2.11}$$

one finds the expression for $\mathcal{A}_{if}$ that can be summed over all final states

$$\mathcal{A}_{if} = C\nu^3 \left|\left\langle J_f \left\|\hat{D}_1\right\| J_i\right\rangle\right|^2 \times (2F_i+1)(2F_f+1) \begin{pmatrix} F_f & 1 & F_i \\ -M_f & \mu & M_i \end{pmatrix}^2 \begin{Bmatrix} J_f & F_f & I \\ F_i & J_i & 1 \end{Bmatrix}^2. \tag{2.12}$$

Using Eq. (2.8) and following the sum rules for the $3j$ and $6j$ symbols one finds the decay rate of the initial state

$$\frac{1}{\tau_j} = \sum_{M_f \mu F_f} \mathcal{A}_{if} = C\nu^3 \frac{\left|\left\langle J_f \left\| \hat{D}_1 \right\| J_i \right\rangle\right|^2}{(2J_i+1)}. \tag{2.13}$$

Substituting Eq. (2.13) into Eq. (2.12) yields a final expression for the spontaneous emission coefficient

$$\mathcal{A}_{if} = \frac{1}{\tau_j}(2J_i+1)(2F_i+1)(2F_f+1) \times \begin{pmatrix} F_f & 1 & F_i \\ -M_f & M_f - M_i & M_i \end{pmatrix}^2 \begin{Bmatrix} J_f & F_f & I \\ F_i & J_i & 1 \end{Bmatrix}^2. \tag{2.14}$$

From the properties of the $3j$ and $6j$ symbols immediately follow the selection rules for electric dipole radiation (E1):

$$\begin{aligned} |J_f - J_i| \leq 1 \leq J_f + J_i \quad &\Rightarrow \quad \Delta J = 0, \pm 1 \quad \wedge \quad J_f + J_i \neq 0 \\ |F_f - F_i| \leq 1 \leq F_f + F_i \quad &\Rightarrow \quad \Delta F = 0, \pm 1 \quad \wedge \quad F_f + F_i \neq 0 \\ &\qquad \Delta M = 0, \pm 1. \end{aligned} \tag{2.15}$$

To calculate the intensities $\mathcal{I}$ of each hyperfine component, Eq. (2.14) has to be summed over the degenerate M_i and M_i states, which results in, see [59]

$$\mathcal{I}(f,i) \propto (2F_i+1)(2F_f+1) \begin{Bmatrix} J_f & F_f & I \\ F_i & J_i & 1 \end{Bmatrix}^2. \tag{2.16}$$

2.2 Optical Isotope Shift

The isotope shift (IS) between isotopes with atomic numbers A, A' is given by [3]

$$\delta\nu^{AA'} = \nu^{A'} - \nu^{A} \tag{2.17}$$

with ν^A and $\nu^{A'}$ representing the transition frequencies with respect to the fine-structure levels. The isotope shift $\delta\nu^{AA'}$ can be separated into a field shift or volume shift (FS) originating from the change in nuclear charge radius and a mass shift (MS) [60]

$$\delta\nu^{AA'} = \delta\nu_{MS}^{AA'} + \delta\nu_{FS}^{AA'} \tag{2.18}$$

The mass shift is usually separated into a normal mass shift (NMS) and a specific mass shift (SMS) caused by a correlation of two electronic momenta due to the motion of the nucleus with its finite mass [35]:

$$\delta\nu_{MS}^{AA'} = \delta\nu_{NMS}^{AA'} + \delta\nu_{SMS}^{AA'} = (K_{NMS} + K_{SMS})\frac{m_{A'} - m_A}{m_A m_{A'}}, \tag{2.19}$$

with K_{NMS} and K_{SMS} the normal and the specific mass shift constant, m_A and $m_{A'}$ the nuclear masses (the nuclear masses are obtained by subtracting the electron masses from the atomic mass taken e.g. from [61]). The normal mass shift constant can be calculated using $K_{NMS} = \nu^A m_e$. The specific mass shift constant K_{SMS} is the expectation value of $\sum_{i>j} \boldsymbol{p}_i \cdot \boldsymbol{p}_j$ for the lower state minus that for the upper state of the transition, with $\boldsymbol{p}_i$ and $\boldsymbol{p}_j$ the momentum of the i^{th} and j^{th} electron in the center of mass frame of the atom, for details see [35].

The field shift can be expressed as

$$\delta\nu_{FS}^{AA'} = F\delta\left\langle r^2\right\rangle^{AA'}, \tag{2.20}$$

with F being the electronic factor and $\delta\left\langle r^2\right\rangle^{AA'} = \left\langle r^2\right\rangle^{A'} - \left\langle r^2\right\rangle^{A}$ the change in nuclear mean square charge radius. The electronic factor F describes the change in the electron density at the nucleus $\Delta\left|\Phi(0)\right|^2$ between the initial state and the final state of an atomic transition. For the medium mass nuclei discussed in this work a non-relativistic approach is sufficient and F can be calculated from [3]

$$F = -\frac{2\pi}{3} Ze^2 \Delta\left|\Phi(0)\right|^2. \tag{2.21}$$

Purely theoretical calculations for the specific mass shift and field shift constants have to be taken with care. In most cases one has to rely on a combination of theoretical calculations in combination with experimental results, see for example Refs. [29, 35] for more details.

If the specific mass shift and field shift constants are known, $\delta\left\langle r^2\right\rangle^{AA'}$ can be calculated using

$$\delta\left\langle r^2\right\rangle^{AA'} = \frac{\delta\nu^{AA'} - (K_{NMS} + K_{SMS})\frac{m_{A'}-m_A}{m_A m_{A'}}}{F}. \tag{2.22}$$

To extract the absolute nuclear rms charge radius R, the nuclear charge radius of at least one isotope has to be determined by a different method, e.g. elastic electron scattering. If such a reference radius exists R can be calculated from the relation

$$R(A') = \sqrt{R^2(A) + \delta\left\langle r^2\right\rangle^{AA'}}. \tag{2.23}$$

2.3 Nuclear Properties from Optical Spectra

The nuclear properties that can be extracted from optical hyperfine spectra are $\delta\left\langle r^2\right\rangle^{AA'}$ from Eq. (2.22), the ground-state spins, magnetic dipole and electric quadrupole moments (chapter 2.1). The frequency ν_{HFS} of a hyperfine transition depends on the hyperfine constants A_u, B_u (A_l, B_l) of the upper (lower) hyperfine level [9]

$$\nu_{HFS} = \nu_{cg} + \alpha_u A_u + \beta_u B_u - \alpha_l A_l - \beta_l B_l, \tag{2.24}$$

where $\alpha = C/2$, $\beta = \frac{3C(C+1)-4I(I+1)J(J+1)}{8I(2I-1J(J-1)}$ and ν_{cg} the center of gravity of the HFS. Before one can use a χ^2-minimization fitting procedure to determine ν_{cg}, $A_{l,u}$ and $B_{l,u}$

one has to define the line profile of the optical transitions, e.g. Gaussian, Lorentzian or a Voigt profile (see chapter 2.5). The IS is then calculated using the resulting ν_{cg}

$$\delta\nu^{AA'} = \nu_{cg}^{A'} - \nu_{cg}^{A}. \tag{2.25}$$

2.4 Collinear Laser Spectroscopy

Collinear laser spectroscopy (CLS) is based on the geometrical superposition of a fast ion beam or atomic beam and a laser beam. The collinear configuration offers two main advantages. The most important one is the intrinsically small line width measured in optical transitions. This effect is caused by the longitudinal compression of the velocity distribution of ions accelerated in an electrostatic field. It is described in the papers of Kaufman [62] and Wing *et al.* [63] and will be summarized in section 2.4.1. The second advantage is the possibility to post-accelerate the ions in the CLS setup (see figure 3.5). This change in velocity causes a Doppler shift of the laser frequency in the rest frame of the ions or neutralized atoms. In this way the laser frequency in this moving frame can be tuned with a variable voltage while keeping the laser at a fixed frequency. This gives the advantage to use a frequency-stabilized laser system (see chapter 3.2.2) and to avoid the relatively complicated calibration of the laser wavelength when the laser frequency is scanned.

2.4.1 Doppler Compression in CLS

The use of accelerated ions enables one to overcome the resolution limits set by the Doppler broadening of the spectral lines. Regardless of the technique used, a spectral line always has a intrinsic non-zero width, related to the finite lifetime (τ) of the states under consideration. Besides this natural line width

$$\delta\nu_n = 1/(2\pi\tau), \tag{2.26}$$

the thermal motions of the atoms cause an additional broadening. At a temperature T, the thermal velocities v are distributed according to the Maxwell-Boltzmann distribution and the Doppler width $\delta\nu_D$ for an atom of mass M and optical transition frequency ν_0 is given by (see for example [8]):

$$\begin{aligned} \delta\nu_D &= \nu_0 \frac{\delta v}{c} \\ &= \frac{\nu_0}{c}\sqrt{\frac{8k_B T ln2}{M}}. \end{aligned} \tag{2.27}$$

With a typical value of several GHz, this width is in many cases bigger than the HFS and IS effects discussed in sections 2.1 and 2.2. The CLS overcomes this limitation by compressing the line width due to the use of accelerated beams. When the ions leave the ion source, they have a certain spread in the kinetic energy δE. Upon acceleration,

all ions are given the same increase in kinetic energy eU but their initial energy spread remains constant. The velocity spread along the beam direction can be calculated using

$$\delta E = \delta\left(\frac{1}{2}Mv^2\right) = Mv\delta v. \tag{2.28}$$

As δE is constant this means that the velocity spread decreases while the velocity increases. Using the Doppler shift for collinear beams $\Delta\nu_D = \nu_0(v/c)$ and Eq. (2.27) in (2.28) gives

$$\delta E = \frac{Mc^2}{\nu_0^2}\Delta\nu_D\delta\nu_D, \tag{2.29}$$

i.e. the product of the Doppler shift and the Doppler width is a constant of motion. Using the relation $v = \sqrt{2eU/M}$, the velocity v as a function of acceleration voltage U, the Doppler width can be written as

$$\delta\nu_D = \nu_0\frac{\delta E}{\sqrt{2eUMc^2}}. \tag{2.30}$$

Given an original energy spread of about 1.5 eV and an acceleration voltage of 40 kV, the Doppler width can be reduced to ≈ 10 MHz, comparable to the natural line width.

2.4.2 Doppler Shift in CLS

The Doppler-shifted frequency ν can be calculated using the relativistic Doppler effect

$$\nu = \nu_0\frac{(1-\beta\cos\phi)}{\sqrt{1-\beta^2}}, \tag{2.31}$$

where ϕ is the angle between the propagation direction of the radiation and the velocity $\boldsymbol{v}$ of the observer (here the atom or ion) and $\beta = |\boldsymbol{v}/c|$ the relativistic Lorentz factor. The frequency ν is that seen by the ion, ν_0 is the frequency of the laser in the rest frame. For collinear or anti-collinear beam-laser alignment it reduces to

$$\nu = \nu_0\frac{(1\pm\beta)}{\sqrt{1-\beta^2}}, \tag{2.32}$$

with $\langle+\rangle$ for the anti-collinear ($\cos(180°) = -1$) and $\langle-\rangle$ for the collinear ($\cos(0°) = +1$) case. In this work, the collinear geometry is employed so the $\langle-\rangle$ must be considered. The resulting Doppler-shifted frequency ν for an ion with charge e and rest mass M_0 accelerated with the total voltage difference U is given by (see Appendix A)

$$\nu = \nu_0\frac{M_0^2c^4}{(Ue+M_0c^2)^2}\left(1-\sqrt{1-\frac{M_0^2c^4}{(Ue+M_0c^2)^2}}\right). \tag{2.33}$$

2.4.3 Bunched Beam Spectroscopy

CLS with laser-induced fluorescence detection is limited in sensitivity by background originating from detector dark counts and scattered laser light from apertures or other components in the beam line. An additional source of background is beam light generated in the charge-exchange process (from the ion of interest and/or from isobaric contamination) if neutralization by charge exchange in a gas is applied. When the production yield is low ($< 10^6$ ions/s) and the ratio of contaminating isobars is high, this is a considerable effect. To reduce the background from detector dark counts and scattered laser light, trapping of the ions (see section 3.1 and Fig. 3.3) and releasing them in bunches with a well-defined time structure can be used. The data-acquisition system (section 3.2.3) can be set in a way that it only accepts counts when the ion bunches are inside the light-collection region. For the remaining time it will not count. With a typical cooling time of 100 ms and a resulting bunch length of 10 μs, a background-suppression factor of 100 ms/10 μs= 10^4 can be achieved [64]. This technique does not reduce the background originating from beam light. This background can be reduced if the wavelength of the fluorescence photons of the ion of interest and the isobars can be separated with an optical filter in front of the detectors (section 4.1.5).

2.5 Line Shapes in CLS

The Doppler compression discussed in section 2.4.1 reduces the Doppler width to a level comparable to the natural line width see Eq. (2.26). The line profile describing the Doppler broadening is the Gauss profile

$$G(x,\sigma) = \frac{1}{\sigma\sqrt{2\pi}}\, e^{-x^2/2\sigma^2}, \tag{2.34}$$

where the full-width-at-half-maximum (FWHM) is given by $\Gamma_G = 2\sigma\sqrt{2\ln 2}$. The natural line width, and other homogenous broadening effects like power broadening, are represented by a Lorentz profile

$$L(x,\Gamma_L) = \frac{1}{\pi}\,\frac{\Gamma_L/2}{x^2 + (\Gamma_L/2)^2}, \tag{2.35}$$

where Γ_L is the FWHM. The resulting line profile is best described by a Voigt profile, which is a convolution of a Gauss and a Lorentz profile

$$V(x,\sigma,\Gamma_L) = \int_{+\infty}^{-\infty} G(t,\sigma)\, L(x-t,\Gamma_L)dt. \tag{2.36}$$

For the analysis of the data, a mathematical representation of the Voigt profile was used (see Ref. [65] for more details). Figure 2.2 gives a comparison of the three line profiles. The Gauss and Lorentz profiles have the same FWHM of 15 MHz. The Voigt profile is build using the shown Gauss and Lorentz profiles resulting in a FWHM of 24.5 MHz.

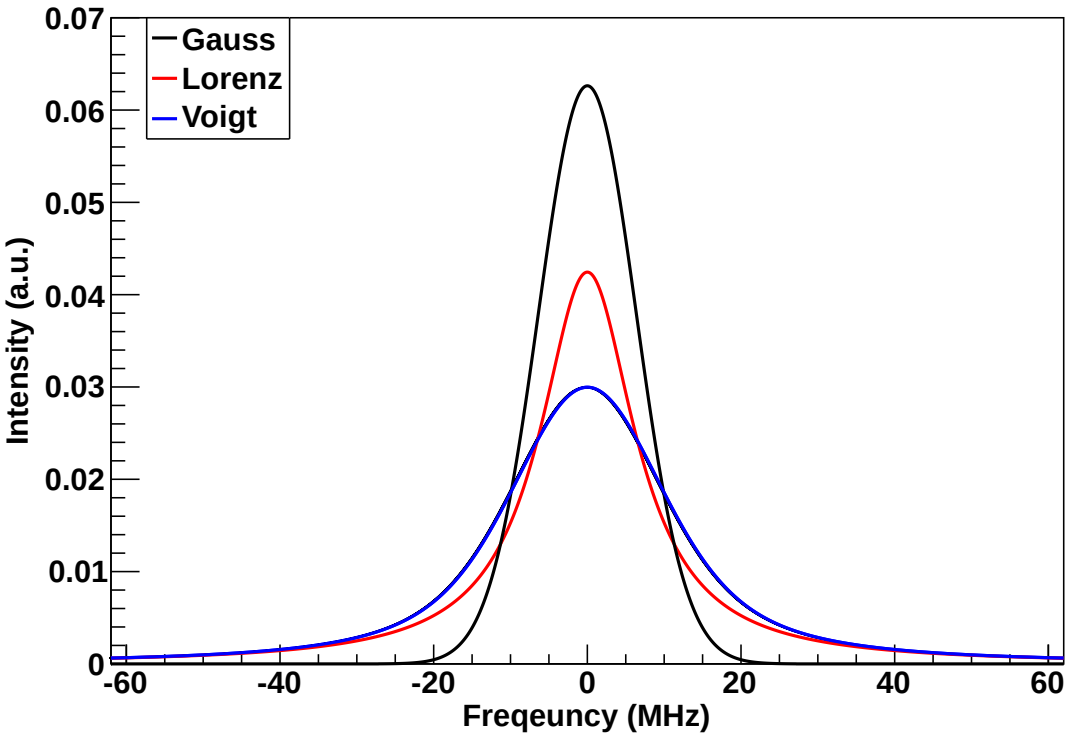

Figure 2.2: Comparison of Lorentz, Gauss and Voigt line Profiles. For details see text.

2.6 Charge Exchange

For spectroscopy on neutral atoms, one has to use a charge-exchange process to neutralize the ion beam. This is typically done in a charge-exchange cell (CEC) filled with a thin vapor of an alkali element. For our K^+ ions we can use a K vapor. Now, two processes can occur in the CEC: a resonant charge-exchange:

$$\boldsymbol{K}^+ + K(4s) \rightarrow \boldsymbol{K(4s)} + K^+ \tag{2.37}$$

with a cross section σ_r; and a non-resonant charge exchange:

$$\boldsymbol{K}^+ + K(4s) \rightarrow \boldsymbol{K(4p)} + K^+ - \Delta E \rightarrow \boldsymbol{K(4s)} + K^+ - \Delta E + h\nu \tag{2.38}$$

with a cross section σ_{nr}. The bold printed letters represent the fast ions. Detailed studies of the processes involved in the charge exchange are given in Bendali *et al.* [66], and Klose *et al.* [67]. Additional to the two mentioned charge-exchange processes, two inelastic collision processes are possible. One in which the collision happens before the charge exchange:

$$\boldsymbol{K}^+ + K(4s) \rightarrow \boldsymbol{K}^+ - \Delta E + K(4p) \rightarrow \boldsymbol{K}^+ - \Delta E + K(4s) + h\nu \tag{2.39}$$

and one in which the collision happens after the charge exchange:

$$\boldsymbol{K(4s)} + \boldsymbol{K(4s)} \rightarrow \boldsymbol{K(4s)} - \Delta E + K(4p) \rightarrow \boldsymbol{K(4s)} - \Delta E + K(4s) + h\nu. \tag{2.40}$$

Due to these inelastic collisions, the line shape of the HFS is broadened [67–69] or multiple peaks occur [66, 70]. Since our energy is higher than the one used in [66], we will not see the multiple peaks but an asymmetric broadening of the lines as shown in [67–69] (see chapter 4). According to Bendali *et al.* [66], the probability of an atom undergoing n collisions is given by Poisson's law

$$P(n) = \frac{x^n}{n!} e^{-x}, \tag{2.41}$$

where x is a parameter depending on the length and the density of the vapor. This distribution represents also the distribution of the relative intensities of the side peaks [66] and can be used to fix the line shape for the analysis of the HFS (see section 4.1.3 and [67]).

3 Experimental Setup

This chapter presents the ISOLDE facility, which provided the K isotopes (section 3.1), as well as the collinear laser spectroscopy setup (section 3.2 and following) at which the measurements presented here have been carried out.

3.1 The ISOLDE Facility

The experiments presented in this thesis have been performed at the on-line isotope separator ISOLDE located at the European Organization for Nuclear Research CERN in Geneva. Detailed information on the ISOLDE facility can be found online [71,72] and

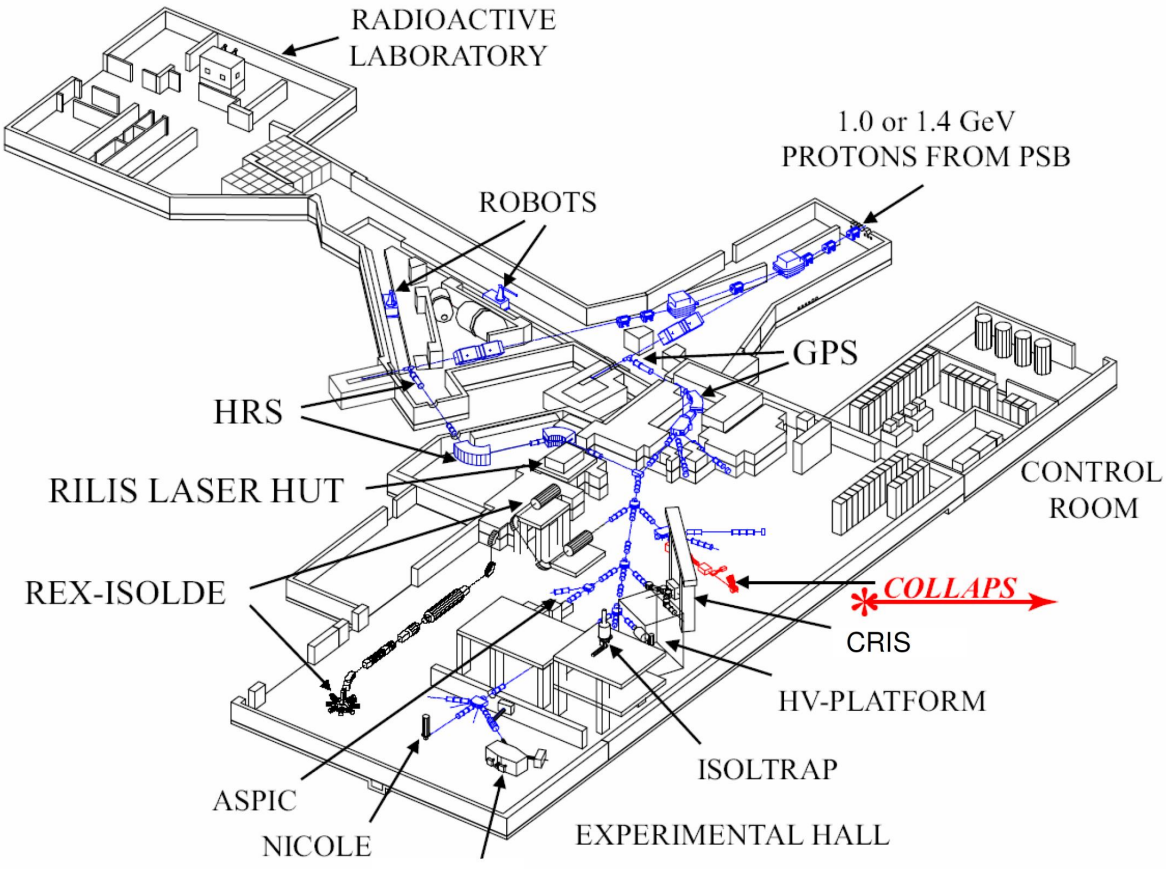

Figure 3.1: Layout of the ISOLDE hall.

in recent publications [73, 74]. ISOLDE is dedicated to the production of a large variety

of radioactive ion beams for different experiments in the field of nuclear and atomic physics, nuclear astrophysics, solid-state physics, life science, and material science.

A general layout of the experimental hall is given in figure 3.1. The radioactive nuclides are produced in one of the two target areas (GPS and HRS in figure 3.1) in thick, high-temperature targets via proton-induced nuclear reactions (spallation, fission or fragmentation). ISOLDE uses the 1.4-GeV proton beam coming from the CERN Proton Synchrotron Booster (PSB) with a maximum intensity of 3.6×10^{13} protons per pulse. The pulses are 2.5 μs long and have a period of 1.2 s or multiples of that. The target material is adapted to the nucleus of interest. For the K isotopes studied, a standard ISOLDE uranium carbide (UC_x) target with a density of 48 g/cm^2 and a surface-ionizer source were used. The produced nuclides diffuse out of the target container into the transfer line (Figure 3.2). To achieve a fast release, the target container and the transfer line are heated to 1500-2000° C. The atoms are then surface ionized in a 3 cm long tungsten cavity which is heated to 1800-2400° C.

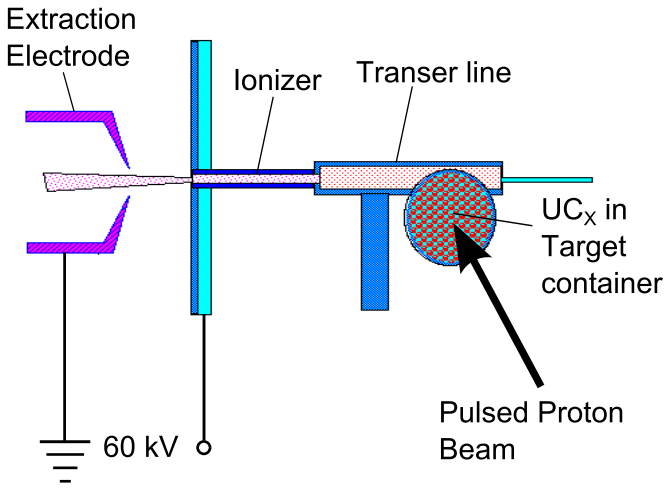

Figure 3.2: A schematic view of the ISOLDE surface-ionizer source with target container, surface-ionizer tube and extraction electrode [72].

After ionization, the ions are accelerated up to 60 keV by an electrostatic potential applied to the ion source (figure 3.2) and sent to the magnetic mass separators. ISOLDE uses two different systems, one the so-called General Purpose Separator (GPS), the other a High-Resolution Separator (HRS). The GPS is a single 60° magnet separator with a maximum mass-resolving power of 2400 [73]. The GPS has a reasonable resolution and allows switching between mass numbers within seconds. In standard operation, a mass-resolving power of about 700 is used. The HRS is a two-stage mass separator with first a 90° and second a 60° magnet. The HRS has a theoretical mass-resolving power of $m/\Delta m$ = 7000-15000 [73] but needs roughly 10 minutes for a mass change since the magnets are cycled in a hysteresis-compensated mode. The standard mass-resolving power used is about 1400-2000. Behind the second magnet, a Radio Frequency Quadrupole (RFQ) cooler and buncher (ISCOOL) is installed [75–78]. The RFQ is

installed on a high-voltage platform to reduce and adjust the energy of the ion beam to a few 10 eV. This energy is adjusted to highest transmission. The RFQ can be used in two operation modes. The most commonly used is the transmission mode. In this mode, the RFQ only operates as an ion-guide cooler and not as a buncher. The second mode is the bunched mode. The RFQ structure is in both modes filled with He as buffer gas at a pressure of about 0.01-0.1 mbar to cool down the transversal and longitudinal energy spread of the incoming ions [75, 78]. Figure 3.3 shows a schematic view of the RFQ and the applied longitudinal potential for trapping (solid line) and ejection (dashed line). In transmission mode the ejection potential (dashed line) is applied. The longitudinal potential together with the buffer gas leads to the trapping of the ions in the potential minimum at the end of the RFQ. The last electrodes are then switched to ejection potential and the bunched ions are extracted.

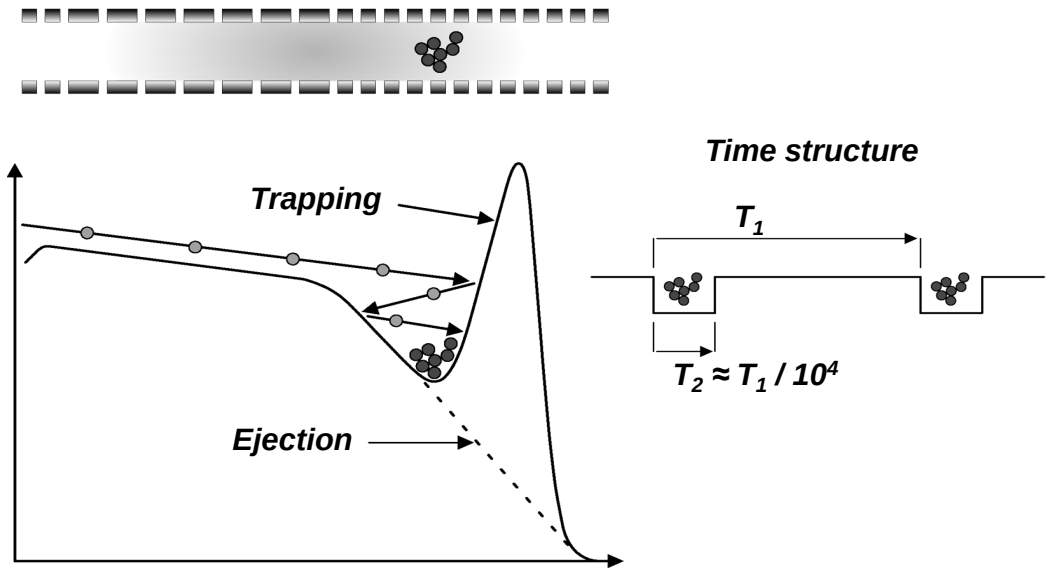

Figure 3.3: Sketch of the RFQ with the applied longitudinal potential for trapping (solid line) and ejection (dashed line). The figure on the right shows the time structure.

The GPS ion beam (after mass separation) and the HRS ion beam (after passing through the RFQ) are directed to a merging switchyard. Here, one of the two ion beams can be directed into the central beam line of ISOLDE. From here the ions are directed to the experiments. The whole beam line, except for mass separation and ISCOOL, uses electrostatic deflectors for bending and quadrupoles for focusing of the ion beam. For the reported experiment on potassium, the HRS and ISCOOL in bunched mode were used. Figure 3.4 shows a technical drawing of the beam line from the HRS target to the COLLAPS setup with all important beam line elements marked. Also shown are the last focusing magnets of the proton beam line from the PSB.

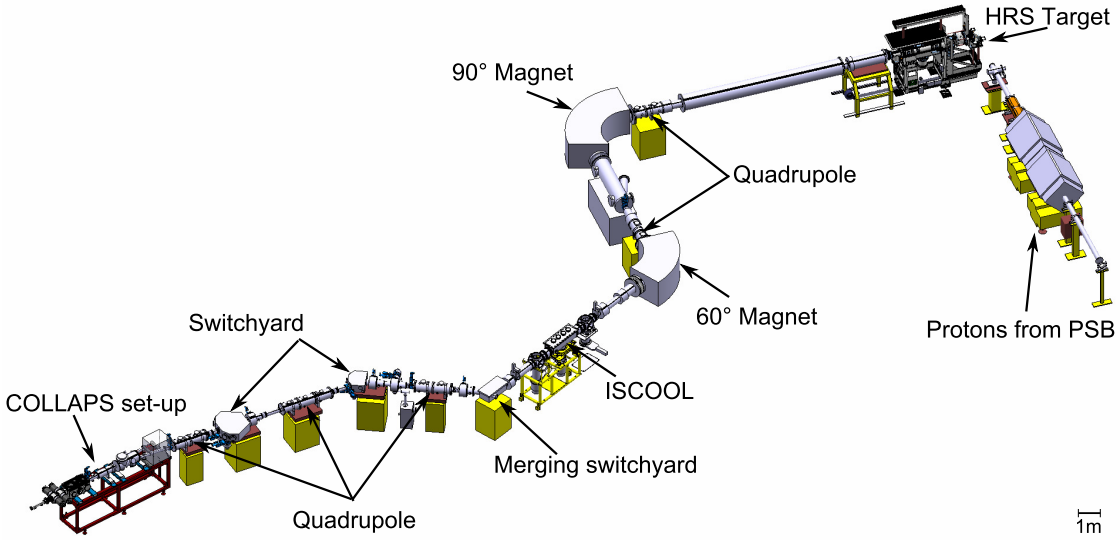

Figure 3.4: Technical drawing of the ISOLDE beam line from the HRS target to the COLLAPS setup.

3.2 The Collinear Laser Spectroscopy Beam Line at ISOLDE

The collinear laser spectroscopy setup at ISOLDE was originally installed in 1980 [1,69]. Since then, the setup has been used in several configurations [5, 11] depending on the experiment performed. The present configuration used in this thesis is shown in figure 3.5.

The setup is kept at high vacuum (10^{-7} mbar) to avoid beam losses and photon background from collisions with residual gases. The ions enter the setup via an electrostatic 10° deflection (label 3 in figure 3.5), which overlaps the ion beam with the linearly polarized laser beam. The ion beam is aligned inside the setup using a set of vertical and horizontal deflector plates and a quadrupole lens system (not shown). A set of variable apertures helps overlapping the laser beam and the ion beam. The ion beam then reaches the post-acceleration region (label 4 in figure 3.5) in which the voltage for the Doppler tuning is applied in 4 steps (1/4, 1/2, 3/4 and full). The charge-exchange cell (CEC) (label 5 in figure 3.5) follows immediately and is kept on the full Doppler voltage. The post-acceleration region and the CEC are mounted electrically insulated inside the vacuum chamber. Inside the CEC, the ions are neutralized using an alkali vapor (see section 2.6). The neutralized atoms enter the light-collection region (LCR) (see section 3.2.1 for details) where their fluorescence light is imaged onto 4 photomultiplier tubes (PMT). To minimize the effect of optical pumping, the distance to the LCR is kept as short as possible (see chapter 4). Behind the LCR, a moveable metal plate and a secondary electron multiplier (SEM) with a moveable first dynode are mounted (not

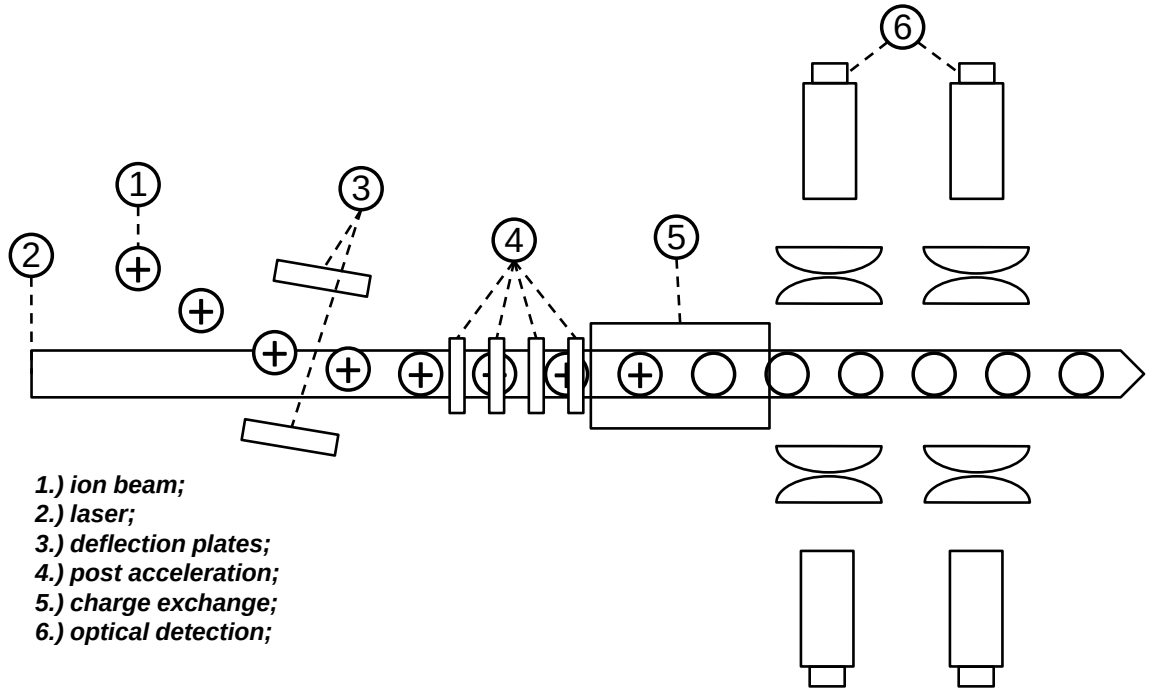

Figure 3.5: Schematic of the COLLAPS setup. For details see text.

shown in the figure). The metal plate is used for ion-current measurements to test beam alignment and to measure the neutralization efficiency. For isotopes with low yield, the SEM is used to determine the amount of ions/atoms of interest (for ion currents below 10^6 ions/s). After passing this section, the atoms hit the exit quartz window for the laser (laser entrance and exit window are oriented under Brewster's angle to minimize reflections).

3.2.1 The New Light-Collection Chamber

Figure 3.6 shows a technical drawing of the new light-collection region (LCR) designed by M.L. Bissell for the measurements of potassium. The objective was to achieve high geometric efficiency for the fluorescence photons and low non-resonant background from scattered laser light and photomultiplier dark counts. A measure for the geometric efficiency is the probability of a photon to reach the photocathode. During the design studies, ray tracing simulations, using a self written MATHEMATICA script, for the existing LCRs and the new design were performed. Figure 3.7 shows the results of these simulations [79]. Shown is the probability of a photon to reach the photocathode along the ion-beam path. For the new LCR the calculations have been performed for light emission with $\delta m_F = 0$ (linear polarization) and $\delta m_F = \pm 1$ (circular polarization) since they have different angular distributions [57, 80]. Using Eq. (2.12) one can calculate the decay rate ($\mathcal{A}_{if}$) for all possible transitions in the used D1 line in K ($4s\ ^2S_{1/2} \rightarrow 4p\ ^2P_{1/2}$) for different ground-state spins I. The calculations show that for all ground-state spins the composition of the emission is $1/3 * (\delta m_F = 0)$ and $2/3 * (\delta m_F =$

± 1), which represents a isotropic angular distribution. The combined results for a isotropic distribution are shown as "Isotropic" and are used for further comparison. The probability for the "Original" and the "Previous" LCR are only shown for isotropic distribution. The "Previous" LCR was designed to aid β-detection measurements [65] and was not designed for high geometric efficiency and low background. The setup uses two PMTs (2-inch diameter) on one side and a cylindrical mirror on the other side. The fluorescence photons are focused into the two PMTs using a single spherical lens for each PMT. The "Original" LCR [2] uses a cylindrical mirror on one and a set of two cylindrical lenses on the other side to focus the fluorescence light onto a light pipe which is connected to one PMT (2-inch diameter).

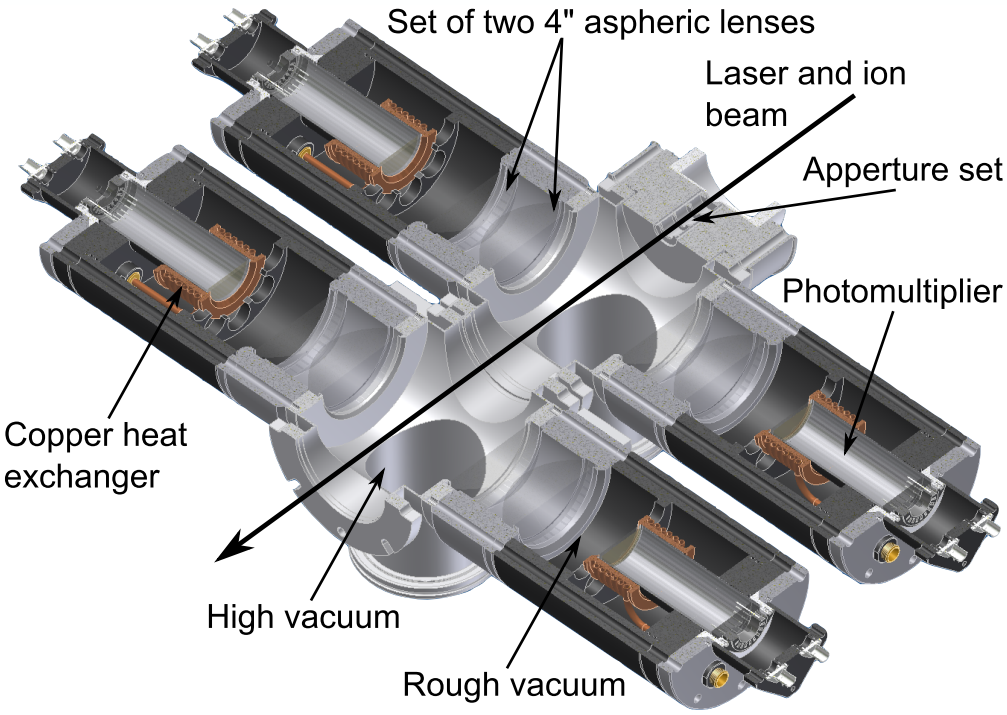

Figure 3.6: Technical drawing of the new Light-Collection Chamber (LCR). Adapted from Ref. [79]

Comparing the results, see figure 3.7 and table 3.1, one can see that the new LCR has a higher geometric efficiency than the two existing ones. Shown in figure 3.7 is the probability of a photon reaching a photocathode as a function of the distance to the charge exchange cell. The geometric efficiency corresponds to the area beneath the curve. Table 3.1 gives the full geometric efficiencies as shown in figure 3.7. In the case of the "Previous" used LCR, it is only possible to cool down one of the two PMTs due to space constraints, therefore only half of the geometric efficiency is available. Taking this into account, the new LCR has a 13 times higher geometric efficiency. Compared

to the "Original" LCR, the gain is only a factor of two, but this one has a too high background from scattered laser light of about 5000 counts/s/mW laser power [69].

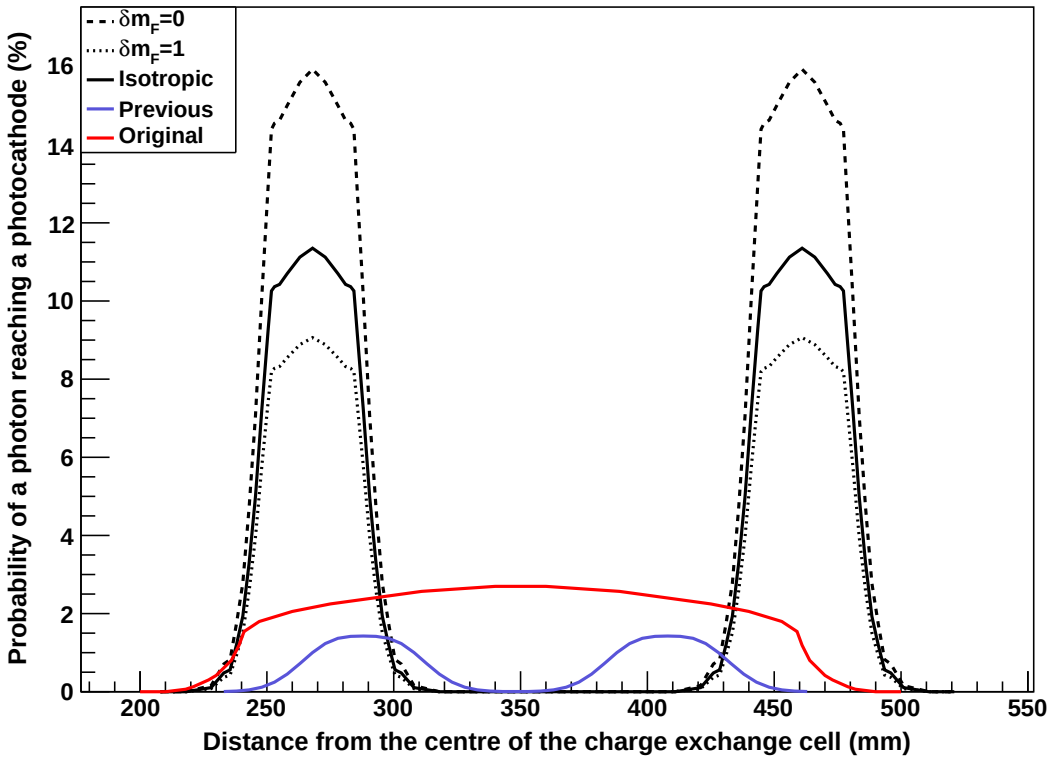

Figure 3.7: Comparison of the geometric efficiency of the new and the two old LCRs. Shown is the probability of a photon reaching a photocathode as a function of the distance to the charge exchange cell. The geometric efficiency corresponds to the area beneath the curve.

The new LCR consists of 4 PMT's (2-inch diameter) arranged in pairs on each side of the beam path (figure 3.6). To achieve a larger geometrical efficiency, the fluorescence photons are imaged onto the PMTs using a telescope consisting of two 4-inch aspheric lenses (Type A100-100LPX-U-S from Asphericon GmbH). This configuration produces an 1:1 image of the overlapped laser and ion beam on the PMTs and a total efficiency of 1 photon in 20000 potassium ions. The ion beam and the image on the PMTs have a diameter of ≈ 6 mm. To suppress the background from scattered laser light the PMTs are masked by an aperture with an opening of 10 mm height and 50 mm length oriented parallel to the ion beam axis. The aperture is slightly larger to account for possible displacements of the ion beam. Compared to the "Previous" setup it was possible to reduce the non-resonant background originating from scattered laser light from typically 1500 counts/s/mW laser power to an average of 1000 counts/s/mW in the new LCR.

Table 3.1 compares the geometric efficiency and background from scattered laser light for the three designs discussed.

Table 3.1: Properties of the light-collection regions used at COLLAPS. For details see text.

LCR	Geometric efficiency	Background from laser light (counts/s/mW)
Original	540	5000
Previous	146	1500
New	1002	1000

With the new design, we achieved two of the initial goals: high geometric efficiency and low background from scattered laser light. To achieve the third goal, low dark-count rates in the PMTs, one has to take a closer look at the used PMTs. For the measurements the photomultiplier type 9658B from Electron Tubes (ET) was used. This type has a typical dark-count rate at room temperature of 15000 counts/s and a typical quantum efficiency of 2.5 % at 770 nm (D1 line in K) with a maximum of 20 % between 350-450 nm. For comparison, the type 9814Q from ET has a dark-count rate of typical 300 counts/s and a quantum efficiency of maximum 30 % between 350-450 nm, but does not work in the infrared. The high dark-count rate of the 9658B originates from thermal radiation of the multialkali IR sensitive photocathode (Typ S20: Na-K-Cs-Sb). This dark-count rate can be reduced by cooling. To achieve this, the new LCR includes housings for the PMTs that are equipped with copper heat exchangers (Figure 3.6) to cool the photocathode of each PMT. The copper heat exchangers are connected to a cryothermostat (LAUDA ECO Silver RE 1045S) that has enough cooling power to cool the PMTs down to -40° C by using a mixture of 90 % pure ethanol and 10 % water. To prevent ice formation on the Glass of the PMTs, the chambers are pumped down to 10^{-2} mbar with an oil free pre-pump (Scrollvac SC15D from Leybold). By cooling the PMTs down to -40° C, the dark-count rate could be reduced to 300 counts/s. This results in a non-resonant background from laser scatter and dark counts of typical 2000 counts/s/mW. Applying the bunched-beam technique described in section 2.4.3 this can be reduced to 0.2 counts/bunch/mW.

3.2.2 The Laser Setup

The Doppler compression used in CLS (see section 2.4) reduces the experimental line width down to about 10 MHz. To resolve the HFS spectra, narrow-band continuous-wave (CW) laser systems are used, which reach laser line widths below 1 MHz. The measurements presented here have been performed with two different laser systems. They will be described in the following.

2010 Measurements

For the first experiment in 2010, we used a titanium:sapphire (Ti:Sa) ring laser (Coherent 899-21) pumped with $\lambda = 532\,\text{nm}$ laser light generated by a diode-pumped solid-state laser (Coherent Verdi V18). With 10 W pump power, 700 mW of infrared laser light at 770 nm was generated. Figure 3.8 shows the setup of the 899 ring cavity in a side view. All elements are mounted on a 2-inch Invar bar that ensures stability and low thermal drifts. Unidirectional lasing is achieved utilizing optical activity and the Faraday effect in an optical diode. The wave propagates counter-clockwise in the cavity. The three plate birefringent filter allows broadband operation with a bandwidth of 2 GHz. After inserting the intracavity etalon assembly (ICA), the bandwidth can be narrowed to 10 MHz. Applying active frequency control, the line width can be narrowed down to 500 kHz RMS. This is achieved with an electronic servo loop and an external reference cavity. The servo loop applies an error signal derived from the reference cavity to the piezo-driven lower fold mirror for fast cavity-length variations, and to the galvo driven rotating Brewster plate to compensate for slower cavity-length changes.

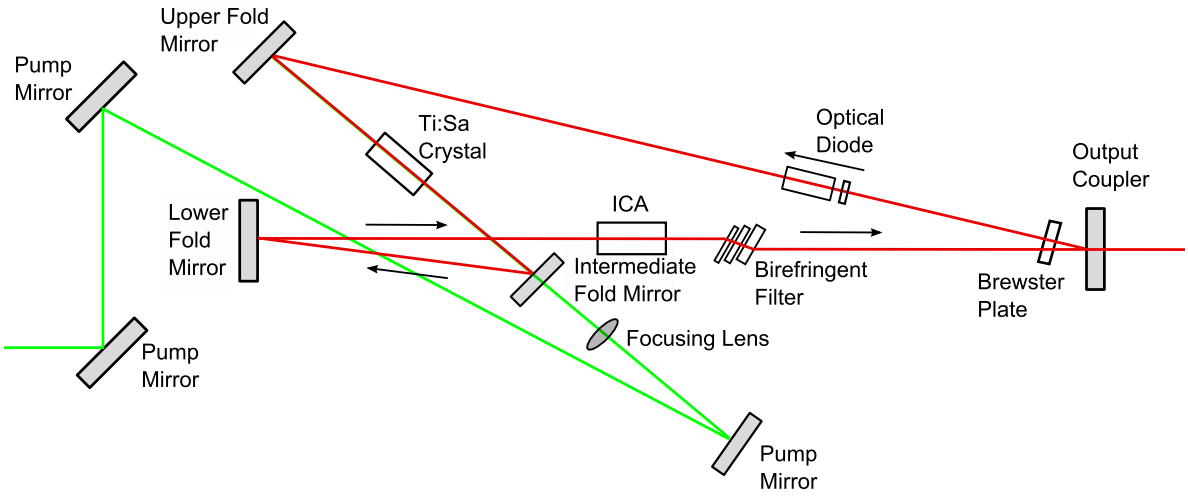

Figure 3.8: Scheme of the 899-21 laser. Four mirrors form a ring cavity. Single-mode operation is achieved with several frequency selective elements: a birefringent filter, an intracavity etalon assembly (ICA) consisting of a thick and a thin etalon, and the ring resonator itself. Unidirectional lasing is ensured by an optical diode (the direction is indicated by arrows). Laser frequency drifts are detected with a reference cell and compensated using the piezo-driven lower fold mirror and the galvo driven rotating Brewster plate. Adapted from ref. [81].

The built-in stabilization of the 899 ring laser is not temperature compensated resulting in slow drifts of the frequency over temperature changes and time. To compensate this the laser is coupled to a long term stabilization system [82] consisting of a frequency

stabilized helium-neon (He-Ne) laser (Melles Griot STP1), a piezo-driven confocal Fabry-Pérot interferometer (FPI) and custom-made locking electronics. The He-Ne laser has an output power of $< 0.9\,\mathrm{mW}$, a wavelength of $632.8\,\mathrm{nm}$, a frequency stability of $\pm 3.0\,\mathrm{MHz}$ over 8 hrs, and a temperature dependence of $0.5\,\mathrm{MHz/°C}$. The FPI is mounted inside a vacuum chamber to decouple it from temperature and air pressure changes.

Figure 3.9 shows the overview of the laser setup. A fraction of the Ti:Sa laser beam is transported to the stabilization system using two beam splitters (first a 50/50 and second a 10/90) and an optical fiber. Behind the fiber coupler (FC), the beam passes trough a half-wave plate ($\lambda/2$), which is used to adjust the polarization for the overlap of the beams in the polarizing beam splitter (BS). The He-Ne laser beam is passing trough

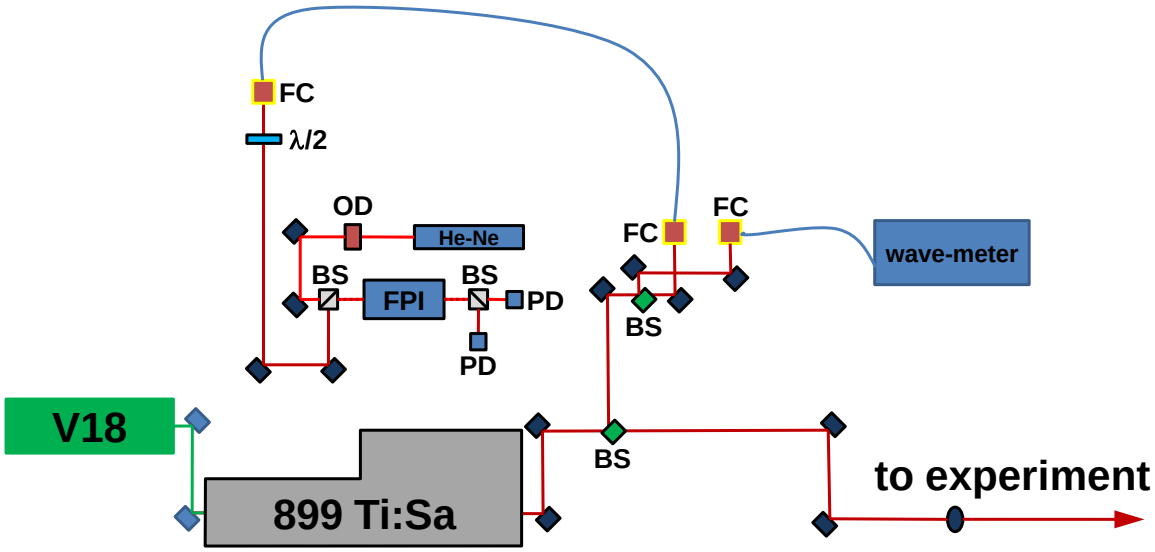

Figure 3.9: Scheme of the laser setup. The Coherent 899 Ti:Sa laser is pumped by a Coherent Verdi V18. The infrared laser light is split into two parts by a beam splitter (BS). The transmitted beam is directed to the experiment, the reflected to a second BS. The reflected beam of the second BS is coupled into a fiber (FC) connected to a wavelength meter. The transmitted beam is coupled into a fiber transferring the laser beam to the long-term stabilization setup. Here, the laser beam of the Ti:Sa is overlapped in a polarizing BS with the beam of the He-Ne laser and coupled into the FPI. Behind the FPI, the laser beams are split in a second polarizing BS and directed into two photo diodes (PD) which are connected to the locking electronic.

an optical diode and is coupled into the FPI through the polarizing BS. To maximize transmission, the polarization axis can be adjusted on the laser. The polarizing BS is used to overlap the laser beam of the He-Ne and the Ti:Sa in the FPI. After passing through the FPI, a second polarizing BS splits the two laser beams and directs them into two photo diodes (PD). The signal of the He-Ne laser PD is used to lock the FPI to the He-Ne laser. This is achieved by locking the FPI to one of the etalon modes of the

He-Ne frequency using a custom-made servo loop controlling the piezo-driven mirror of the FPI. The signal of the Ti:Sa laser PD is connected to a custom-made servo control loop, which uses the external control input at the 899 laser control box to feed in the error signal and to lock the Ti:Sa laser frequency to the stabilized FPI. The Ti:Sa laser is then locked to the low-temperature drift of the He-Ne laser. This allows longer scan times of hyperfine structures without reference scans. With a non-stabilized laser one has to measure the reference isotope every 5-10 minutes to calibrate the wavelength, which is not possible with the HRS magnets (see section 3.1).

To adjust the wavelength, the Ti:Sa laser beam is coupled into a wavelength meter (Bristol 621A). The wavelength meter has a built-in reference He-Ne laser for continuous calibration. The absolute accuracy of the wavelength meter is ±60 MHz @ 300 THz, which is precise enough to adjust the wavelength to the acceleration voltage used.

The main laser beam is directed over several mirrors to the COLLAPS setup. Before entering the vacuum chamber, the laser beam passes trough a telescope which is used to adjust beam focus and size to maximize the overlap of laser and ion (atom) beam. A half-wave plate is used to maximize the transmission trough the Brewster window. The power is adjusted using neutral density filters. The power used during the experiment on potassium isotopes was in the range of P_{laser} = 0.2-1.2 mW at λ = 770 nm with a beam diameter of d_{laser} = 4 mm at the LCR (compare figure 3.5).

2012 Measurements

For the 2012 experiment, a new Ti:Sa laser (Sirah Matisse TS) was used. Figure 3.10 shows the setup of the Matisse TS laser in top view. The main difference to the Coherent 899 laser is the orientation of the cavity. The 899 laser is mounted on a 2-inch Invar bar, with the cavity oriented vertical. The Matisse TS laser is mounted on a Invar base plate, with horizontally oriented cavity. The second difference concerns the way of achieving unidirectional lasing in the ring cavity. The 899 laser uses an optical diode to suppress the clockwise-propagating wave. In the Matisse TS laser, a combination of Faraday isolator and the out-of-plane (OP) mirror suppresses the clockwise-propagating wave. The Faraday isolator rotates the polarization independent of the propagation direction by +2°. The OP mirror rotates the polarization of the counter-clockwise-propagating wave by −2° and the clockwise-propagating wave by +2°. As a result, the polarization rotations for the counter-clockwise-propagating wave cancel out thus suppressing the clockwise-propagating wave due to losses on the Brewster-cut surfaces in the resonator. Single-mode operation is achieved in the same way as it is done in the 899 laser: with a birefringent filter, a separate thin and thick etalon, and active stabilization through a temperature-stabilized external reference cavity. The locking system controls the tuning mirror for correction of slow drifts and the fast piezo mirror for fast corrections of the cavity length. The Matisse TS laser achieves line widths below 500 kHz. The laser was pumped with 10 W from the Verdi V18 and generated an output power of 1.2 W at 770 nm.

The Matisse laser offers the possibility to couple light into the fiber for the wavelength meter directly in the housing avoiding an extra beam splitter in the main path. Only

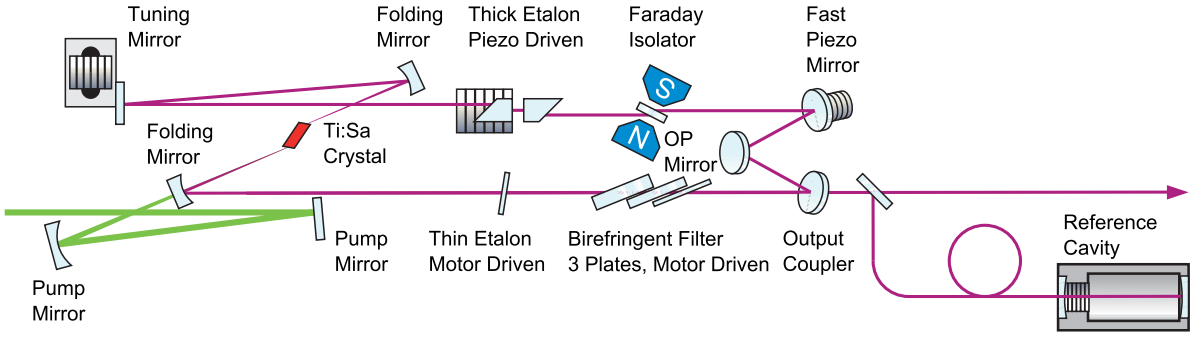

Figure 3.10: Scheme of the Matisse TS laser. Six mirrors form a ring cavity. Single-mode operation is achieved with several frequency selective elements: a birefringent filter, a thick and a thin etalon, and the ring resonator itself. Unidirectional lasing is ensured by the combination of an out-of-plane (OP) mirror and a Faraday Isolator (FR). Laser frequency drifts are detected with a temperature-stabilized reference cell and compensated using the piezo-driven mirrors. Adapted from ref. [83].

one BS is used to direct the laser beam to the long-term stabilization. The laser setup is the same as in the 2010 experiment from figure 3.9 except for the Matisse TS laser. The Matisse TS laser is computer controlled and has no direct input for the error signal. An analog-to-digital converter (ADC) (National Instruments USB-6009) was used to feed the analog error signal into the computer and the control program. The control program has the built-in function to use this signal for long-term stabilization by applying the signal to the reference cavity on which the laser is locked. The transport of the laser beam to the experiment was done in the same way as in the 2010 experiment. For this experiment, the power used was $P_{laser} = 1.2\,\mathrm{mW}$ at $\lambda = 770\,\mathrm{nm}$ with a beam diameter of $d_{laser} = 4\,\mathrm{mm}$. A comparison of the wavelength stability over time for the two laser systems is given in chapter 4.

3.2.3 The Data Aquisition System

The experiment is controlled by a computer program (Measurement and Control Program MPC). The MCP allows the user to define different types of scans. The most common is a scan which records counts as a function of a computer-controlled voltage. The program allows this voltage to be set in a range from $U_{DAC} = -10\,\mathrm{V}$ to $U_{DAC} = +10\,\mathrm{V}$ (range of the 18 Bit DAC), and the number of channels used. The range is set to the minimum needed to cover the HFS and the number of channels to the best value to resolve the spectrum and to measure in a reasonable amount of time. Typical values used for K are 101 channels with a step size of 0.02 V. One may split the scan into several tracks allowing regions between the hyperfine structure peaks to be skipped if required (example are given in chapter 4). Figure 3.11 shows a schematic view of the setup with power supplies for the Doppler tuning, charge-exchange cell (CEC) heating and read-out

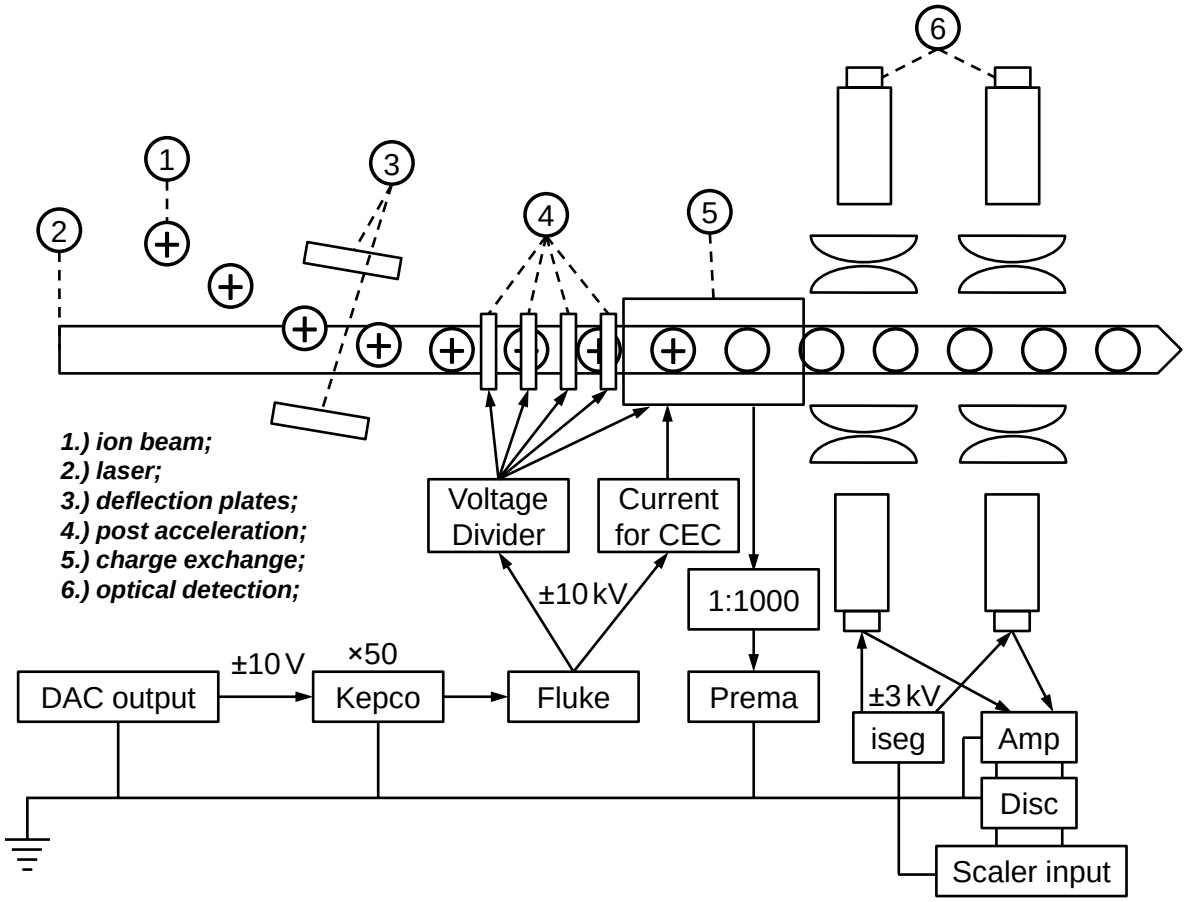

Figure 3.11: Scheme of the COLLAPS setup with power supplies and read-out electronics. For details see text.

electronics. The signal from the computer DAC (Hytec 670 18Bit DAC) is amplified by a fast linear-voltage amplifier (Kepco BOP 500M), which has an amplification factor of about $a_{Kepco} \approx 50$ (the exact value determined in the experiments is given in chapter 4). The scan voltage available for post-acceleration is $U_{scan} = U_{DAC} * a_{Kepco} = \pm 500\,\mathrm{V}$. Since the laser frequency is locked and kept fixed to the same value by the long-term stabilization, an additional offset voltage (U_{off}) is applied to the post-acceleration region to allow for the measurement of isotopic chains. This is done with a high-voltage power supply (Fluke 410B) that is floated on the scan voltage. The Fluke offers an offset voltage from $U_{off} = -10\,\mathrm{kV}$ to $U_{off} = +10\,\mathrm{kV}$. For the measurements presented here, the laser frequency was set to give access to potassium isotopes with mass numbers $A = 38$ to $A = 51$ with the available $U_{off} = \pm 10\,\mathrm{kV}$ from the Fluke power supply. The total voltage applied to the post-acceleration region is $U_{tot} = U_{DAC} * a_{Kepco} + U_{off}$. The applied voltage is directly measured by a high-voltage divider (Julie Research 1 : 1000) connected to a digital voltmeter (Prema 6040). After each scan, the MCP records the voltage of the Fluke by applying 0 V to the DAC. Three Fluke power supplies are avail-

able and can be selected in the MCP with an additional computer-controlled switch box (not shown in figure 3.11) that connects one of the Fluke power supplies to the post-acceleration region and CEC heating. This configuration provides a relative accuracy of the voltage of 10^{-4}. If no scan is running, no voltage is applied to the setup. A custom-made floating power supply is used to heat the charge-exchange cell (compare cipher 5 in figure 3.11). It provides a maximum current of $I_{CEC} = 5\,\mathrm{A}$ and maximum voltage of $U_{CEC} = 60\,\mathrm{V}$, and is operated in voltage control mode. The heating wire used had a resistance of $R_{CEC} = 35\,\Omega$.

The photomultiplier tubes (compare cipher 6 in figure 3.11) are powered by two power supplies (iseg NHQ 203M two Ch.), which can deliver voltages up to $\pm 3\,\mathrm{kV}$ with a maximum current of 4 mA. The voltage for each PMT is adjusted individually. The signal of each PMT is first amplified in a variable gain amplifier (Phillips Research Mod. 777 8 Ch.) and then discriminated (CAEN Mod. N413A 8 Ch.) before it is sent to the scaler input (CAEN C257 16 Ch. NIM scaler, compare figure 3.11).

In the case of bunched-beam spectroscopy, the signals are sent in parallel to a coincidence setup counting only signals when the ion beam is in front of the PMTs and are then sent to the scaler input. This gives the advantage of having raw and gated signal recorded. The setup uses two three fold logic units (CAEN three Fold Logic Unit Mod. 405) combining the signal with the gates (logic AND). Each PMT has its own unit. The generation of the gates is described below.

To control accumulation and release of ions in ISCOOL, a setup with one coincidence unit (LeCroy Quad Coincidence Unit Mod. 622) and two dual timers (CAEN Dual Timer Mod. 2255B) was set up to generate an adjustable number of TTL pulses to close ($U_{ISCOOL} = 0\,\mathrm{V}$) and open ($U_{ISCOOL} = 5\,\mathrm{V}$) ISCOOL (compare figure 3.12) upon triggering. The number of ion bunches and the accumulation time can be adjusted. The release time was constant and set to $t_{open} = 100\,\mu\mathrm{s}$. The ISOLDE proton trigger was used as trigger signal, a TTL pulse synchronized to the arrival of the proton pulse at the target. The ISCOOL control signal is also used to generate the gates used in the coincidence setup for the PMT signals. Here, the signal that controls ISCOOL is converted into a delayed gate using two dual timers (CEAN Dual Timer Mod. 93B). Two signals are generated to have the possibility to use different delays and gates for the two rows of PMTs. The delay and width was defined using a time-of-flight spectrum of one PMT recorded in a multi-channel scaler (Stanford Research SR430). The spectrum is recorded using the control signal of ISCOOL as start and the ungated signal of one PMT as signal input. Typical values used for ^{47}K at an acceleration voltage of $U_{acc} = 40\,\mathrm{kV}$ are a delay of $t_d = 45\,\mu\mathrm{s}$ with a width of $t_w = 7\,\mu\mathrm{s}$. The former corresponds to the time of flight from the cooler to the light-detection region, the latter to the bunch length. An example time-of-flight spectrum is shown in figure 4.5 of the next chapter.

Figure 3.12 shows an oscilloscope screen shot with the signals used to control the ISCOOL buncher and one of the coincidence gates for the PMT signals. In yellow, the proton trigger from ISOLDE is shown, also used as trigger for the oscilloscope. The yellow arrow on top of the screen shot shows the position of the proton trigger pulse, which is not visible on the time scale used. The pink line denotes the gates for the coincidence with the PMT signals. The control signal, which opens and closes ISCOOL,

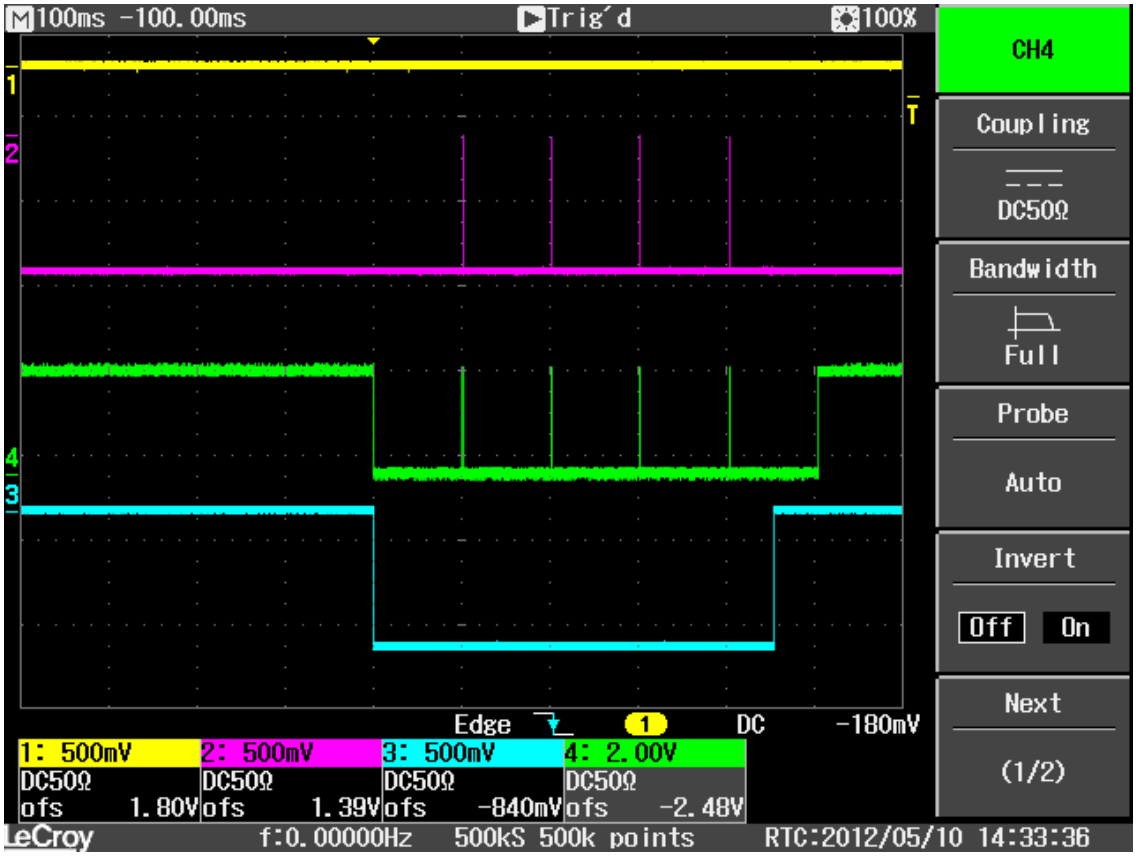

Figure 3.12: Oscilloscope screen shot showing the signals used to control the ISCOOL buncher and for the coincidence with the PMT signals. Yellow: proton trigger from ISOLDE, also used as trigger for the oscilloscope. Pink: gates for the coincidence with the PMT signals. Green: control signal that opens and closes ISCOOL. Blue: gate that defines the number of ion bunches. For details see text.

is shown in green. Finally, the gate defining the number of used ion bunches is depicted by the blue line. To avoid filling ISCOOL beyond its storage capacity, it is kept open when no signal is applied and actively closed only when a proton trigger arrives.

To synchronize the data acquisition with the bunched signals, the MCP offers the possibility to trigger the scans with an external signal. The scan waits for an external trigger to start collecting counts and changes the voltage every time an external trigger is applied. For this purpose the proton trigger from ISOLDE was used. For each trigger, the MPC was set to count the PMT signals for a time of $t_{count} = 1\,\mathrm{s}$ since the proton pulses have a period of $t_{pp} = 1.2\,\mathrm{s}$. The proton-triggered data acquisition had to be used since the release time of the radioactive K isotopes is only about $t_{release} = 300\,\mathrm{ms}$, which is for most of the measured K isotopes shorter than their half-life.

4 Spectroscopic Measurements on Potassium

In what follows, the experimental results are presented and discussed. This chapter presents the data obtained in the two measurement campaigns of COLLAPS at ISOLDE in 2010 and 2012. It focuses on the collection of hyperfine spectra, conversion of raw data and other technical details concerning the treatment of the data. Some preliminary conclusions are drawn. The next chapter presents the results of the data analysis of the measured hyperfine spectra of $^{38g,38m,39,42,44,46-51}$K. The spins of $^{48-51}$K could be measured for the first time. Isotope shifts of all measured isotopes referenced to ^{47}K are compared to literature. Moreover, the changes in mean square as well as the rms charge radii are presented.

Table 4.1: Basic properties of the presented potassium isotopes. Spins and half-lives are taken from Ref. [84]; Masses are taken from Ref. [61]; Yield information is taken from the ISOLDE yield database if available for the used UC_x target [72].

A	I^π	Mass (μamu)	Half-life	Yield (ions/μC)
37	$3/2^+$	36973375.889(100)	1.226(7) s	NA
38m	0^+	37969220.678(209)	924.3(3) ms	NA
38g	3^+	37969081.117(209)	7.636(18) m	NA
39	$3/2^+$	38963706.486(005)	stable	NA
40	4^-	39963998.166(060)	stable	NA
41	$3/2^+$	40961825.258(004)	stable	NA
42	2^-	41962402.306(113)	12.321(25) h	NA
43	$3/2^+$	42960734.702(440)	22.3(19 h	NA
44	2^-	43961586.985(450)	22.13(19) m	NA
45	$3/2^+$	44960691.493(560)	17.81(61) m	NA
46	2^-	45961981.586(780)	105(10) s	NA
47	$1/2^+$	46961661.614(1.5)	17.50(24) s	NA
48	(2^-)	47965341.186(830)	6.8(2) s	$1.3 * 10^6$
49	$(1/2^+, 3/2^+)$	48968210.755(860)	1.26(5) s	$2.7 * 10^5$
50	$(0^-, 1^-, 2^-)$	49972380.017(8.3)	472(4) ms	$3.7 * 10^4$
51	$(1/2^+, 3/2^+)$	50975828.036(14.0)	365(5) ms	$4.5 * 10^3$

Finally, chapter 6 discusses the physics impact of the new data. Spins and charge radii provide information of the structural evolution along an isotopic chain. The evolution

of the $\pi d_{3/2}$ orbital in the potassium isotopes as well as the behavior of charge radii in the region of potassium and the magic-shell isotopes of calcium will be discussed.

Table 4.1 lists basic properties of the potassium isotopes studied within the scope of this work. The properties of $^{37-51}$K important in the context of collinear laser spectroscopy are given, such as spin, half-life, mass and production rate (yield). Spins and half-lives are taken from the database of the National Nuclear Data Center [84], the masses from the newest atomic-mass evaluation AME2012 [61], and the yield information from the website of ISOLDE (Experiments/Yield Database) [72] if available for the UC_x target employed. Section 4.1 covers the data measured in 2010, section 4.2 those of 2012.

4.1 The 2010 Experiment

This experiment was carried out using the new LCR, compare figure 3.2.1. Besides its characterization, the other parameters necessary for the collection of data had to be adjusted. Among these are the settings of the CEC, which were determined with stable potassium, and the laser wavelength and power (compare cipher 2 in figure 3.11). Subsequently, the release of potassium from the ISOLDE target was measured to determine appropriate timing.

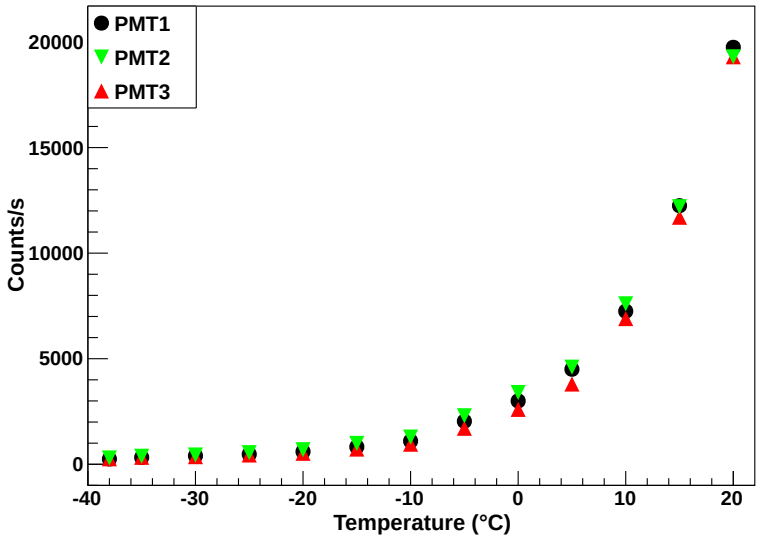

Figure 4.1: Dark-count rate as a function of temperature for three PMTs. The dark-count rate could be reduced from 20,000 counts/s to below 300 counts/s by cooling the PMTs from room temperature down to −38° C.

First, offline tests were performed to confirm the specifications of the new LCR. The reduction of the dark-count rate was tested upon cooling down of the PMTs. Figure 4.1

shows the count rate of the individual PMTs for different temperatures while cooling down to −38° C. The dark-count rate could be reduced from about 20,000 counts/s at room temperature (20° C) to below 300 counts/s at −38° C. The curve of PMT4 (compare figure 4.1) is missing because the PMT broke and could not be tested after re-installation.

The dark-count rate at low temperature reaches the value of a standard PMT for visible light (for example ET-9814Q), which was the aim in the design of the new LCR (see section 3.2.1). Following this test, the dark-count rate could be reduced even further by improving shielding as well as grounding of the signal cables. Finally, a total combined dark-count rate of about 850 counts/s summed over all four PMTs was reached. The background from scattered laser light was measured to about 1,000 counts/s/mW for all four PMTs.

In a second step, the first spectra were recorded on stable ^{39}K to adjust the charge-exchange temperature and optimize the laser power (compare cipher 2 and 5 in figure 3.11). The temperature of the CEC is directly related to the density of the potassium vapor inside the CEC and thus to the efficiency of the charge exchange process. The temperature is measured with an uncalibrated thermocouple in mV. The absolute temperature in ° C is not important since it is only used to keep stable conditions.

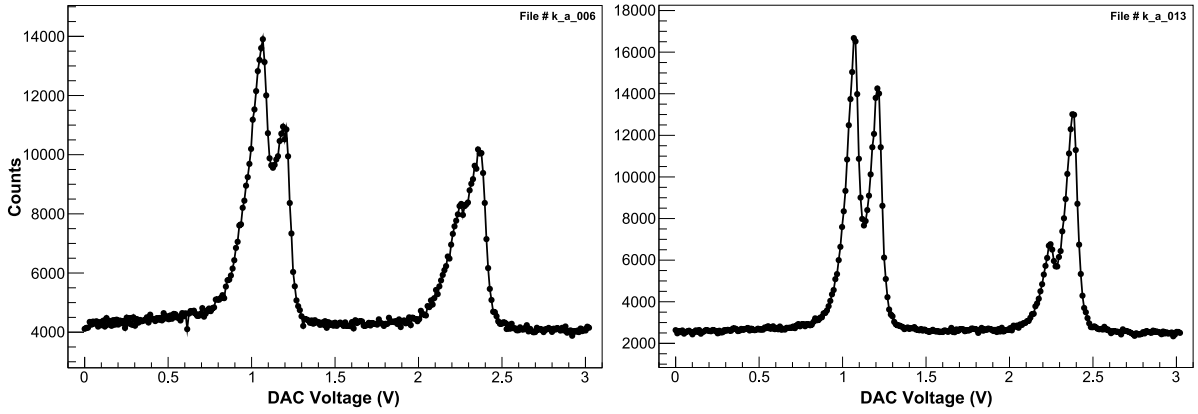

Figure 4.2: Continuous spectra of ^{39}K for high (6.5 mV) and low (5 mV) charge-exchange temperature. Shown is the sum of the counts in all four PMTs as a function of the DAC voltage. The data points are connected to guide the eye.

Figure 4.2 shows two spectra of ^{39}K recorded with different charge-exchange temperatures. Shown is the sum of the counts in all four PMTs as a function of the DAC voltage. The data points are connected to guide the eye. The left (right) spectrum was recorded with a charge-exchange temperature of 6.5 mV (5 mV). In both scans, a potassium ion current of $I_K = 650$ pA and a laser power of $P_{laser} = 0.16$ mW were used. The spectra were recorded with a time window of 0.5 s per channel. Comparing both spectra, the difference in the resolution of the four HFS peaks is clearly visible. The spectrum with reduced charge exchange rate shows a smaller width of the peaks and has a more pronounced separation of the four peaks. In addition a reduced background

from beam light (light emitted from atoms excited in the charge exchange gas) could be achieved. For the online experiment the settings of the right plot in figure 4.2 were used. The charge-exchange heating voltage was set to $U_{CEC} = 30\,\mathrm{V}$ resulting in a current of $I_{CEC} = 0.86\,\mathrm{A}$ and a neutralization efficiency of more than 50 % at a temperature of 5 mV.

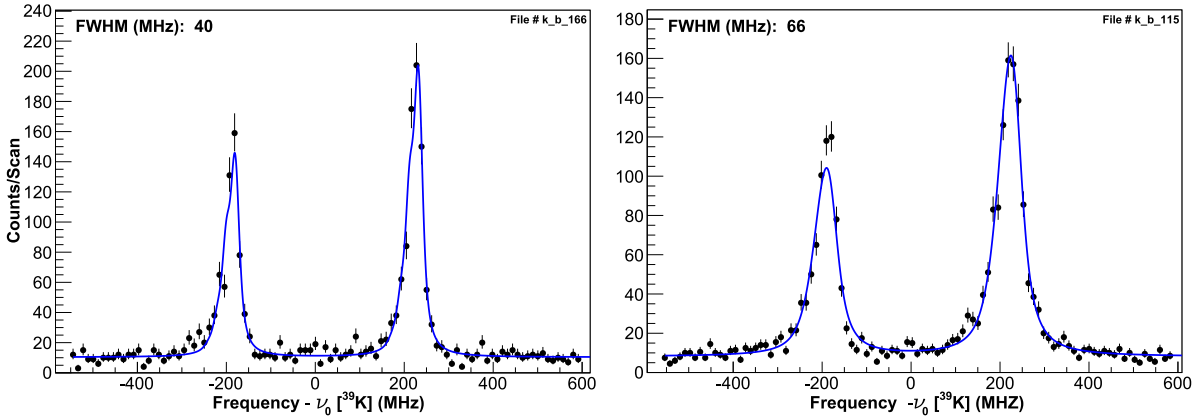

Figure 4.3: Gated spectra of the left multiplet of ^{47}K for low and high laser power. Shown are the counts/scan as a function of shifted frequency (see section 4.1.2). The blue line is a fit with the line shape defined in section 4.1.3. The left (right) spectrum was recorded with a laser power of $P_{laser} = 0.2\,\mathrm{mW}$ ($P_{laser} = 1.2\,\mathrm{mW}$). Shown inside the plots is the FWHM of the fitted profile.

Third, a suitable laser power had to be determined. Higher laser power results in a higher detection efficiency but due to optical pumping effects (saturation broadening) produces broader peaks causing less-resolved hyperfine spectra. For isotope-shift measurements, a good resolution is necessary to get an accurate measurement of the HFS centroids. Low laser power should be chosen to help resolve the hyperfine spectra. Figure 4.3 shows a comparison of the left multiplet of the hyperfine spectrum of ^{47}K for $P_{laser} = 0.2\,\mathrm{mW}$ and $P_{laser} = 1.2\,\mathrm{mW}$ in the left and right spectrum, respectively. It is clearly visible that the higher laser power produces broader lines. The FWHM increases from 40 MHz at 0.2 mW laser power to 66 MHz at 1.2 mW. The effect of higher count rate with higher laser power is not visible since the ion current was reduced in the scan with higher laser power. Initially a laser power of $P_{laser} = 1.2\,\mathrm{mW}$ was chosen in the 2010 online experiment for possible measurements of the most exotic and thus least produced isotope ^{51}K. Unfortunately, low yield from the ISOLDE target as well as high background hindered a measurement of ^{51}K (see section 4.1.5 for details). It was then decided to perform isotope-shift measurements up to ^{50}K with a laser power of $P_{laser} = 0.2\,\mathrm{mW}$.

In a fourth step, the timing for the control of ISCOOL and the coincidence setup was addressed (see section 3.2.3). To determine the number of ion bunches per proton trigger, the release of potassium from the ISOLDE target was probed, which depends on element-specific chemical properties. A so-called release curve was recorded for ^{50}K. To

record the release curve, the continuous ion beam was directed to the secondary electron multiplier (SEM) at the end of the beam line. The isotope ^{50}K was used because the yields of the other isotopes were too high to direct them into the SEM. The release time of an element is identical for all isotopes as long as the half-life is longer than the release time, which is the case for most of the potassium isotopes, except ^{50}K and ^{51}K which have a half-life in the order of the release time (see table 4.1).

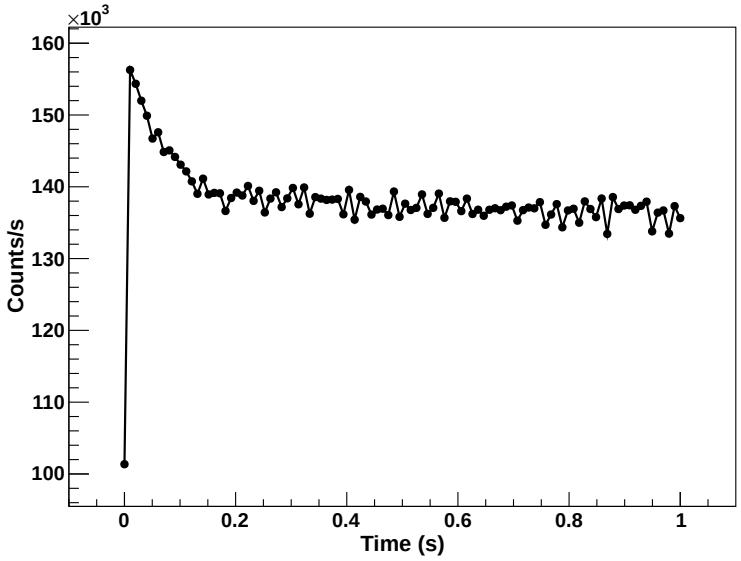

Figure 4.4: Release curve of ^{50}K showing counts as a function of time elapsed after proton impact on target.

Figure 4.4 shows a typical release curve. Shown are the counts/s recorded for 1 s after a proton pulse hit the target. The plot is the sum of 100 proton pulses with time steps of 0.01 s per channel. It is clearly visible that the release curve consist of a fast and a slow component. The fast component originates from the potassium ions the slow component from isobaric contamination. The release time of the potassium isotopes was determined to be about 300 ms. According to this, the electronics for the control of ISCOOL was set to accumulate ions for 45 ms and to release them in 100 μs. The number of bunches was set to 6 after a proton pulse. The optimal number of bunches is determined by comparing the signal-to-background ratio (S/B) in the recorded spectra for different number of bunches. The optimal value has the highest S/B-ratio.

To determine the timing for the gates, a time-of-flight (TOF) spectrum of the ungated bunched potassium ion beam was recorded (see section 3.2.3 for details). Figure 4.5 shows the TOF spectra of ^{39}K, ^{47}K and ^{50}K recorded for an acceleration voltage of $U_{acc} = 40$ kV. In the case of ^{39}K the gate was set to a delay of $t_d = 41\,\mu$s with a width of $t_w = 7\,\mu$s. In the case of ^{47}K the width was kept the same and the delay was set to $t_d = 45\,\mu$s. The TOF spectrum of ^{50}K shows a reduced peak width. The reduction is due to the reduced ion current of potassium at this mass in ISCOOL. For details on

this effect, the reader is referred to Ref. [78]. The delay for ^{50}K was set to $t_d = 47.5\,\mu$s with a width of $t_w = 4\,\mu$s. The reduction of the TOF peak width also occurs in ^{38,49}K. Similar TOF spectra were recorded for the other potassium isotopes and the gates were set accordingly.

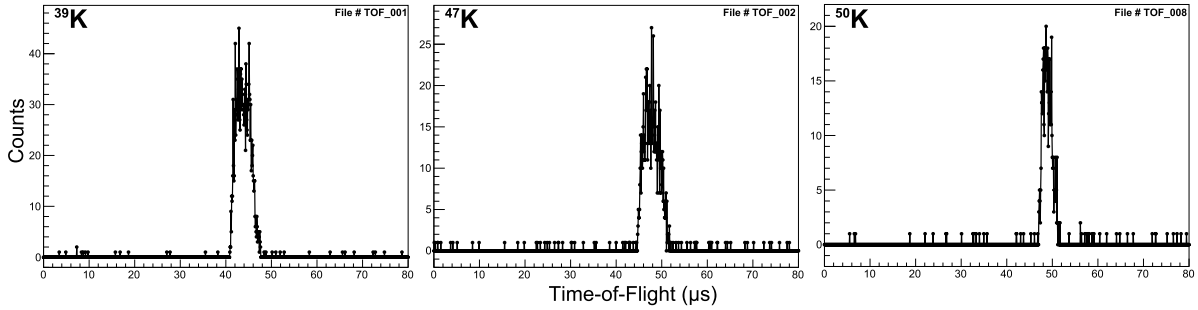

Figure 4.5: Time-of-flight spectrum of ^{39}K, ^{47}K and ^{50}K. Shown are the counts of one PMT as a function of flight time. For details see text.

Finally, the wavelength (used is the wavenumber $1/\lambda$) of the laser was set to $\lambda_1^{-1} = 13003.1200\,\mathrm{cm}^{-1}$, read-out value at the wavelength meter. Due to a limitation in the locking system, the wavelength had to be changed in the middle of the measurement campaign. The second wavelength was $\lambda_2^{-1} = 13003.1109\,\mathrm{cm}^{-1}$. The wavelength-meter software allows to record the measured wavenumber over time. Mean values were thus used for the data analysis, $\bar{\lambda}_1^{-1} = 13003.12017\,\mathrm{cm}^{-1}$ for the former and $\bar{\lambda}_2^{-1} = 13003.11096\,\mathrm{cm}^{-1}$ for the latter nominal value. Based on these wavelengths, the voltages for the Fluke 410B power supplies were set for each isotope. For example, in the case of ^{47}K the voltage was set to $U_{off}(\lambda_1) = -1300\,\mathrm{V}$ and $U_{off}(\lambda_2) = -1500\,\mathrm{V}$. For comparison, the measurement on ^{38}K was performed with $U_{off}(\lambda_2) = +6230\,\mathrm{V}$, for ^{50}K a voltage of $U_{off}(\lambda_1) = -4250\,\mathrm{V}$ was used. The Fluke voltage is recorded by the MCP after every scan. For the analysis of the spectra, the recorded values and not the nominal values were used. Table C.1 gives an overview of the used settings for all isotopes.

4.1.1 Measured HFS Spectra

In the experiment carried out in 2010 we recorded HFS spectra for nine potassium isotopes and one isomer: $^{38g,38m,39,42,44,46-50}$K. The spectra discussed in this section are gated spectra, which were recorded using the bunched-beam technique, unless otherwise stated. A detailed analysis and discussion of the results may be found in chapter 5. Figure 4.6 shows spectra of the isotopes $^{46-49}$K. Shown is the sum of the counts in all four photomultiplier tubes as a function of the DAC voltage. The spectrum of ^{46}K is the sum of two scans, that of ^{47}K consist of one scan, and that of ^{48}K comprises four scans. In the case of ^{49}K, six (five) scans were recorded for the left (right) multiplet, a spectrum normalized to five scans is thus shown. One scan represents a complete

hyperfine structure recorded with one proton pulse per DAC voltage and takes about 7 Min for ^{47}K.

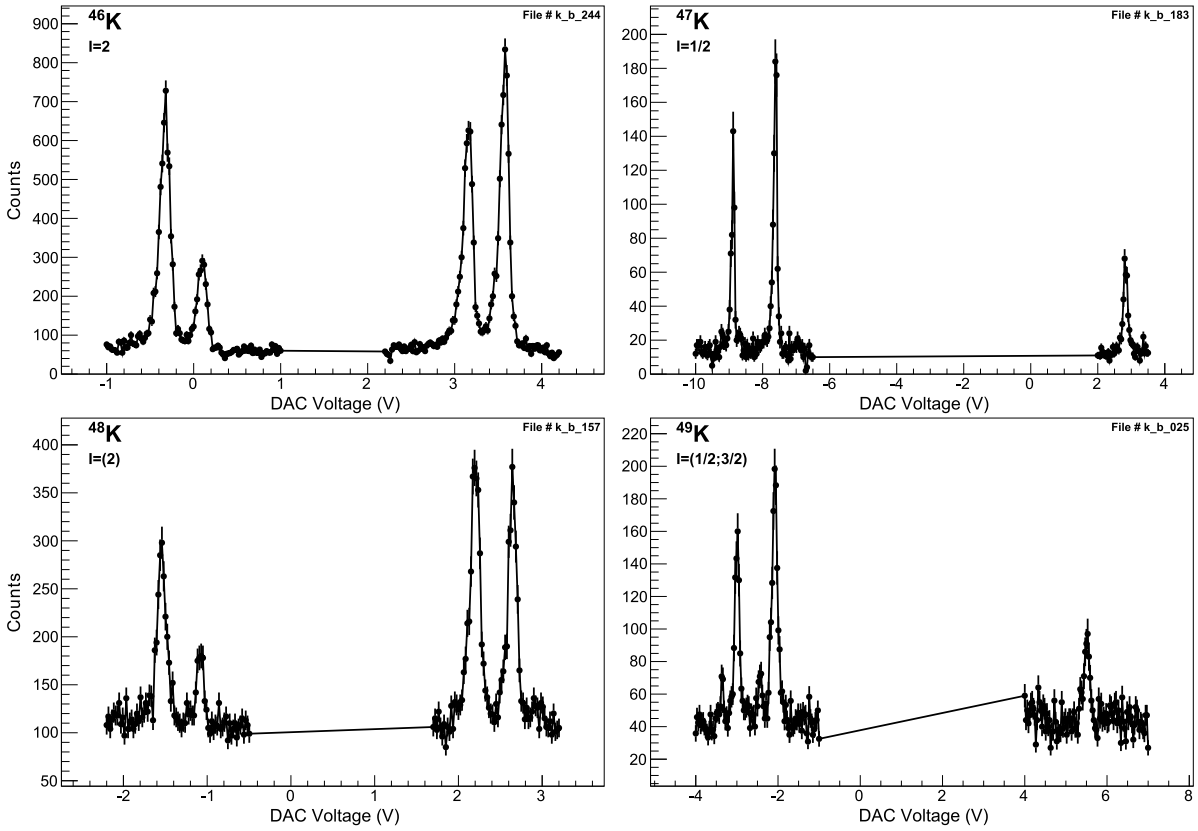

Figure 4.6: Gated raw spectra of $^{46-49}$K. Shown is the sum of the counts in all four PMTs as a function of the DAC voltage. The data points are connected to guide the eye. For details see text.

Already from the raw spectra new results can be obtained. From Eq. (2.4) and the selection rules given in Eq. (2.15), one can obtain the number of possible transitions for the used D1 line ($J_g = 1/2 \rightarrow J_e = 1/2$ transition) in potassium for a given ground-state spin. A ground-state spin $I = 0$ exhibits no hyperfine structure ($\Delta E_{HFS} = 0$). Therefore only one peak appears in the spectrum. For a ground-state spin of $I = 1/2$ it follows that three transitions are possible, resulting in three peaks in the hyperfine spectrum. For a spin $I > 1/2$ four transitions are possible. The obvious presence of only three peaks in the spectrum of ^{49}K rules out the possibility of a ground-state spin of 3/2 as proposed in [52]. The difference in the relative peak heights between ^{46}K and ^{48}K hints at a different ground-state spin of ^{48}K compared to ^{46}K. The spectra of ^{42,44}K support this difference (see figure B.1 in the appendix).

Figure 4.7 shows the spectrum of the ^{38}K ground (g) and isomeric state (m). The spectrum is the sum of six scans for the ground state and 12 scans for the isomeric state normalized to six scans. The spectra for ground and isomeric state were recorded under

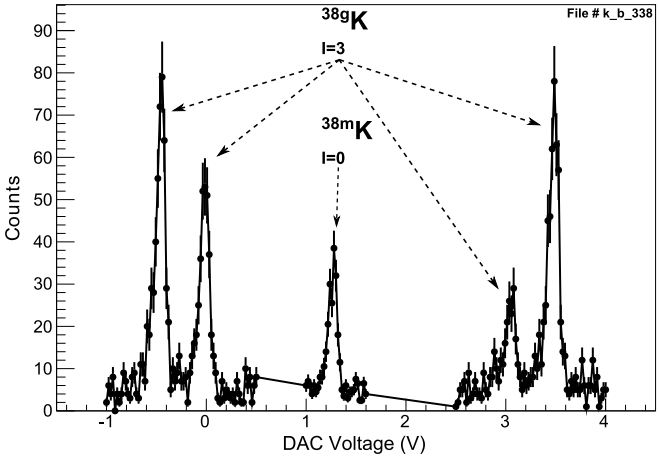

Figure 4.7: Gated raw spectra of ^{38}K ground and isomeric state. Shown is the sum of the counts in all four PMTs as a function of the DAC voltage. The data points are connected to guide the eye. Indicated in the spectrum is the assignment of the peaks to the $I = 3$ ground state and to the isomeric state with nuclear spin $I = 0$.

identical experimental conditions using a scan file with three tracks. It is indicated in the figure which peaks belong to the $I = 3$ ground state and which belong to the $I = 0$ isomeric state.

Two spectra recorded for ^{50}K and presented in figure 4.8 show only one peak resulting in a ground-state spin of $I = 0$. The left spectrum in figure 4.8 covers a broad scan range to include signatures of the proposed ground-state spins $I = 0, 1$, and 2. It is the sum of eleven scans. The right spectrum in figure 4.8 is a fine scan with better resolution and is the sum of ten scans. It is converted to frequency as discussed in the next section.

4.1.2 Conversion of the Raw Data

To extract nuclear ground-state properties from the recorded data, the spectra have to be converted to the frequency domain for the full analysis. The x-axis of the recorded spectra is converted from DAC voltage to frequency according to Eq. (2.33). The acceleration voltage thus has to be exchanged by $U = U_{DAC} * a_{Kepco} + U_{off} + U_{acc}$ as discussed in section 3.2.3. DAC and offset voltage (Fluke voltage) are recorded in the raw data files. The acceleration voltage U_{acc} of ISCOOL is measured by a high-voltage divider (FUG 1:10000), which is connected to a digital voltmeter (Prema 6040) and is regularly read out and written down by hand. The amplification factor a_{Kepco} of the linear voltage amplifier is determined by analyzing so-called "Kepco scans". To this end, the DAC voltage is scanned from $-10\,\mathrm{V}$ to $+10\,\mathrm{V}$ in $0.2\,\mathrm{V}$ steps and the voltage is recorded for every step. This is done regularly during the measurement campaign for all three Fluke power supplies to check the amplification of the linear-voltage amplifier (Kepco). The slope of the resulting graphs is the amplification factor a_{Kepco}. Figure 4.9

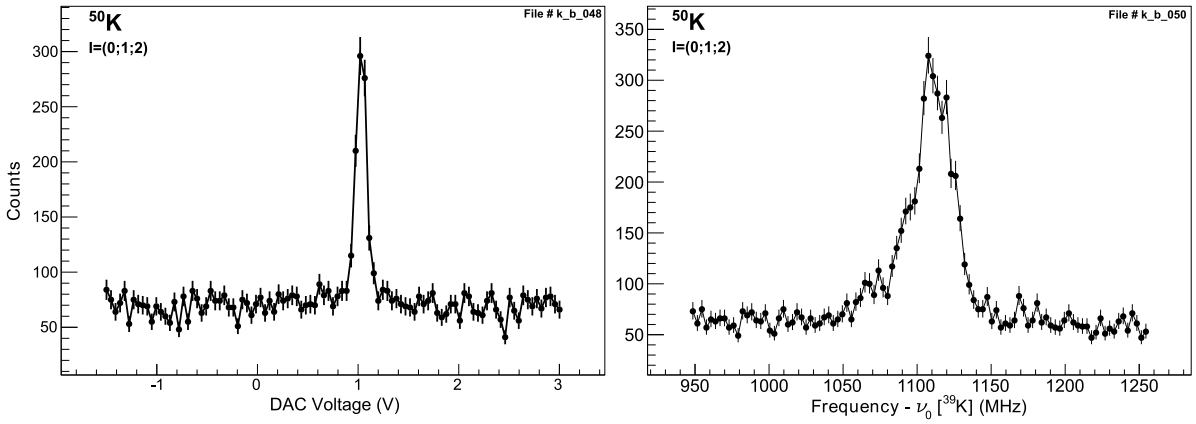

Figure 4.8: Gated raw spectra of ^{50}K. Shown is the sum of the counts in all four PMTs as a function of the DAC voltage in the left plot and as a function of shifted frequency in the right (see section 4.1.2). The data points are connected to guide the eye. For details see text.

gives the amplification factor as a function of file number (file #) for all three Fluke power supplies (points in the graph). The lines represent the weighted mean values for the individual Flukes and the combined weighted mean (all Flukes) used for the analysis. The left graph in figure 4.9 shows all values, the right graph a zoomed view. The origin

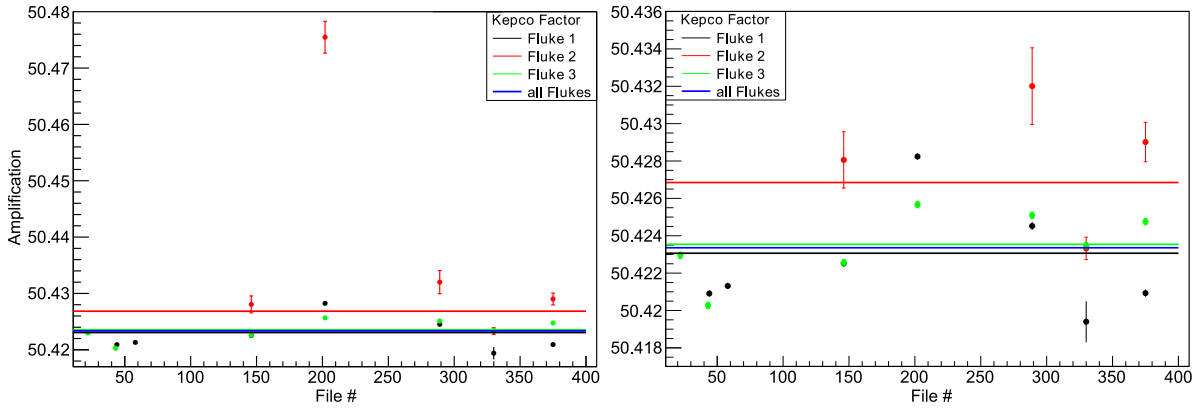

Figure 4.9: Amplification factor of the Kepco linear voltage amplifier as a function of file number (file#) for each Fluke power supply. The solid lines represent the weighted mean for each Fluke (black, red, and blue) and for all (blue). For details see text.

of the larger errors in the results for Fluke 2 are not fully understood. An instability of the power supply itself could be excluded after a test of its stability after the end of the experiment. The resulting weighted mean (Eq. (5.1)) of all three Flukes gives an amplification factor of $a_{Kepco} = 50.4233(5)$.

The masses of the potassium isotopes needed for the conversion using Eq. (2.33) are taken from table 4.1. For the frequency of the laser ν_0 entering Eq. (2.33) the recorded mean value as discussed in section 3.2.2 is used. In order to have the frequencies centered around $\nu = 0$, the transition frequency $\nu_{D1} = 389286058.716(62)\,\text{MHz}$ of the D_1 line of ^{39}K [85] is subtracted from the converted frequencies. As an example a converted spectrum of ^{50}K is given in figure 4.8 (spectrum on the right). Due to the low background counts (N) in most scans, compare for example figure 4.7, the normal symmetric $\sqrt{N}$ error cannot be used. For the analysis asymmetric errors were used. They can be calculated from the recorded counts via [86]

$$\sigma_{low} = \sqrt{N + 1/4} - 1/2; \qquad \sigma_{high} = \sqrt{N + 1/4} + 1/2. \tag{4.1}$$

As an illustration the reader is referred to figure 4.10, where the difference in the error bars for low count rates is clearly visible. For high count rates the asymmetric error converges to the symmetric error.

For the analysis, the data of the first and second row of photomultiplier tubes (see figure 3.6) are analyzed separately. Due to optical pumping the Lorentz width increases in the second row. For the hyperfine spectra recorded with 0.2 mW laser power, this effect results in an increase of the Lorentzian width in the second row by about 6 MHz. Additionally, single scans are used for fitting whenever possible, otherwise the graphs are normalized to counts/scan.

4.1.3 Defining the Used Line Shape

Figure 4.10 shows the left multiplet of the hyperfine structure (HFS) of ^{47}K with a fit of the HFS using Voigt profiles in the left spectrum and a multiple Voigt profile in the right spectrum. It is clearly visible in the left spectrum that the symmetric line shape of

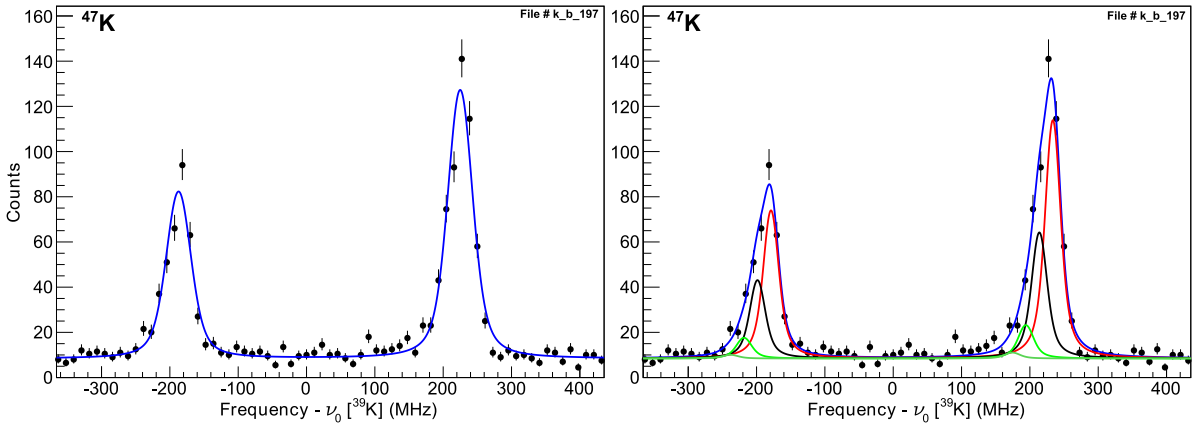

Figure 4.10: Fit of ^{47}K using a Voigt profile (left spectrum) and a multiple Voigt profile (right spectrum). Shown is only the left multiplet of the hyperfine structure. For details see text.

the Voigt profile (blue solid line) used does not describe the measured hyperfine peaks. As discussed in section 2.6, the charge-exchange processes introduce an asymmetry in the observed line shape. To account for this, a fit combining multiple Voigt profiles was used. The right spectrum in figure 4.10 shows the same spectrum as the left but fitted with a line shape (blue solid line) consisting of four Voigt profiles (differently colored solid lines). The main peak ($n = 0$, red) corresponds to no collisional excitation, the three side peaks to $n = 1, 2, 3$ (black, light green, dark green) collisional excitations. The energy which matches best the displacement of the side peaks to the main peak is that of the transition $4s\ ^2S_{1/2} \rightarrow 5p\ ^2P_{1/2} = 3.06\,\text{eV}$ taken from [56]. The number of side peaks has been determined using this energy by fitting multiple spectra of ^{47}K. Four peaks describe best the measured line shape for a collisional-excitation energy of $E = 3.06\,\text{eV}$, which was kept constant in the further data analysis. Lorentzian and Gaussian widths of the four Voigt profiles are fitted but kept identical for the individual peaks. In addition, the peak heights are determined using Eq. (2.41) with the Poisson factor x as fit parameter. For the analysis of the 2010 data, Lorentzian width and Poisson factor were fixed to the mean value resulting from fits to all spectra recorded for ^{47}K for which the parameters were allowed to evolve freely. The resulting Poisson factor is $x = 0.506$ for all laser powers used. The Lorentzian widths for the scans with 0.2 mW laser power are 16.8 MHz for the first and 22.8 MHz for the second row of PMTs, respectively. For the scans with 1.2 mW laser power the resulting Lorentzian widths are 26.6 MHz for the first and 32.7 MHz for the second row, respectively. The line shape defined in this way was used to fit all recorded spectra, also those for the ^{47}K data previously fitted with no fixed parameters. The right spectrum in figure 4.10 was fitted with the parameters for 0.2 mW laser power, the left spectrum was fitted with a standard Voigt profile. The agreement of the fit with the data is represented by the reduced chi-square χ^2_{red} of the fit (see section 5.2). The fit with the Voigt profile results in a $\chi^2_{red} = 2.2$, the multiple Voigt profile has a $\chi^2_{red} = 1.5$ confirming that the line shape found gives a better description of the data.

4.1.4 Voltage Calibration

The acceleration voltage of the cooler and buncher ISCOOL (U_{acc}) is measured with a precision of 0.2%, as specified for the used voltage divider. This results in an uncertainty of the ISCOOL voltage of 80 V at 40 kV acceleration voltage, which is not acceptable for the precision aimed at in this work. Therefore, the voltage is determined by comparing the isotope shifts (IS) with respect to ^{47}K ($\delta\nu^{47,A}$) obtained with the measured ISCOOL voltages to the corresponding ones from Touchard *et al.* [34], see figure 4.11. The green dots were obtained using the measured ISCOOL voltages which need to be corrected to match the literature values. Calculating this voltage correction for the four isotopes ^{38,42,44,46}K requires to change the voltage by $-11.5(2.3)\,\text{V}$ as weighted mean. The red dots show the isotope shift differences obtained with the corrected voltage. For the final analysis, the measured ISCOOL voltages are each corrected by $-11.5(2.3)\,\text{V}$ and all spectra are fitted with the resulting new voltage.

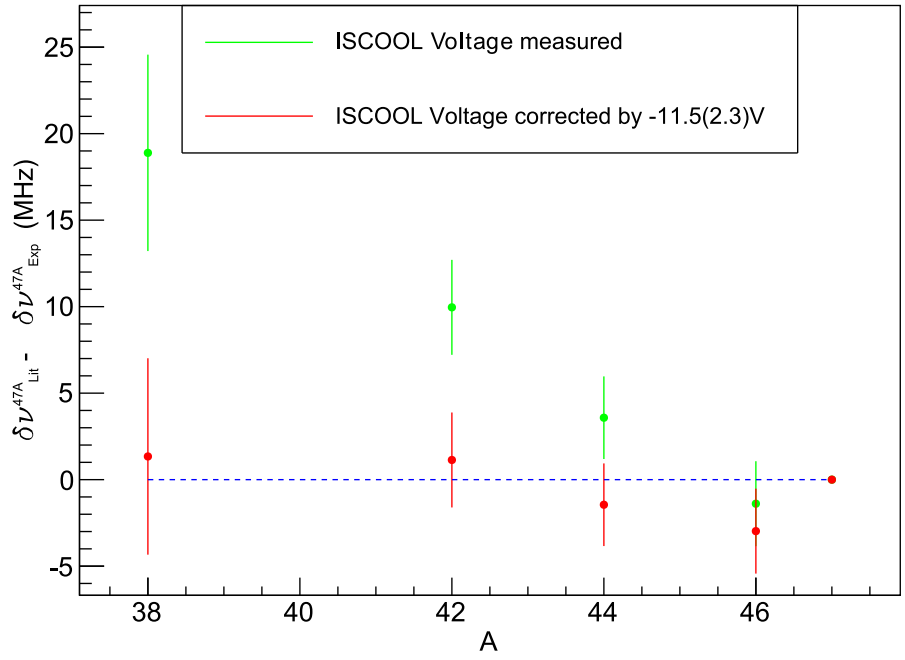

Figure 4.11: ISCOOL voltage calibration of the 2010 data. Shown is the differential isotope shift of our experimental data to the literature values from Touchard *et al.* [34] for the measured voltages (green dots) and corrected by $-11.5(2.3)$ V (red dots). For details of the correction see text.

4.1.5 Problems with Beam Light and Changes for the 2012 Experiment

In the 2010 experiment, it has not been possible to observe the isotope ^{51}K. The main reasons are a high background from isobaric contamination and the measured yield of only about 3000 ions/proton pulse (pp) for ^{51}K. The background for the mass of ^{51}K was about a factor of 3 higher than for ^{49}K (7 counts per proton pulse (pp) compared to 2.5 counts/pp in the gated spectra with laser beam blocked). With a detection efficiency of the new LCR of 1 photon per 20000 potassium ions this would result in 1 signal photon per 7 proton pulses on a background of about 49 counts. The low yield in combination with the high background made the measurement impossible. The high background level originates from beam light generated by contaminating ions non-resonantly excited in the charge-exchange medium or in the rest gas. Since the transition in potassium is in the infrared (770 nm) a possible solution to reduce the background from beam light is to block all wavelengths below the used one. A suitable filter is the RG715 color glass filter from SCHOTT, which blocks all wavelengths below 715 nm and transmits light with larger wavelengths with up to 90 % transmission. At the end of the 2010 experiment it was possible to test the efficiency of the long-pass glass filter with an ion beam from an irradiated UC_x target. A 1.5-inch RG715 filter was mounted in front of the second photomultiplier tube on the right side (with respect to the ion beam direction), R2.

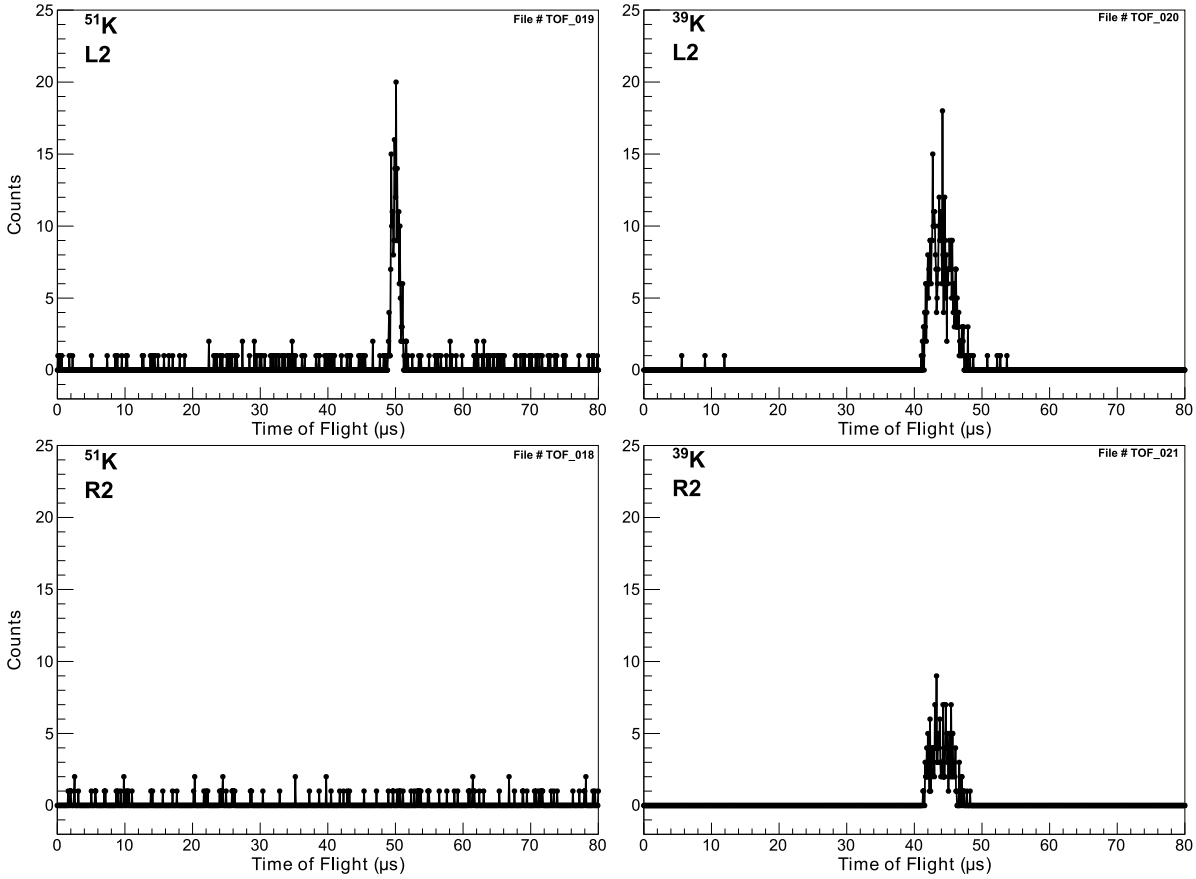

Figure 4.12: Time-of-flight spectra for ^{51}K and ^{39}K without RG715 Filter (L2, top row) and with (R2, bottom row). Shown are the counts of one PMT as a function of flight time. For details see text.

Figure 4.12 shows the time-of-flight spectra of the PMTs R2 and L2 (without RG715) for the mass of ^{39}K and ^{51}K. All spectra represent 20000 bunches, except for the spectrum of ^{51}K for R2, where 40000 bunches were collected. Since the proton impact had been stopped, the beam is expected to be composed of stable or long-lived potassium isotopes and contaminating ions, respectively. While knowledge of the exact composition of the beam is not necessary, it is clearly visible that on the mass number of the short-lived ^{51}K all beam light entering the PMT L2 originates from isobaric contaminants because the filter completely cuts it, giving no signal in PMT R2. On the mass of ^{39}K, where we expect the main beam component to be stable potassium, the signal measured with PMT L2 is also visible with the RG715 filter in front of R2. The reduction of counts by a factor of two is caused by a transmission loss, mainly due to the filter itself but also due to the reduced solid angle. In addition the mount of the 1.5-inch filter cuts some of the incoming ion-beam light.

After this promising test, the light-collection chamber was re-designed to accommodate a 3-inch RG715 filter in front of each of the four PMTs. Figure 4.13 shows a

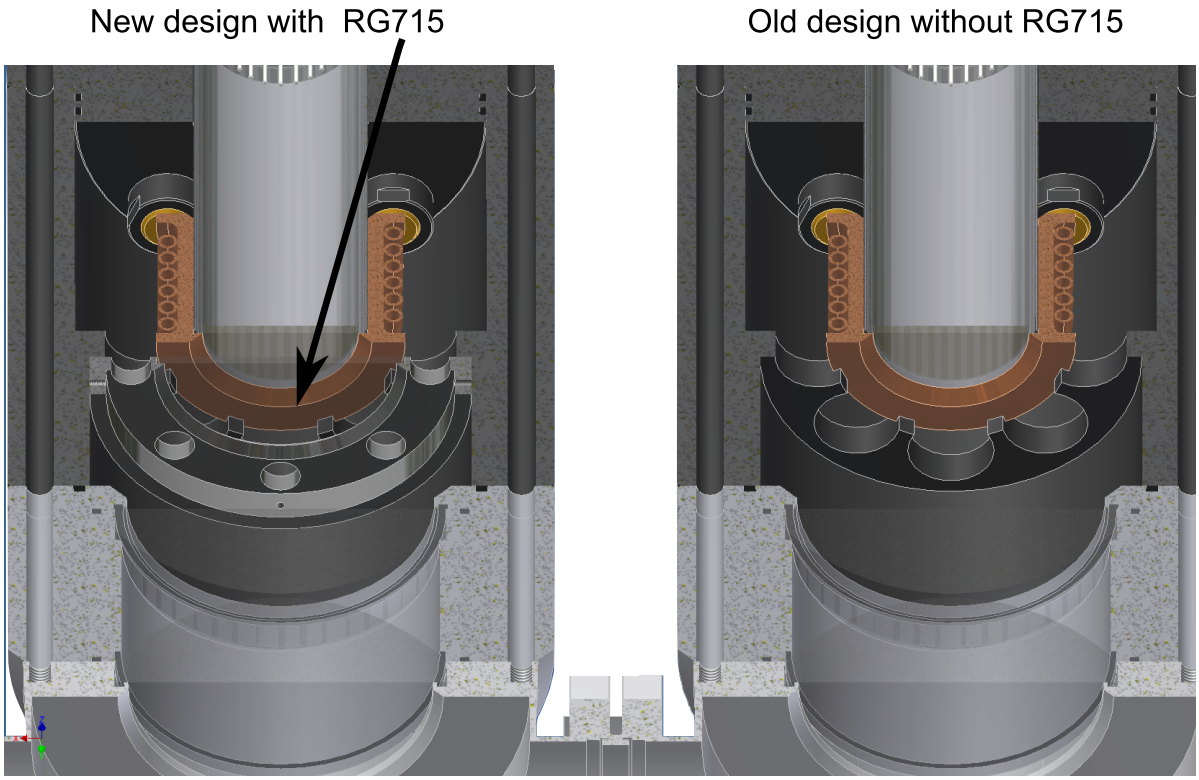

Figure 4.13: Technical drawing of the new LCR with RG715 and mount (left chamber) and without (right chamber). Adapted from Ref. [79]

comparison of the old design and the new design with RG715 filter used in the 2012 experiment. Transmission losses due to the mount were reduced and a larger solid angle was provided.

4.2 The 2012 Experiment

As already discussed in section 3.2.2, for the 2012 experiment a new laser system was used. With the improved beam quality of the Matisse TS laser and improved out coupling of the laser light we could decrease the background from scattered laser light to about 500 counts/s/mW combined for all four PMTs. The dark-count rate of the PMTs was about 850 counts/s for all four PMTs similar to the 2010 experiment. The replacement of the broken charge-exchange cell uses a different heating wire with a resistance of $R_{CEC} = 29\,\Omega$ instead of the $35\,\Omega$ of the 2010 experiment. In order to have a better efficiency for the measurement of ^{51}K, the charge-exchange-cell temperature was increased. The voltage was set to $U_{CEC} = 24.8\,\mathrm{V}$ resulting in a current of $I_{CEC} = 0.85\,\mathrm{A}$ and a temperature of 5.5 mV. At this temperature, a neutralization efficiency of more than 80 % was reached. The laser power was set to $P_{laser} = 1.2\,\mathrm{mW}$ during the entire experiment. Due to the lower background from beam light, the timing could be adjusted accordingly. The

accumulation time and the number of used bunches could be increased compared to the 2010 experiment. In 2010, up to 6 bunches with an accumulation time of 45 ms were used. Now up to 7 bunches with an accumulation time of 60 ms could be used. Since the lower background also results in a better signal-to-noise ratio, the time used after proton impact could be increased from 270 ms to now 420 ms. The gates for the bunched-beam spectroscopy were set to the same values as in 2012 except for ^{47}K. In 2010 a delay of $t_d = 45\,\mu$s with a width of $t_w = 7\,\mu$s was used, now the delay was set to $t_d = 46\,\mu$s and the width to $t_w = 4\,\mu$s. For the new isotope ^{51}K the delay was set to $t_d = 48\,\mu$s with a width of $t_w = 4\,\mu$s.

The next parameter to be set is the laser wavelength. In 2012 the wavelength (used is the wavenumber $1/\lambda$) of the laser was set to $\lambda^{-1} = 13003.0985\,\mathrm{cm}^{-1}$, read out on the wavemeter. The mean value used for the data analysis is $\bar{\lambda^{-1}} = 13003.09879\,\mathrm{cm}^{-1}$. Figure 4.14 shows the recorded wavenumber for the 2010 and 2012 experiment over

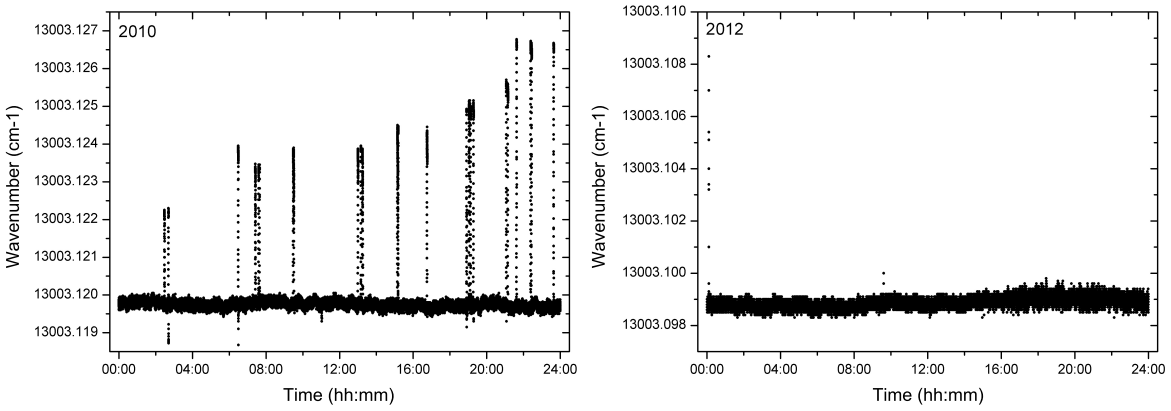

Figure 4.14: Comparison of the long-term stability of the used laser systems in 2010 and 2012. Shown is the wavenumber recorded over 24 hours. For details see text.

24 hours. The data represents a full day starting and ending at midnight. The left graph shows the recorded wavenumber for the 2010 experiment. It contains several spikes originating from drifts in the Coherent 899 laser cavity forcing the laser system to be manually relocked to the long term stabilization. Whenever such a spike occurred, the laser was no longer in resonance and no signal was recorded. Thus the scan had to be rejected in the data analysis. This happened for about 5 % of all scans. The right graph shows the recorded wavenumber for the 2012 experiment, which used the Sirah Matisse TS laser system. In contrast to the 2010 experiment only a few spikes are visible. The spikes did not happen during a hyperfine structure scan and therefore no scans had to be rejected for the analysis.

Based on the wavelength set for the 2012 experiment, the voltages for the Fluke 410B power supplies were set accordingly for each isotope. For example, in the case of ^{47}K the voltage was set to $U_{off} = -1470\,\mathrm{V}$. All other parameters and settings were the same as

in the 2010 experiment. Table C.1 gives an overview of the used settings for all isotopes.

4.2.1 Measured HFS Spectra

In the experiment carried out in 2012, we recorded HFS spectra for six potassium isotopes and one isomer: ^{38g,38m,39,42,47,50,51}K. Unless otherwise stated the spectra shown are gated spectra. A detailed analysis and discussion of the results is part of chapter 5.

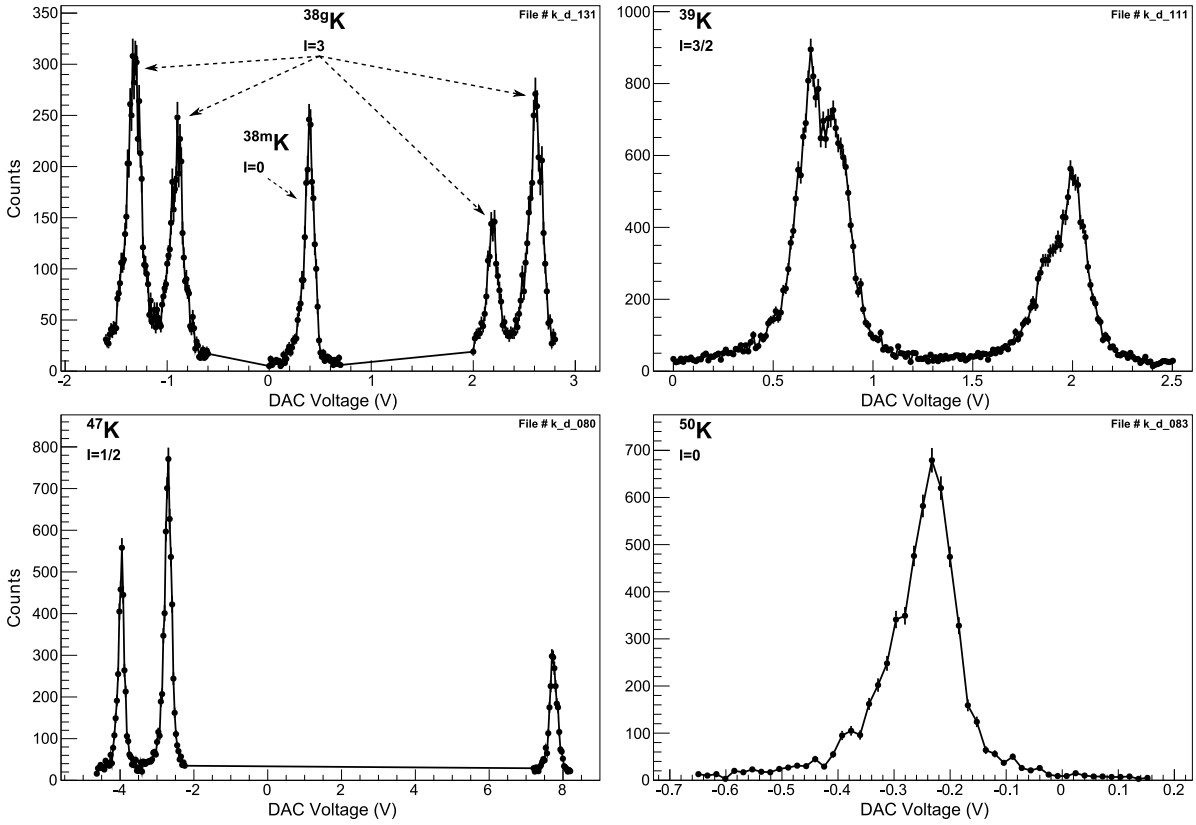

Figure 4.15: Gated raw spectra of ^{38,39,47,50}K. Shown is the sum of the counts in all four PMTs as a function of the DAC voltage. The data points are connected to guide the eye. For details see text.

Figure 4.15 shows spectra of the isotopes ^{38,39,47,50}K. The spectra are made from the sum of the counts in all four photomultiplier tubes as a function of the DAC voltage. The spectrum of ^{38}K is the sum of 10 scans, that of ^{39}K consist of 15 scans, that of ^{47}K comprises 5 scans, and that of ^{50}K consists of 15 scans. The peaks of the ground state in the spectrum of ^{38}K show a higher background because the scan range was narrowed down and cuts the tails of the peaks. The real background is at the same level as seen in the isomer. The spectrum of ^{39}K from figure 4.15 shows the effect of the higher charge-exchange-cell temperature and laser power compared to figure B.2. The structure is broader and less resolved. In addition, two obvious changes are visible in

the raw spectra. First, the background level is lower, compare for example the spectrum of ^{47}K to the one in figure 4.6. This is the result of the suppression of the beam light from isobaric contamination by the RG715 filter. Second, the yield from the target was higher. This can be seen for example in the spectra of ^{50}K and ^{38}K. In both spectra, the count rate is higher compared to the spectra recorded in the 2010 experiment (figures 4.7 and 4.8). As a result of the higher yield and lower background the signal-to-background ratio (S/B) was higher in 2012. For ^{47}K the S/B increased by a factor of two, for ^{50}K the S/B increased by more than a factor of 40. Figure 4.16 shows the spectrum of ^{51}K

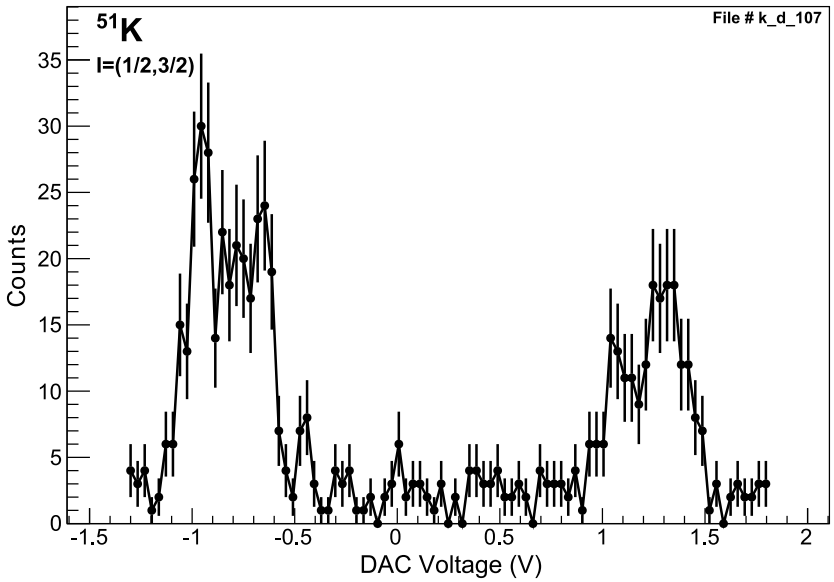

Figure 4.16: Gated raw spectrum of ^{51}K. Shown is the sum of the counts in all four PMTs as a function of the DAC voltage. The data points are connected to guide the eye. For details see text.

which consists of 95 scans and was recorded over a total time of 8 hours separated by reference scans on ^{47}K every 2 hours. From the spectrum it is clearly visible that the spin of ^{51}K cannot be 1/2 since four peaks are visible. The background count rate could be reduced from 7 counts per proton pulse (pp) to about 0.02 counts/pp with the RG715 filter installed as discussed in section 4.1.5. During the experiment five such spectra were recorded for data analysis. The spectrum of ^{42}K is shown in figure B.3 in the appendix.

The conversion to frequency is done in the same way as described in section 4.1.2. The amplification factor a_{Kepco} for the 2012 experiment was determined to be $a_{Kepco} = 50.4261(12)$. For the analysis the data of all isotopes were split into the first and second row of photomultiplier tubes, except for ^{51}K due to low statistics.

4.2.2 Defining the Used Line Shape

The ^{47}K files were fitted with free parameters to define the Poisson factor (x). The Poisson factor was determined to $x = 0.607$. In contrast to the 2010 experiment, the

Lorentzian width is not fixed because the observed width is smaller for ^{50}K and ^{38m}K compared to the remaining isotopes. This effect is not yet fully understood. A possible explanation are optical-pumping effects populating dark states only occurring for isotopes with ground-state spin $I > 0$. The peak height of the hyperfine structure is then artificially reduced resulting in larger Lorentzian widths, which can be nicely seen in the spectrum of ^{38}K shown in figure 4.15. For the data analysis the same line shape as defined in section 4.1.3 was used.

4.2.3 Voltage Calibration

The voltage calibration for the 2012 data was not done against the literature data from Touchard but against our 2010 isotope shifts to get a consistent data set. Figure 4.17 shows the differences in isotope shift between the experimental data of 2012 and 2010 for the measured ISCOOL voltages (green dots). The correction voltage was calculated to a mean value of $-14.7(8)$ V with which the final analysis was performed.

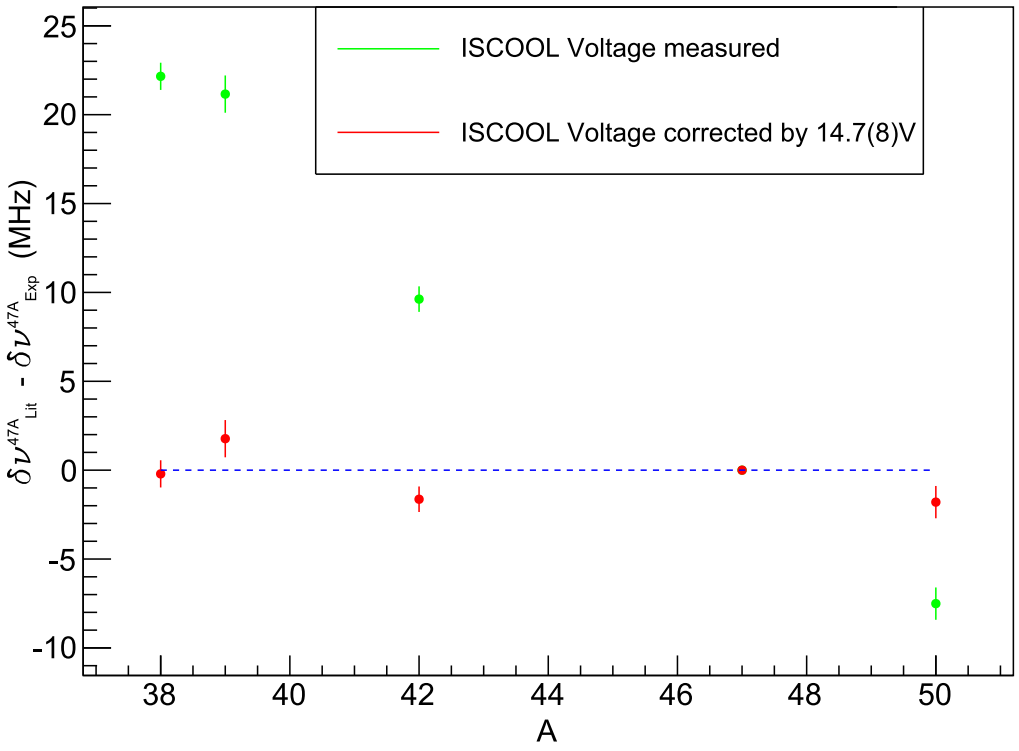

Figure 4.17: ISCOOL voltage calibration of the 2012 data. Shown is the differential isotope shift of our experimental data from 2012 against the 2010 data for the measured voltages (green dots) and corrected by $-14.7(8)$ V (red dots). For details of the correction see text.

5 Results

This chapter presents the results of the analysis of the measured hyperfine spectra presented in chapter 4. The nuclear ground-state properties which were deduced from the hyperfine spectra within the context of this thesis are, on the one hand the spins of ^{48,49,50,51}K. On the other hand, the changes in mean square charge radii extracted from the measured isotope shifts. As the charge radii of the isotopic chain ranging from ^{38}K to ^{51}K cross the two magic numbers $N = 20$ and $N = 28$, it will be shown how the existence and non existence of a shell closure can be deduced. Section 5.1 gives the newly measured ground-state spins of the four isotopes ^{48,49,50,51}K, which are summarized in table 5.1. In section 5.2 the measured A-factors and the calculated isotope shifts referenced to ^{47}K ($\delta\nu^{47A}$) from the two experiments and the combined results will be presented. Section 5.3 presents the calculation of the changes in mean square charge radii $\delta\langle r^2\rangle^{AA'}$ including the results for both experiments and the combined data. The last section 5.4 gives the extracted rms charge radii for the combined data. Discrepancies to literature values will be discussed.

5.1 Spin Determination of $^{48-51}$K

As mentioned in section 4.1.1, in the case of ^{49}K and ^{50}K the identification of the ground-state spin is based on the number of peaks visible in the measured hyperfine spectra. Figure 5.1 shows the fitted spectra of the two isotopes. The spectrum of ^{49}K (left

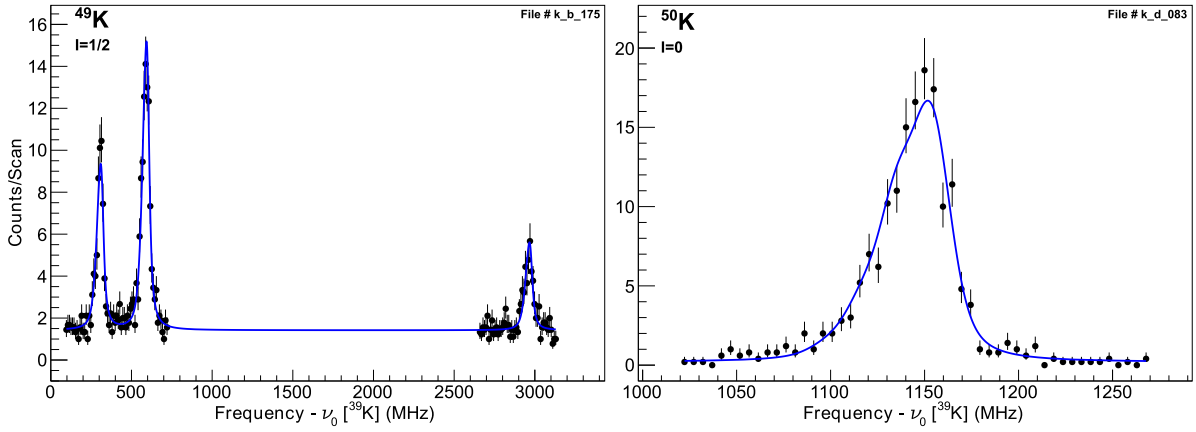

Figure 5.1: Fitted hyperfine spectra of ^{49}K from 2010 and ^{50}K from 2012 shown as counts/scan as a function of shifted frequency. For details see text.

spectrum) is taken from the 2010 data, the spectrum of ^{50}K (right spectrum) is from 2012. The recorded hyperfine spectra were converted to frequency and fitted with the line shapes defined for the two experiments as discusses in chapter 4. In the spectrum of ^{49}K, three peaks are visible. As the D1 transition in potassium ($J_g = 1/2 \rightarrow J_e = 1/2$) was used for spectroscopy, the possible transitions for a given ground-state spin can be obtained using Eq. (2.4) and the selection rules given in Eq. (2.15). Three transitions, resulting in three peaks in the spectrum, are only possible with a ground-state spin of $I = 1/2$. The ground-state spin of ^{49}K was thus determined to $I = 1/2$, which confirms the assignment of $I = 1/2^+$ proposed by Broda *et al.* [48]. In the spectrum of ^{50}K only one peak is visible,which is the characteristic feature of a ground-state spin $I = 0$. Thus, the ground-state spin of ^{50}K was determined to $I = 0$, which confirms the assignment of $I = 0^-$ proposed by Baumann *et al.* [53].

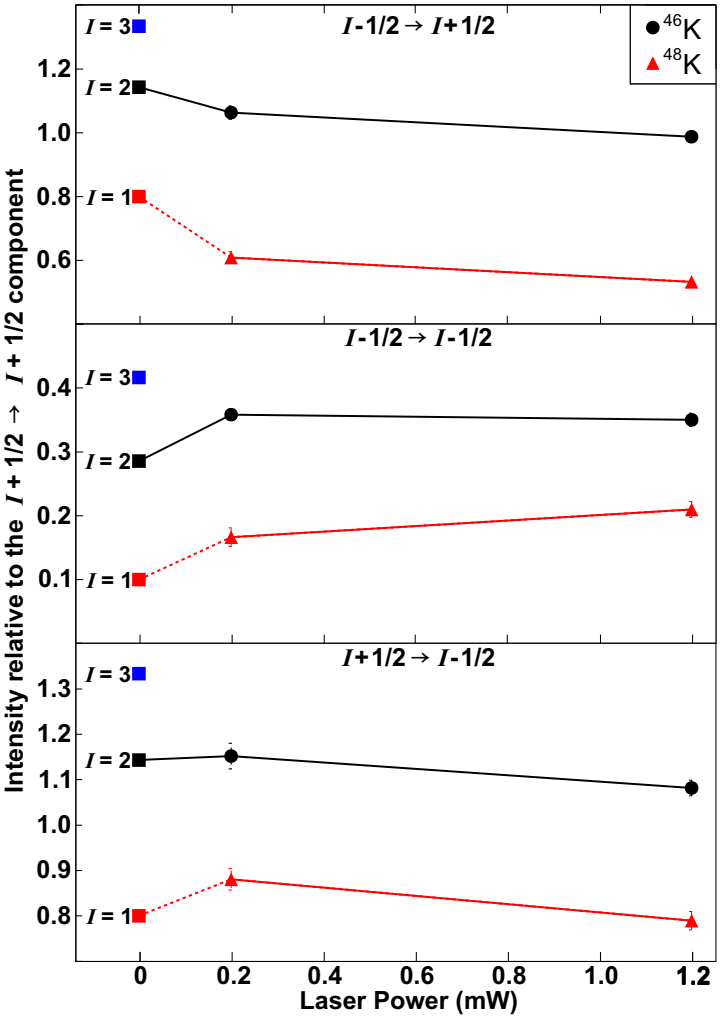

Figure 5.2: Intensities of the hyperfine components of ^{46}K and ^{48}K relative to the $I + 1/2 \rightarrow I + 1/2$ component as a function of laser power. For details see text.

For the isotopes of ^{48}K and ^{51}K, the situation is not as clear since four peaks are visible in the spectra. Four transitions between hyperfine levels are possible for every ground-state spin with $I > 1/2$. Here, a comparison of the relative intensities between the different hyperfine transitions is used to determine the spin. In the case of ^{48}K, the predicted ground-state spin is $I = 2$ based on decay spectroscopy measurements. To determine its spin, the measurements of ^{48}K are compared to those of ^{46}K which has a ground-state spin of $I = 2$.

Figure 5.2 shows the intensities of the individual hyperfine components relative to the $I + 1/2 \rightarrow I + 1/2$ component as a function of laser power. Data points are taken at $P = 0.2\,\mathrm{mW}$ and $P = 1.2\,\mathrm{mW}$. The relative intensities at $P = 0\,\mathrm{mW}$ correspond to the calculated intensities using Eq. (2.16). The hyperfine spectra of both isotopes have been recorded under identical experimental conditions, the only property that can thus cause a difference in the relative intensities is the nuclear spin. The relative intensities of ^{46}K and ^{48}K are well separated and do not overlap. Therefore, the spin of ^{48}K cannot be the same as the spin of ^{46}K. The two measurements of ^{46}K at $P = 0.2\,\mathrm{mW}$ and $P = 1.2\,\mathrm{mW}$ were connected to the relative intensity at $P = 0\,\mathrm{mW}$ known for a ground-state spin of $I = 2$ (represented by the solid line). The relative intensities of ^{48}K have to follow a similar trend when going to $P = 0\,\mathrm{mW}$ laser power. Following the trend of ^{46}K the relative intensities of ^{48}K converge to the value at $P = 0\,\mathrm{mW}$ corresponding to a ground-state spin of $I = 1$ (represented by the dashed line). We therefore obtain the spin of $I = 1$ for ^{48}K, which confirms the assignment of $I = 1^-$ proposed by Królas *et al.* [50].

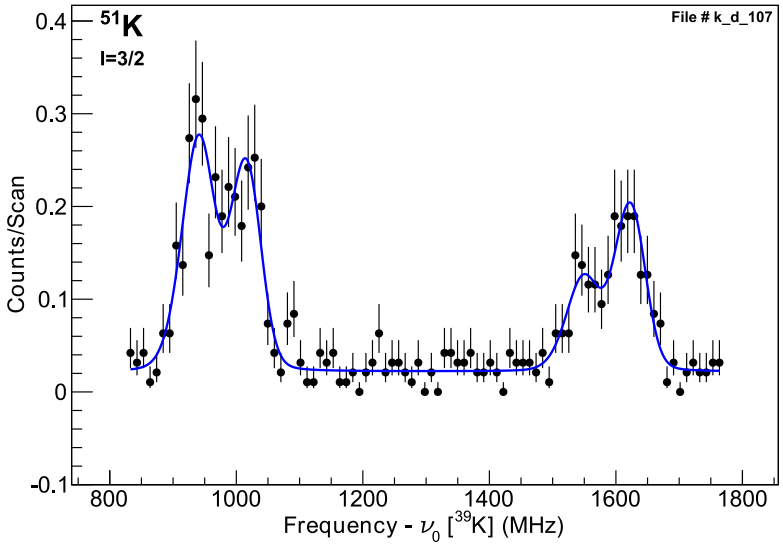

Figure 5.3: Hyperfine spectrum of ^{51}K shown as counts/scan as a function of frequency. The spectrum was fitted using a ground-state spin of $I = 3/2$.

For the determination of the ground-state spin of ^{51}K the situation is even more complex. A spin of $I = 1/2$ can be excluded since four peaks are visible in the recorded spectra. Figure 5.3 shows the hyperfine spectrum of ^{51}K with a fit assuming a spin of $I = 3/2$ which yields a good agreement with the data.

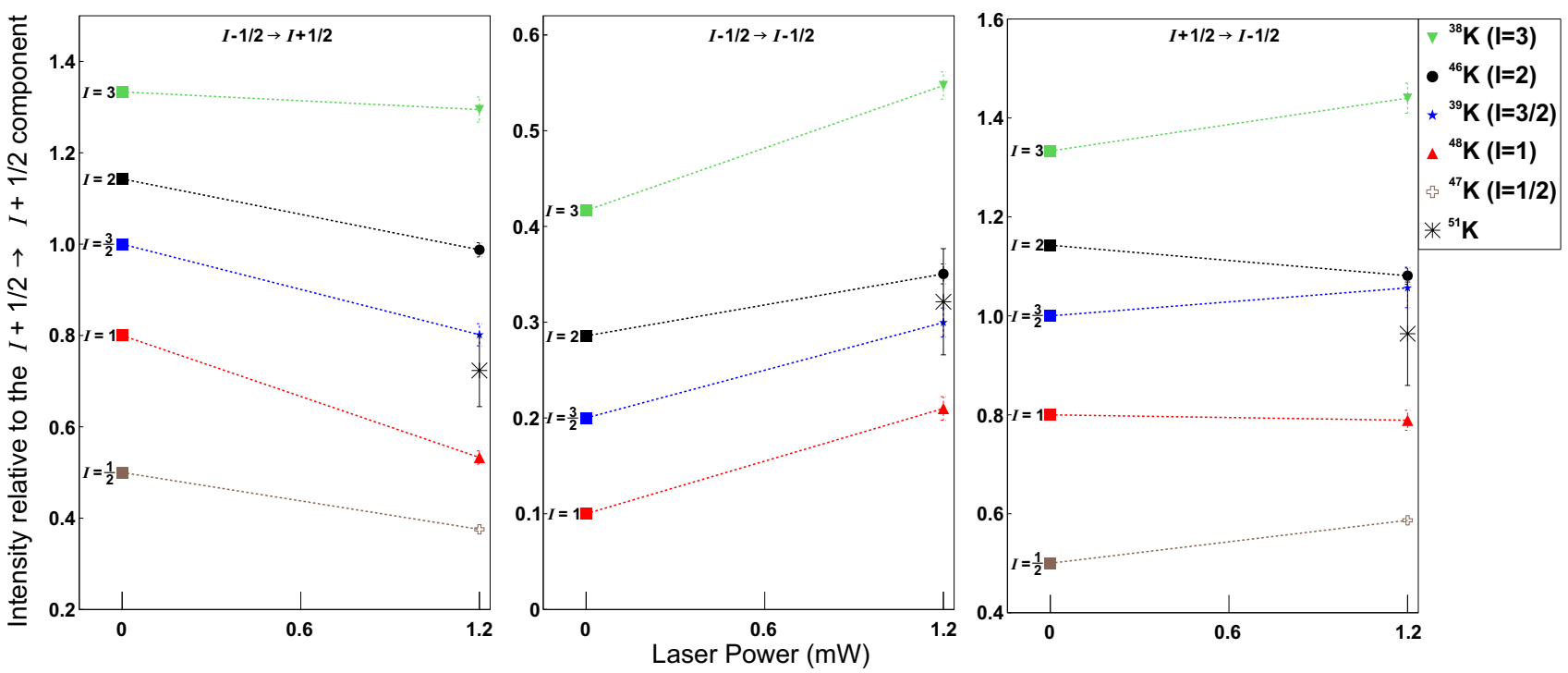

Figure 5.4: Intensities of the hyperfine components of ^{38,39,46,47,48,51}K relative to the $I + 1/2 \rightarrow I + 1/2$ component as a function of laser power. For details see text.

However, a fit with a spin of $I = 5/2$ delivers practically the same result apart from different A-factors and a different hyperfine structure centroid. This illustrates that this method alone cannot determine the ground-state spin of ^{51}K. Other methods to discriminate between the possible spins, e.g. using the isotope shift systematics, were discarded due to the same unambiguity of the results.

As in the case of ^{48}K, the nuclear spin was determined looking at the development of the relative intensities of the individual hyperfine transitions. A direct comparison with a particular isotope (e.g. ^{39}K) for different laser powers is not possible since the spectra for ^{51}K were recorded only for one laser power. The solution is to compare the relative intensities of the hyperfine components of ^{51}K with several isotopes at $P = 0\,\mathrm{mW}$ and $P = 1.2\,\mathrm{mW}$. Figure 5.4 shows these relative intensities of the individual hyperfine components relative to the $I + 1/2 \rightarrow I + 1/2$ component as a function of laser power for ^{38,39,46,47,48,51}K. Data points were taken at $P = 1.2\,\mathrm{mW}$, the relative intensities at $P = 0\,\mathrm{mW}$ correspond to the theoretically calculated intensities. Similar to figure 5.2, the data points are connected to the respective value at $P = 0\,\mathrm{mW}$ with a dashed line. The relative intensities of ^{51}K are denoted by as star and are not connected to a value at $P = 0\,\mathrm{mW}$. Within the error bars the relative intensities of ^{51}K agree with those for a ground-state spin of $I = 3/2$ corresponding to the spin of ^{39}K.

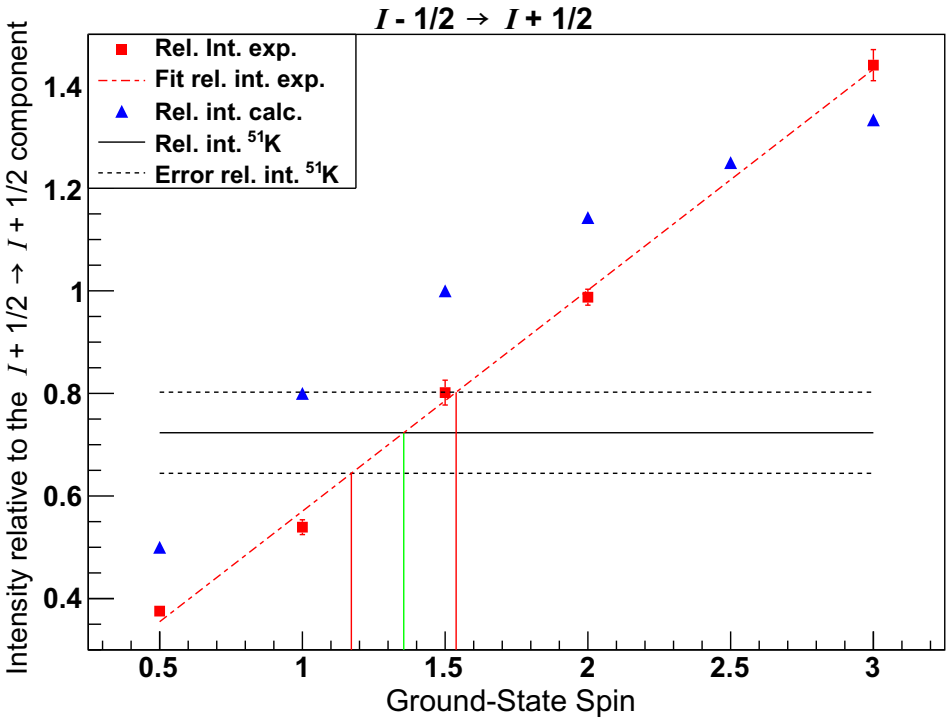

Figure 5.5: Intensities of the hyperfine component $I - 1/2 \rightarrow I + 1/2$ of ^{38,39,46,47,48,51}K relative to the $I + 1/2 \rightarrow I + 1/2$ component as a function of ground-state spin. For details see text.

To define a confidence level for the spin determination the observed relative intensities

were plotted against the spin. Figure 5.5 shows the intensities of the hyperfine component $I-1/2 \rightarrow I+1/2$ of ^{38,39,46,47,48,51}K (left plot of figure 5.4) relative to the $I+1/2 \rightarrow I+1/2$ component. These relative intensities of ^{38,39,46,47,48}K were fitted with a linear function, shown in the plot as a dot-dashed line. The relative intensity determined for ^{51}K is given as horizontal line shown with its error band (dashed lines). The intersection of the relative intensity of ^{51}K with the fitted line defines the ground-state spin with uncertainty estimates (green and red vertical lines). The confidence level for exclusion $I = 5/2$ (or higher) is 95 %. The plots for the two remaining intensity ratios from figure 5.4 confirm this level of confidence. As a result, we determine the ground-state spin of ^{51}K to $I = 3/2$ which supports the $I = 3/2^+$ assignment made by Perrot *et al.* [49]. Table 5.1 summarizes the determined spins of the four new potassium isotopes and compares them to the tentative assignments found in literature.

Table 5.1: Determined spins for ^{48,49,50,51}K. Literature values taken from [48–50, 53, 54, 84].

A	I Exp.	I^π Lit.
48	1	$(1^-, 2^-)$
49	1/2	$(1/2^+, 3/2^+)$
50	0	$(0^-, 1^-, 2^-)$
51	3/2	$(1/2^+, 3/2^+)$

5.2 A-Factors and Isotope Shifts Deduced from the Hyperfine Structures

The hyperfine structure parameters presented in this section are the results of χ^2-minimization fits applied to the data converted to a frequency scale as described in chapter 4. The fitting routines were constructed using the ROOT framework [87] based on the standard MINUIT fitting package. As mentioned in chapter 4, asymmetric errors on the counts were used for the analysis, which is implemented in the MINUIT fitting package. The multiple Voigt profile as defined in chapter 4 was used as line shape, taking the respective Voigt profile from [65]. As a measure of the quality of the fits, the reduced chi-square $\chi^2_{red} = \chi^2/d$ is used. Here, d is the number of degrees of freedom, which is defined as the number of data points minus the number of free fit parameters. For a fit which represents the data well, the reduced χ^2 should lie around 1. As standard procedure, the errors are multiplied by the square root of the reduced chi-square if $\chi^2_{red} > 1$. This multiplied error is then assigned as statistical error of the parameter which is used in the further analysis. This corresponds to a 68 % (1σ) confidence level.

To combine the results of n individual measurements, the mean of the value X_i

weighted by the errors σ_i on the individual measurements is calculated via

$$\bar{X} = \frac{\sum_{i=1}^{n} (X_i/\sigma_i^2)}{\sum_{i=1}^{n} (1/\sigma_i^2)}. \tag{5.1}$$

The standard deviation σ_A is then defined as

$$\sigma_A = \frac{1}{\sqrt{\sum_{i=1}^{n} (1/\sigma_i^2)}}. \tag{5.2}$$

If the individual measurements show a considerable scatter σ_A does not represent the true uncertainty. In this case the experimental standard deviation σ_B is introduced

$$\sigma_B = \sqrt{\frac{\sum_{i=1}^{n} (X_i - \bar{X})^2/\sigma_i^2}{(n-1)\sum_{i=1}^{n} (1/\sigma_i^2)}}. \tag{5.3}$$

The final error σ of $\bar{X}$ is calculated using

$$\sigma = max(\sigma_a, \sigma_B). \tag{5.4}$$

The weighted means of the results obtained in the analysis presented in this thesis were calculated using Eq. (5.1) and (5.4).

For the isotope shift measurements, the data were recorded in pairs of the reference isotope ^{47}K and the isotope of interest (^{38,39,42,44,46,48,49,50,51}K). In the case of ^{38}K, ground and isomeric state were recorded in the same scan using three tracks (see section 3.2.3). These pairs of data were individually analyzed as described in the following. For each isotope pair, the ISCOOL voltage is averaged over the recorded values. The mean voltage is used for the conversion of the raw data to frequency for both isotopes as described in chapter 4. In the final stage of the analysis, the ISCOOL voltage is corrected by the correction voltage as defined in the previous chapter. The pair of hyperfine spectra of the reference isotope ^{47}K and the isotope of interest are recorded simultaneously in the first and second row of photomultiplier tubes, which are fitted separately. The results of the fit procedure are the A-factors and the center of gravity (ν_{cg}) of the hyperfine structure of each isotope. If more than one pair of data is available, A-factors and ν_{cg} are combined using Eq. (5.1) and (5.4). Typically, each isotope shift measurement consist of two independent reference scans and at least two independent scans of the ion of interest. From the weighted mean value of the hyperfine centroids ν_{cg}, the isotope shift to ^{47}K ($\delta\nu^{47,A}$) is calculated applying Eq. (2.25)

$$\delta\nu^{47,A} = \nu_{cg}^{A} - \nu_{cg}^{47}. \tag{5.5}$$

This procedure is repeated for all available pairs, of which at least 3 independent pairs are available for each isotope shift measurement. The final values of the isotope shifts and the A-factors are the weighted means of the results of the individual pairs and the two photomultiplier rows. An exception is the isotope shift of the isomer ^{38m}K. Here, the isotope shift to ^{47}K ($\delta\nu^{47,38m}$) is calculated using the isomer shift $\delta\nu^{38g,38m}$ and the isotope shift of the ground state $\delta\nu^{47,38g}$. The final value is calculated with the weighted mean of the isomer shift $\delta\nu^{38g,38m}$ and the isotope shift $\delta\nu^{47,38g}$.

5.2.1 The Isotope Shifts

Table 5.2 gives the final values of the isotope shifts $\delta\nu^{47,A}$ measured in the two experiments of 2010 and 2012 as well as the weighted mean of the two experiments. The statistical errors are given in round brackets, the systematic errors arising from the uncertainty of the beam energy are given in square brackets. The literature values given in table 5.2 are referenced to ^{47}K while they were originally published with respect to ^{39}K [34, 88]. For the calculation of the isotope shift of the isomer ^{38m}K ($\delta\nu^{47,38m}$) the following isomer shifts, given in MHz, were used:

$$\begin{aligned} \delta\nu_{2010}^{38g,38m} &= -11.10(81) \\ \delta\nu_{2012}^{38g,38m} &= -10.98(77) \\ \delta\nu_{combined}^{38g,38m} &= -11.03(56). \end{aligned}$$

The systematic error for the isomer shift is negligible.

Table 5.2: Measured isotope shifts for the 2010 and 2012 data and the combined values. [1]from [88], [2]from [34];

A	I^π	$\delta\nu^{47,A}$ (MHz) 2010	$\delta\nu^{47,A}$ (MHz) 2012	$\delta\nu^{47,A}$ (MHz) Combined	$\delta\nu^{47,A}$ (MHz) Literature
37	$3/2^+$				$-1122.5(43)^1$
38m	0^+	$-997.05(95)[341]$	$-996.92(97)[341]$	$-996.99(68)[341]$	$-989.5(34)^1$
38g	3^+	$-985.94(49)[341]$	$-985.95(60)[341]$	$-985.95(38)[341]$	$-984.5(56)^2$
39	$3/2^+$	$-861.65(72)[296]$	$-863.48(76)[296]$	$-862.51(92)[296]$	$-857.5(17)^2$
40	4^-				$-731.9(17)^2$
41	$3/2^+$				$-622.3(19)^2$
42	2^-	$-507.16(38)[172]$	$-505.56(61)[172]$	$-506.72(71)[172]$	$-505.8(25)^2$
43	$3/2^+$				$-398.5(21)^2$
44	2^-	$-292.08(50)[98]$		$-292.08(50)[98]$	$-293.2(22)^2$
45	$3/2^+$				$-195.8(23)^2$
46	2^-	$-91.58(47)[31]$		$-91.58(47)[31]$	$-94.7(23)^2$
47	$1/2^+$	0	0	0	0
48	$1-$	$67.88(37)[31]$		$67.88(37)[31]$	
49	$1/2+$	$135.34(46)[60]$		$135.34(46)[60]$	
50	$0-$	$205.83(57)[88]$	$207.56(68)[87]$	$206.54(85)[88]$	
51	$3/2+$		$273.21(143)[114]$	$273.21(143)[114]$	

In general, the measured isotope shifts agree within their errors with the values found in literature whenever available. Two values exhibit larger discrepancies, the isotope shift of ^{39}K and the isomer ^{38m}K. In the case of ^{39}K, the reason can be explained by the change of reference isotope. As explained in the previous chapter, the isotope shifts had been extracted from our data using a voltage calibration based on the literature values. Since our data are referenced to the isotope ^{47}K, the isotope shifts given by Touchard

et al. [34] and referenced to ^{39}K had to be recalculated, see table 5.3. After the data analysis, it was found that the A-factors of the lower state A($S_{1/2}$) given in section 5.2.2 for ^{47}K show a large discrepancy. The literature value of the lower-state splitting A($S_{1/2}$) deviates by more than $2\,\sigma$ from our value. Since the isotope ^{47}K was used as reference during our experiments in 2010 and 2012, very good statistics were collected, and thus the reliability of our A-factor is high. The value from Touchard, on the other hand, was the most exotic isotope measured at that time. It is thus believed that the error in the value for ^{47}K from the data of Touchard *et al.* is underestimated and has to be taken with great care. Assuming that our A-factor is indeed the true value, the determination of the centroid of the hyperfine structure might be erroneous leading to a (slightly) deviating isotope shift. Without a spectrum of the measurement of Touchard *et al.* at hand, it is hard to judge by how much the centroid would shift. It is assumed that this could lead to a change in voltage of the voltage calibration of roughly 1 V. On the isotopes farthest away, ^{38}K, this would augment to a shift in frequency of about 1.5 MHz, which lies still within the systematic uncertainty. As a remedy, the to-date unavailable spectra from literature would have to be re-evaluated with our A-factor as a fixed parameter, which lies out of the scope of the present work.

Table 5.3: Isotope shifts found in literature referenced to ^{39}K and recalculated to ^{47}K . [1]from [88], [2]from [34];

A	I^π	$\delta\nu^{39,A}$ (MHz) Literature	$\delta\nu^{47,A}$ (MHz) Literature
37	$3/2^+$	$-265.0(40)^1$	$-1122.5(43)^1$
38m	0^+	$-132.0(30)^1$	$-989.5(34)^1$
38g	3^+	$-127.0(53)^2$	$-984.5(56)^2$
39	$3/2^+$	0^2	$-857.5(17)^2$
40	4^-	$125.58(26)^2$	$-731.9(17)^2$
41	$3/2^+$	$235.25(75)^2$	$-622.3(19)^2$
42	2^-	$351.7(19)^2$	$-505.8(25)^2$
43	$3/2^+$	$459.0(12)^2$	$-398.5(21)^2$
44	2^-	$564.3(14)^2$	$-293.2(22)^2$
45	$3/2^+$	$661.7(16)^2$	$-195.8(23)^2$
46	2^-	$762.8(15)^2$	$-94.7(23)^2$
47	$1/2^+$	$857.5(17)^2$	0

In the case of the isomer ^{38m}K, the discrepancy relates back to the one of ^{39}K. Behr *et al.* [88] give the isotope shift of ^{38m}K relative to ^{39}K. To relate this to our reference ^{47}K, the isotope shift of ^{39}K to ^{47}K from Touchard was used, as discussed above. If we calculate the isotope shift of ^{38m}K to ^{39}K from our results and compare this to the literature value the situation changes. Our value for $\delta\nu^{39,38m} = -134.47(1.14)$ MHz which agrees within the errors with the literature value $\delta\nu^{39,38m}_{Lit} = -132.0(3.0)$ MHz.

The results of the two experiments are consistent within the error bars, which is partly expected since the 2012 experiment was calibrated against the 2010 data.

Figure 5.6 shows samples of the fitted hyperfine spectra for the isotopes $^{47-51}$K. Also indicated in the graph is the position of the hyperfine centroids (vertical red lines) to illustrate the change of ν_{cg} with increasing number of neutrons.

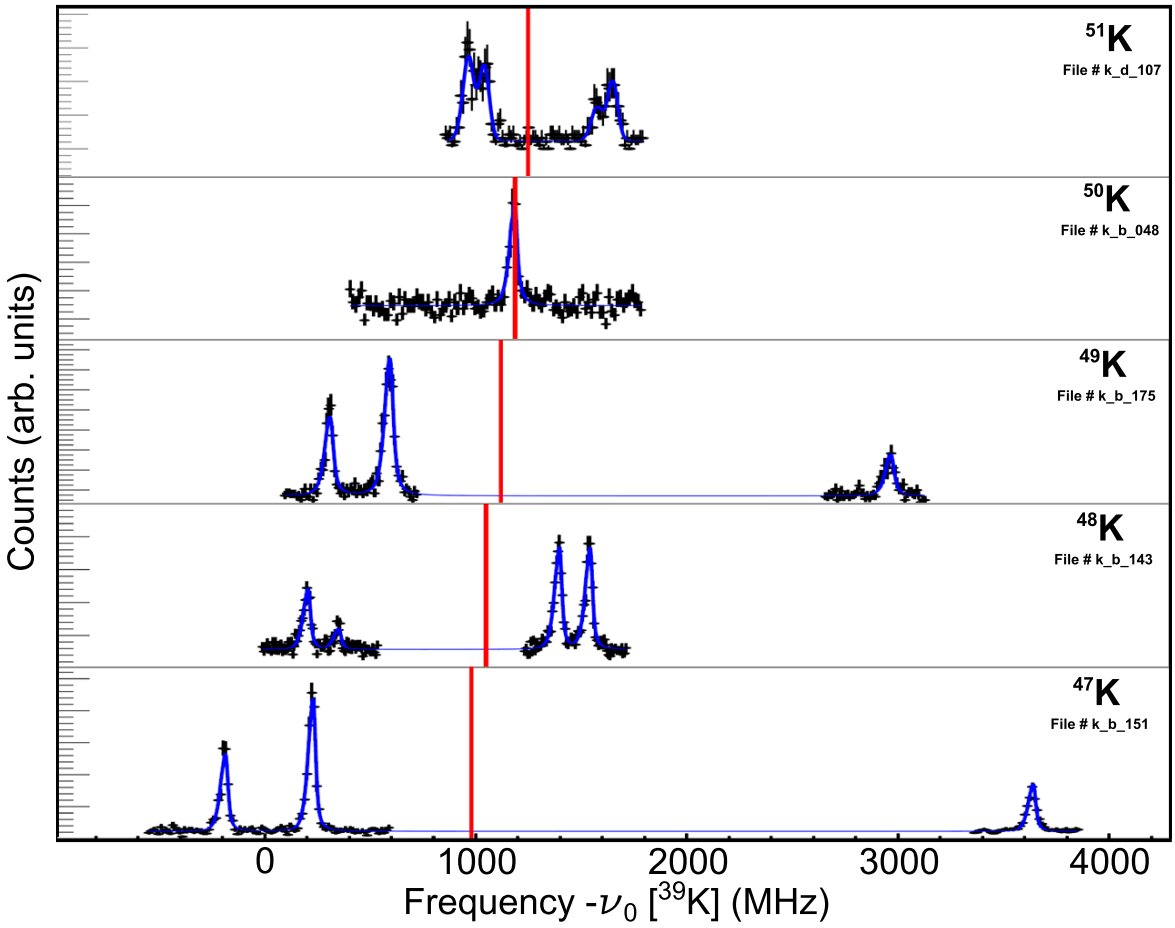

Figure 5.6: Fitted spectra of $^{47-51}$K with hyperfine centroid indicated (red line).

5.2.2 The A-Factors

The tables 5.4 and 5.5 give the final values of the A-factors for the lower state A($S_{1/2}$) and the upper state A($P_{1/2}$) of the hyperfine transition for the two experiments from 2010 and 2012. Also given are the literature values taken from [34] and references therein. The isotopes ^{38m,50}K with a ground-state spin $I = 0$ are not shown since they do not exhibit a hyperfine splitting and therefore have no A-factors.

The measured values of the lower state A($S_{1/2}$) and the upper state A($P_{1/2}$) of the two experiments from 2010 and 2012 agree with each other and the literature values within the error bars, except for ^{39}K and ^{47}K. The discrepancy of the values for ^{39}K results from the partly unresolved structure due to higher laser power and charge-exchange

Table 5.4: Measured A-factors A($S_{1/2}$) for the 2010 and 2012 data. Literature values are taken from [34] and references therein.

A	I^π	A($S_{1/2}$) (MHz) 2010	A($S_{1/2}$) (MHz) 2012	A($S_{1/2}$) (MHz) Literature
38g	3^+	404.36(28)	404.33(14)	404.369(3)
39	$3/2^+$	231.01(27)	231.91(39)	231.0(3)
42	2^-	−503.54(9)	−503.79(18)	−503.55078(1)
44	2^-	−378.71(15)		−378.1(11)
46	2^-	−462.82(14)		−465.1(12)
47	$1/2^+$	3412.87(19)	3412.36(43)	3420.2(29)
48	1^-	−795.84(29)		
49	$1/2^+$	2366.2(11)		
51	$3/2^+$		302.47(143)	

Table 5.5: Measured A-factors A($P_{1/2}$) for the 2010 and 2012 data. Literature values are taken from [34] and references therein.

A	I^π	A($P_{1/2}$) (MHz) 2010	A($P_{1/2}$) (MHz) 2012	A($P_{1/2}$) (MHz) Literature
38g	3^+	48.94(22)	48.72(14)	
39	$3/2^+$	27.77(27)	28.52(26)	27.5(4)
42	2^-	−61.18(16)	−60.86(19)	−60.6(16)
44	2^-	−45.80(16)		−44.9(11)
46	2^-	−55.87(13)		−55.7(13)
47	$1/2^+$	412.08(16)	412.28(32)	411.9(50)
48	1^-	−96.21(22)		
49	$1/2^+$	287.0(6)		
51	$3/2^+$		37.23(95)	

temperature used in the 2012 experiment, compare the spectra of ^{39}K in figures B.2 and 4.15 which are discussed in section 4.2.1. The remaining isotopes investigated in the 2012 experiment all exhibit significantly larger A-factors compared to ^{39}K and therefore a clear separation of the individual peaks of the hyperfine structure. The effect of higher laser power and charge-exchange temperature is thus less pronounced in these isotopes, which becomes obvious in the agreement of the A-factors from the two experiments. For a detailed comparison, the reader is referred to the spectra of ^{38,42,47,51}K of figures 4.15, 5.3 and B.3.

In the case of ^{47}K it is obvious that the lower state A-factor A($S_{1/2}$) deviates by more than $2\,\sigma$ from the literature value whereas the results from the two experiments agree with each other. The upper state A-factors A($P_{1/2}$) of ^{47}K in contrast agree within the errors. As mentioned before, ^{47}K was used as reference in our experiments and was

therefore recorded with highest statistics. The resulting A-factors are believed to be more accurate than the ones reported by Touchard as discussed above.

A combined value for the A-factors is not given since they are not used in the further analysis in contrast to the isotope shifts from which the changes in mean square charge radii are deduced, see next section.

5.3 Changes in Mean Square Charge Radii

As discussed in section 2.2 the changes in mean square charge radii $\delta\langle r^2\rangle^{AA'}$ can be calculated from the isotope shifts using Eq. (2.22). The values of the specific mass shift (K_{SMS}), the normal mass shift (K_{NMS}), and the electronic factor (F) have to be known for the calculation. The normal mass shift can be calculated from the mass of the electron (m_e) and the transition frequency (ν^A) of the reference isotope ($K_{NMS} = \nu^{47}\mathrm{m}_e$). It was calculated to $K_{NMS} = 213.55\,\mathrm{GHz\,u}$ using the D1-frequency of ^{39}K measured by Falke *et al.* [85] and the isotope shift measured relative to ^{47}K from our data ($\delta\nu^{47,39} = -862.51\,\mathrm{MHz}$).

Table 5.6: Changes in mean square charge radii calculated from the isotope shifts of the 2010 and 2012 data, and the combined values. The literature values are calculated from the isotope shifts using the same procedure as described for the measured data. [1]from [88], [2]from [34];

A	I^π	$\delta\langle r^2\rangle$ (fm^2) 2010	$\delta\langle r^2\rangle$ (fm^2) 2012	$\delta\langle r^2\rangle$ (fm^2) Combined	$\delta\langle r^2\rangle$ (fm^2) Literature
37	$3/2^+$				−0.163(40)[199][1]
38m	0^+	−0.025(9)[177]	−0.026(9)[177]	−0.026(6)[177]	−0.094(31)[174][1]
38g	3^+	−0.126(4)[177]	−0.126(5)[177]	−0.126(3)[177]	−0.139(51)[174][2]
39	$3/2^+$	−0.044(7)[153]	−0.028(7)[153]	−0.037(8)[153]	−0.082(15)[151][2]
40	4^-				−0.066(16)[129][2]
41	$3/2^+$				0.036(17)[108][2]
42	2^-	0.038(3)[89]	0.024(6)[89]	0.034(6)[89]	0.026(23)[88][2]
43	$3/2^+$				0.049(19)[69][2]
44	2^-	0.036(5)[51]		0.036(5)[51]	0.047(20)[50][2]
45	$3/2^+$				0.072(21)[33][2]
46	2^-	−0.002(4)[16]		−0.002(4)[16]	0.026(21)[16][2]
47	$1/2^+$	0	0	0	0
48	1^-	0.186(3)[16]		0.186(3)[16]	
49	$1/2^+$	0.342(4)[32]		0.342(4)[32]	
50	0^-	0.441(5)[47]	0.425(6)[47]	0.434(8)[47]	
51	$3/2^+$		0.538(13)[61]	0.538(13)[61]	

In the case of potassium the specific mass shift and the electronic factor have been calculated theoretically by Martensson-Pendrill *et al.* [35] to $K_{SMS} = -15.4(3.8)\,\mathrm{GHz\,u}$

and $F = -110(3)\,\mathrm{MHz\,fm^{-2}}$ and are used in the evaluation. Also needed for the calculation are the nuclear masses which were calculated using the atomic masses for $^{37-51}$K from the latest atomic mass evaluation (AME2012) [61] subtracting 19 electron masses m_e. The calculated $\delta\langle r^2\rangle^{47,A}$ are shown in Table 5.6. For the isotope shifts known from [34, 88] the same procedure was used to calculate the $\delta\langle r^2\rangle^{47,A}$ in order to obtain a consistent set of $\delta\langle r^2\rangle^{47,A}$ over the entire potassium chain. The statistical error on $\delta\langle r^2\rangle^{47,A}$ (round brackets) originates from the statistical error on the isotope shift while the systematic error (square brackets) is dominated by the uncertainty of K_{SMS}.

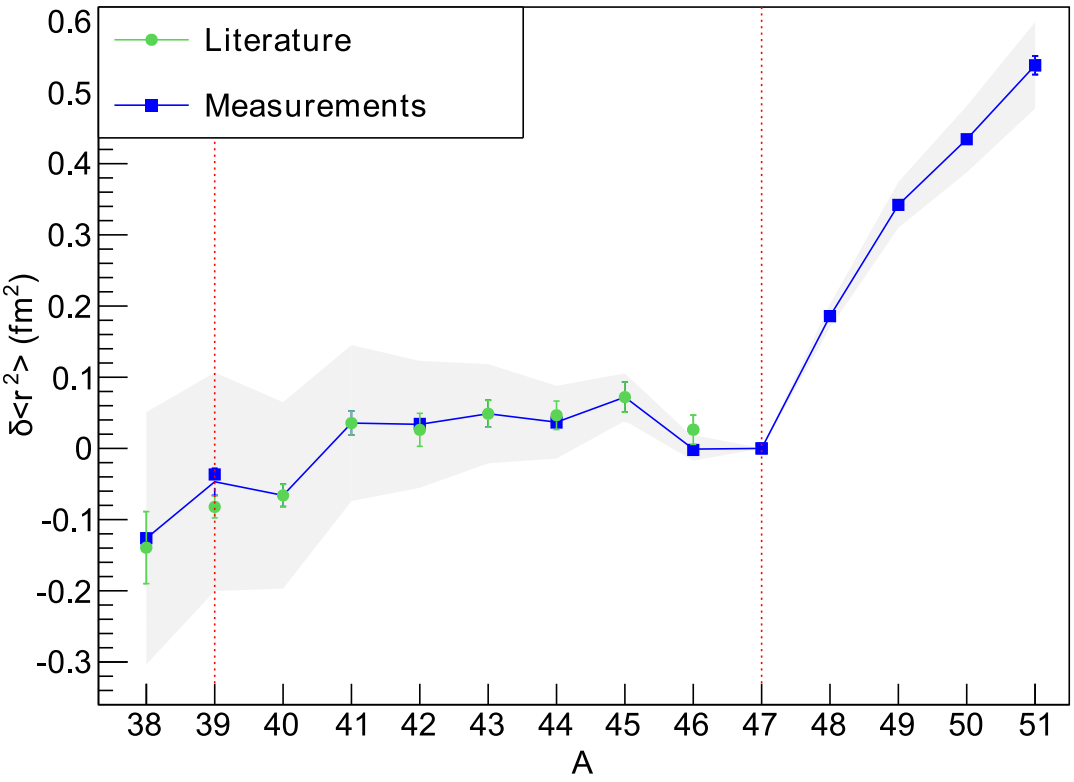

Figure 5.7: Changes in mean square charge radii as a function of A. Plotted are the combined values from our analysis and the literature values taken from table 5.6. The systematic error is given as gray-shaded area surrounding the trend. For details see text.

Figure 5.7 shows a plot of $\delta\langle r^2\rangle^{47,A}$ for the combined values and the literature values given in table 5.6. The solid line connects the weighted mean values of our combined values and the literature values. In the case where values from our measurements exist that value dominates the mean value due to smaller errors. The line illustrates the trend through the isotopes missing from our measurements. The correlated systematic errors of the measured values are indicated by the gray shaded area surrounding the trend. Also marked are the shell closures at $N = 20$ (^{39}K) and $N = 28$ (^{47}K) (dotted red vertical lines).

Prior to our measurements, changes in ms charge radii had been known up to ^{47}K. We re-measured partly the data for the isotopic chain from $^{38-47}$K and find agreement with the literature values. The discrepancies have been discussed in section 5.2.1 upon treatment of the isotope shifts. The new values comprise changes in ms charge radii for the isotopes $^{48-51}$K, see table 5.6 and figure 5.7. The shell closure at $N = 28$ is clearly visible in the steep rise of $\delta\langle r^2\rangle^{47,A}$ values for isotopes with $A > 47$. This strong effect of the shell closure at $N = 28$ is in contrast to the magic neutron number $N = 20$ where no shell closure is visible. A detailed discussion of the data in the context of the trends observed in the elements in the calcium region will be given in chapter 6.

5.4 Root Mean Square Charge Radii

From the changes in mean square charge radii $\delta\langle r^2\rangle^{47A}$ the absolute root mean square (rms) charge radii R can be calculated from a known reference radius using Eq. (2.23). For the potassium isotopes, the radius $R(^{39}K) = 3.435(17)$ fm from [89] was used for the calculation.

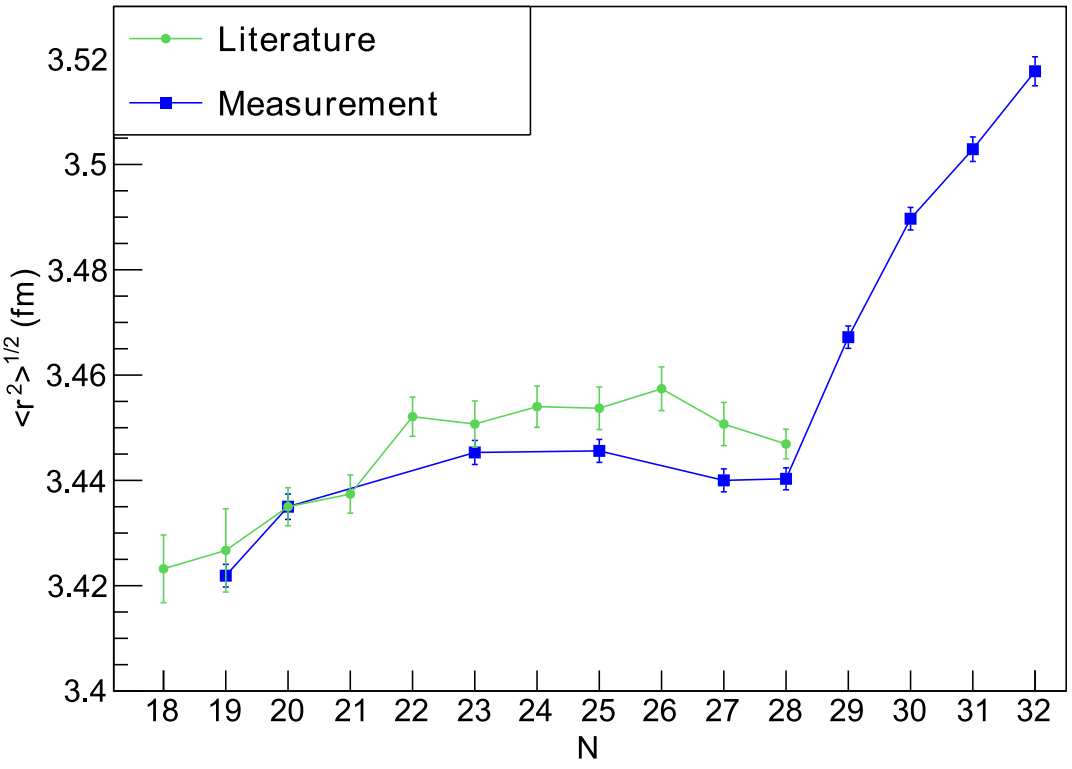

Figure 5.8: Root mean square charge radii as a function of N. Plotted are the combined values from our analysis and the literature values. For details see text.

Figure 5.8 shows the rms charge radii obtained from $\delta\langle r^2\rangle^{47,A}$ given in table 5.6 for the combined and the literature values. Only the statistical errors are shown. Compared to

figure 5.7 an offset of the literature values to our measurements is visible. It is recalled that the changes in ms charge radii were referenced to ^{47}K while the rms charge radii are referenced to ^{39}K. The problem with the isotope shift of ^{47}K from literature as discussed in section 5.2.1 causes this offset. A correction of this isotope shift would naturally diminish the offset. However, the overall trend is not affected.

For further discussion of the results, the combined values of our measurements and the literature values are used as weighted mean values in accordance with the trend line of figure 5.7. The $\delta\langle r^2\rangle$ and $\langle r^2\rangle^{1/2}$ are then calculated from the isotope shifts as described above. The results are given in table 5.7. For the rms charge radii the systematic error was not propagated since they are only used for the global comparison of the radii in the calcium region, see next chapter.

Table 5.7: Combined results of the isotope shift, changes in mean square charge radii and rms charge radii from our results and the literature data from [88] and [34].

A	I^π	$\delta\nu^{47A}$ (MHz)	$\delta\langle r^2\rangle$ (fm^2)	$\langle r^2\rangle^{1/2}$ (fm)
37	$3/2^+$	−1122.5(43)[38]	−0.163(40)[201]	3.4180(66)
38g	3^+	−985.9(4)[34]	−0.126(3)[177]	3.4234(33)
39	$3/2^+$	−861.4(21)[30]	−0.047(19)[153]	3.4350(43)
40	4^-	−731.9(17)[25]	−0.066(16)[131]	3.4322(39)
41	$3/2^+$	−622.3(19)[21]	0.036(17)[110]	3.4470(41)
42	2^-	−506.7(7)[17]	0.034(6)[89]	3.4467(34)
43	$3/2^+$	−398.5(21)[14]	0.049(19)[70]	3.4489(42)
44	2^-	−292.1(5)[10]	0.037(4)[51]	3.4472(33)
45	$3/2^+$	−195.8(23)[6]	0.072(21)[33]	3.4523(45)
46	2^-	−91.7(6)[3]	−0.001(6)[16]	3.4417(33)
47	$1/2^+$	0	0	3.4418(32)
48	1^-	67.9(4)[3]	0.186(3)[16]	3.4687(33)
49	$1/2^+$	135.3(5)[6]	0.342(4)[32]	3.4912(33)
50	0^-	206.5(9)[9]	0.434(8)[47]	3.5043(34)
51	$3/2^+$	273.2(14)[11]	0.538(13)[61]	3.5191(37)

6 Discussion

This chapter discusses the results presented in chapter 5. The spins and mean square charge radii of nuclear ground states in the potassium isotopic chain have been measured op to ^{51}K, a very exotic nucleus with a neutron-to-proton ratio of roughly 1.7. At such a high nucleon asymmetry it is not all obvious that the structural evolution be smooth. We rather expect sudden changes in nuclear ground-state properties. Keeping this in mind, section 6.1 discusses the evolution of the ground-state level in the potassium isotopes from the measured spins. Section 6.2 discusses the systematics of charge radii in the calcium region. Here, the mean square charge radii are discussed for an overview while the changes in mean square charge radii are analyzed applying the Zamick-Talmi formula [90–92]. In the last section, the results will be compared to two theoretical calculations arising from microscopic mean-field models.

6.1 Evolution of the $\pi d_{3/2}$ Level in Potassium

The spins measured in the context of this thesis complement the discussion on the evolution of the $\pi d_{3/2}$ orbital when filling the $\nu p_{3/2}$ orbital [48–54]. Figure 6.1 gives the configuration of the proton and neutron shells for neutron-rich potassium isotopes. Table 6.1 gives the spins for $^{47-51}$K together with the deduced ground-state configuration. The $\pi s_{1/2}$ orbital serves as ground state in ^{47,49}K. In ^{48}K the ground state spin 1^- results from the coupling of the valence proton in the $\pi s_{1/2}$ orbital with the valence neutron in the $\nu p_{3/2}$ orbital. In ^{50}K the inversion of the $\pi d_{3/2}$ and $\pi s_{1/2}$ is revoked resulting in a spin of 0^- from the coupling of the $\pi d_{3/2}$ with the $\nu p_{3/2}$ orbital. This level ordering stays when going to ^{51}K. Here the $\pi d_{3/2}$ orbital defines the ground state spin.

Table 6.1: Determined spins and ground states for $^{47-51}$K.

A	I^π Exp.	Ground-State Configuration
47	$1/2^+$	$\pi s_{1/2}$
48	1^-	$\pi s_{1/2}$; $\nu p_{3/2}$
49	$1/2^+$	$\pi s_{1/2}$
50	0^-	$\pi p_{3/2}$; $\nu p_{3/2}$
51	$3/2^+$	$\pi p_{3/2}$

It has been noted by Sorlin and Porquet [93] that adding neutrons in the $\nu f_{7/2}$ orbital induces an enhanced binding energy of the $\pi d_{3/2}$ orbital as compared to the $\pi s_{1/2}$ one. This effect is so strong that upon going from neutron number $N = 20$ to $N = 28$

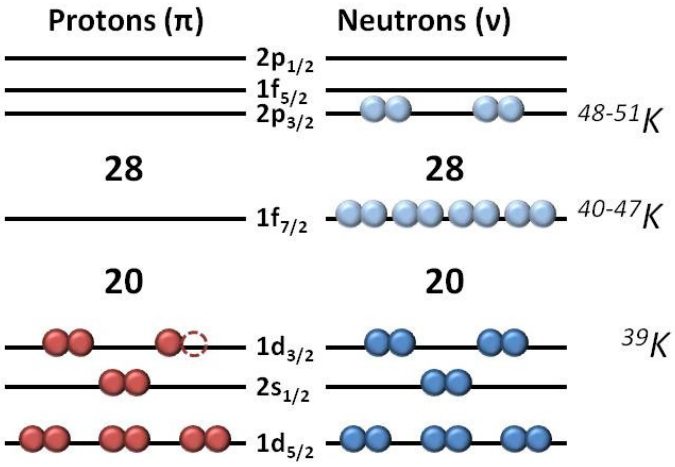

Figure 6.1: Configuration of the proton and neutron shells for neutron-rich potassium isotopes. With increasing neutron number, the $\nu f_{7/2}$ and $\nu p_{3/2}$ neutron levels are subsequently filled. The order of the proton $\pi s_{1/2}$ $\pi d_{3/2}$ orbitals is inverted for ^{47}K ($N = 28$), resulting in a hole in the $\pi s_{1/2}$ proton orbit instead of a hole in the $\pi d_{3/2}$ orbit.

energy gap between the two orbitals vanishes. Hartree-Fock, self-consistent calculations using the Gogny D1S interaction could reproduce a quasi-degeneracy of the $\pi d_{3/2}$ and $\pi s_{1/2}$ orbital (see figure 6 in reference above). Our data illustrate that the $\pi s_{1/2}$ orbital becomes the ground state at neutron number $N = 28$ and remains as such until $N = 30$. The $\pi d_{3/2}$ again acts as ground state at neutron numbers $N = 31, 32$. Recently, ab-initio calculations have become available using chiral effective field theory. In this approach, the nucleon-nucleon interaction is treated on a fundamental level involving the theory of quantum chromodynamics. Virtual excitations between the nucleon within a nucleus are explicitly considered up to a certain energy scale. The nuclear Hamiltonian can then be generated using different approaches, interesting in this context is that of the coupled-cluster method [94]. The extension of this description of the neutron-rich calcium isotopes, has led to predictions of the orbital evolution in the potassium isotopes. Using chiral interactions, it was possible to reproduce the level inversion in ^{47}K. Hagen and colleagues furthermore predicted the isotope ^{51}K to have the $\pi d_{3/2}$ orbital as the ground state [95]. The agreement of this prediction with our experimental findings points towards the predictive power of ab-initio methods at the forefront of nuclear-structure theory.

6.2 Charge Radii Systematic in the Calcium Region

Charge radii are extracted from the measured isotope shift and give us insight into the structural evolution along an isotopic chain. In a shell-model picture, nucleons are

expected to be more strongly bound at closed shells, which would result in a reduced charge radius at magic numbers. However, looking at experimental results we find that proton and neutron orbitals influence each other, in exotic systems even to the point where shell closures are no longer evident in the observables. In Figure 5.4 we compare the root mean square (RMS) charge radii $\langle r^2 \rangle^{1/2}$ of argon [25], calcium [28], scandium [30], titanium [33], chromium [37], manganese [36], iron [38], and potassium from this work. The trend of the radii in these isotopic chains below $N = 28$ has been discussed in [25, 30]. In this region $\delta \langle r^2 \rangle^{N,N'}$ displays a surprisingly strong dependence on Z with a general increasing N dependence for argon developing into a dominantly parabolic behavior in calcium and then progressing towards the anomalous downward sloping trends in scandium and titanium. Such dramatic variations of $\delta \langle r^2 \rangle^{N,N'}$ are not observed in the regions around $N = 50, 82$ and $N = 126$ [3, 39]. To date, although a range of approaches have shown some success in describing the observed trends for specific isotopic chains, no single theoretical model has fully described the strongly Z-dependent radii trends across the region [30].

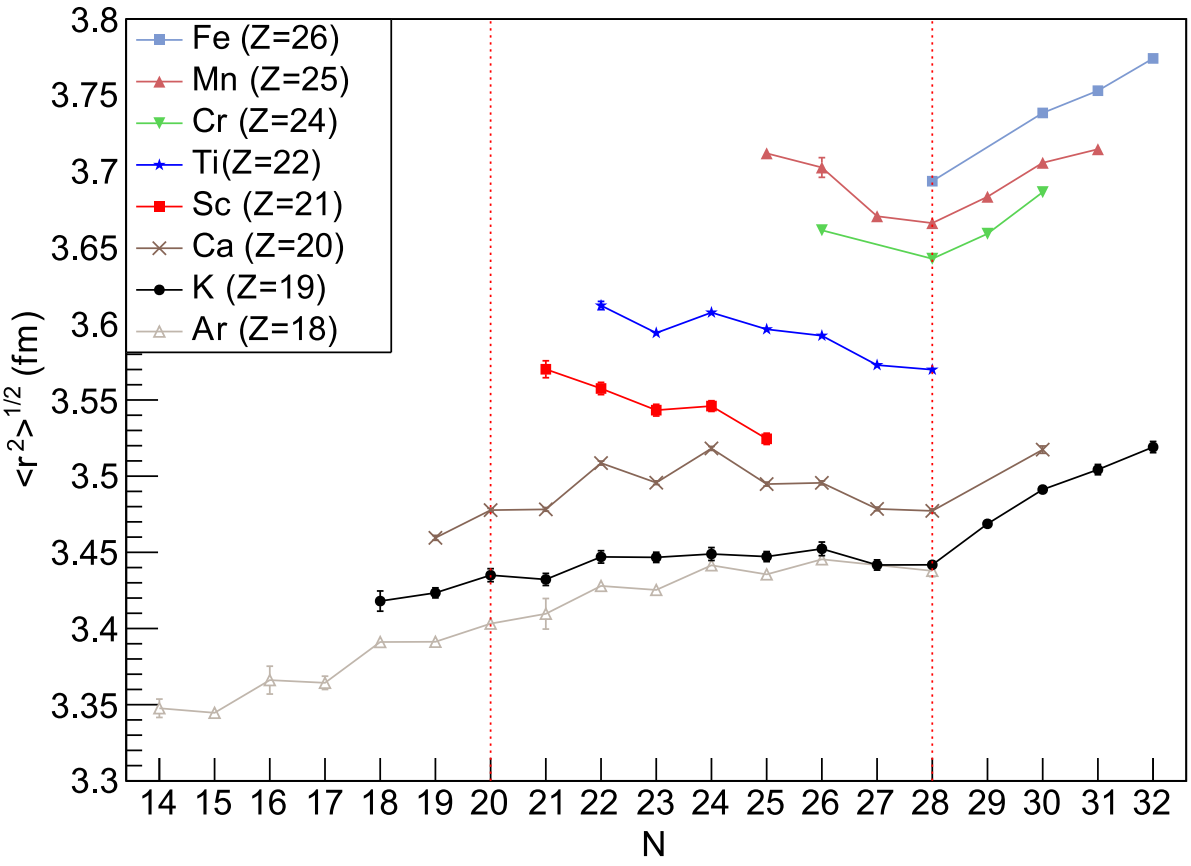

Figure 6.2: Root mean square charge radii as a function of N for the isotopes of of Ar, K, Ca, Sc, Ti, Cr, Mn, Fe, and K. For details see text.

Visible in the plot is the absence of a shell closure effect at the magic number $N = 20$

in argon, potassium and calcium as discussed in section 5.3. This behavior was discussed in [25] and is attributed to a cancellation of monopole and quadrupole polarization of the proton core under successive addition of valence neutrons. The shell effect at $N = 28$ in contrast is clearly visible in the trends of potassium, calcium, chromium, and manganese and will be discussed in the context of changes in the mean square charge radii.

6.2.1 Charge Radii in the Calcium Region between $N = 20$ and $N = 28$

The further discussion will be carried out looking at the changes in mean square charge radii. As discussed by Blaum *et al.* [25] one can fit the experimental data with the Zamick-Talmi formula [90–92]

$$\delta \left\langle r^2 \right\rangle^{20,20+n} = \left\langle r^2 \right\rangle^{20+n} - \left\langle r^2 \right\rangle^{20} = nC + \frac{n(n-1)}{2}\alpha + \left[\frac{n}{2}\right]\beta, \tag{6.1}$$

where $[n/2] = n/2$ for even n and $[n/2] = (n-1)/2$ for odd n. The parameter C expresses the one-body part of the effective charge radius operator, α includes the two-body part and β accounts for the odd-even effects. The parameters C, α and β given in table 6.2 were obtained by fitting Eq (6.1) to the data of Ar, Ca, Ti, Sc from the original publications cited above and for K the data are from table 5.7. The results obtained in the fits do not match the values given in [25] because the data were fitted including the statistical errors given in the publications. The parameters of Blaum *et al.* can be reproduced by performing fits without errors. In the case of Ti, the values given agree with our fit results, which are given without errors because the calculated errors were negligible. The results for Sc do not agree with the results given in [30] also if fitted without errors. We compare the results obtained from our analysis to have a consistent set of parameters.

Table 6.2: Results of the Zamick-Talmi fits between $N = 20$ and $N = 28$. Given are the parameters C, α and β for the elements Ar, K, Ca, Sc, Ti. For details see text.

Element	Z	C (fm^2)	α (fm^2)	β (fm^2)
Ar	18	0.023(9)	-0.018(1)	0.140(20)
K	19	0.024(34)	-0.014(5)	0.070(52)
Ca	20	0.003(12)	-0.033(3)	0.218(35)
Sc	21	-0.125(31)	-0.005(8)	0.160(18)
Ti	22	-0.018	-0.023	0.160

From the parameters one can see the trends described above. The parameter C describes the slope of the trend and is positive for Ar and K, almost zero for Ca and negative for Sc and Ti. Which illustrates the change from increasing to decreasing slope. The parabolic shape can be seen in α, which has the same sign for all five elements and

is biggest in Ca and smallest in Sc. The odd-even staggering is described by β. The effect is smallest in K and strongest in Ca.

6.2.2 Charge Radii in the Calcium Region Beyond $N = 28$

To discuss the new results for $N > 28$ we plot the changes in ms charge radii of potassium given in Table 5.7 from $N = 23$ to $N = 32$ together with the $\delta\langle r^2\rangle$ of Ar, Mn, Ca, Ti, Cr and Fe referenced to the $N = 28$ shell closure, see Figure 6.3. The correlated systematic errors in the potassium data are represented as gray shaded area surrounding the trend.

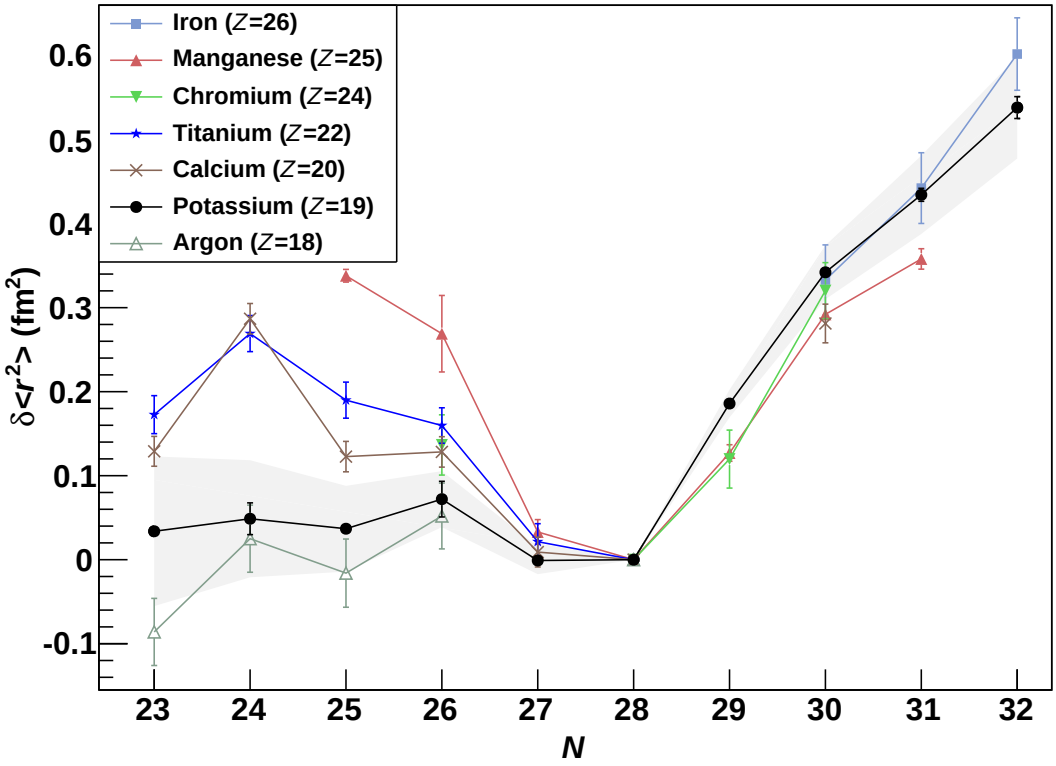

Figure 6.3: Difference in ms nuclear charge radii relative to $N = 28$ as a function of N for the isotopes of Ar, K, Ca, Ti, Cr, Mn and Fe.

Looking at the $\delta\langle r^2\rangle$ curves, one can see the above discussed Z dependence in the development of the radii in a broad structure below $N = 28$. Common in all elements is the strong shell closure effect at $N = 28$. Above $N = 28$ the $\delta\langle r^2\rangle$ values show a steep increasing slope similar for all elements meaning that almost no correlation to the number of protons is visible. The maximal deviation of the change in ms charge radii after the $N = 28$ shell closure is $0.08\,\mathrm{fm}^2$ between manganese and iron at $N = 31$. This value is comparable to the values in the $N = 50$ region. Here the maximal deviation of

$0.13\,\mathrm{fm}^2$ occurs for $N = 54$ between krypton and molybdenum (calculated using data for Kr, Rb, Sr and Mo from [96]). Below $N = 28$ the difference is $0.35\,\mathrm{fm}^2$ between argon and manganese at $N = 25$ illustrating the atypical Z dependence.

What changes at $N = 28$? Up to $N = 28$ the protons and neutrons in the calcium region ($18 \leq Z \leq 26$) occupy the same orbitals (sd and fp) resulting in a complex interplay of proton and neutron configurations. This fact is underlined by the work of [26]. They reproduce the radii trend (see Fig. 2. in [26]) in calcium between $N = 20$ and $N = 28$ by including multi-proton - multi-neutron excitations from the sd to the fp shell into the shell model calculation. Above $N = 28$ the neutrons fill the $2p_{3/2}$ shell. Here the changes in ms charge radii show little or no dependence on Z indicating that charge radii are purely driven by a common and collective polarization of the proton distribution by the neutrons in the $2p_{3/2}$ shell with little or no dependence on the specific proton configuration at the Fermi surface. This absence of strong proton configuration dependence is further emphasized by the consistency of the radii of the isotopes with inverted ground-state configuration ^{47,48,49}K with both the remaining K radii and all other measured radii in the region. Furthermore the changes in the ms radii of potassium show no indication for a shell closure at $N = 32$ as discussed in [42–44] for the calcium region. Theoretical and experimental evidence for a shell effect at $N = 32$ exists for Ca, Ti and Cr from the systematic of the excitation energies ($E_x(2_1^+)$) with the strongest effect in Ca [42, 44].

One can fit the Zamick-Talmi formula also to the changes in mean square radii beyond $N = 28$. The results are given in table 6.3. The change in the trends described above is also visible in the parameters of the fit. The slope described by C is positive and the large value indicates the steep increase after the shell closure. The value is similar for all four elements from K to Fe. The parabola and the odd-even staggering do not exhibit the strong variations seen between $N = 20$ and $N = 28$.

Table 6.3: Results of the Zamick-Talmi fits above $N = 28$. Given are the parameters C, α and β for the elements Ar, K, Ca, Sc, Ti. For details see text.

Element	Z	C (fm^2)	α (fm^2)	β (fm^2)
K	19	0.184(6)	-0.040(6)	0.015(17)
Cr	24	0.120(30)	-0.049(40)	0.134(40)
Mn	25	0.127(89)	-0.031(76)	0.069(91)
Fe	26	0.143(4)	-0.010(2)	0.041(10)

6.3 Comparison to Theory

The results of the mean square charge radii are compared to theoretical calculations performed by Goriely *et al.* [97] and Pena-Arteaga *et al.* [98]. Goriely *et al.* performed non relativistic Hartree-Fock-Bogoliubov calculations using Skyrme forces and Pena-Arteaga *et al.* performed relativistic mean-field calculations. Both calculations are based

on a microscopic description of the interaction between the nucleons within the nucleus using quantum mechanics. In this approach, the nuclear interaction is treated effectively in such a way that the nucleon-nucleon interactions are averaged to a mean field [99,100]. The ansatz for the effective interaction is based most commonly on the Skyrme force, which has a number of parameters requiring a fit to experimental data [101]. More recently, the Gogny force has been used in a similar way [102, 103]. Both models are global models developed to calculate masses. From these models charge radii can be extracted as well.

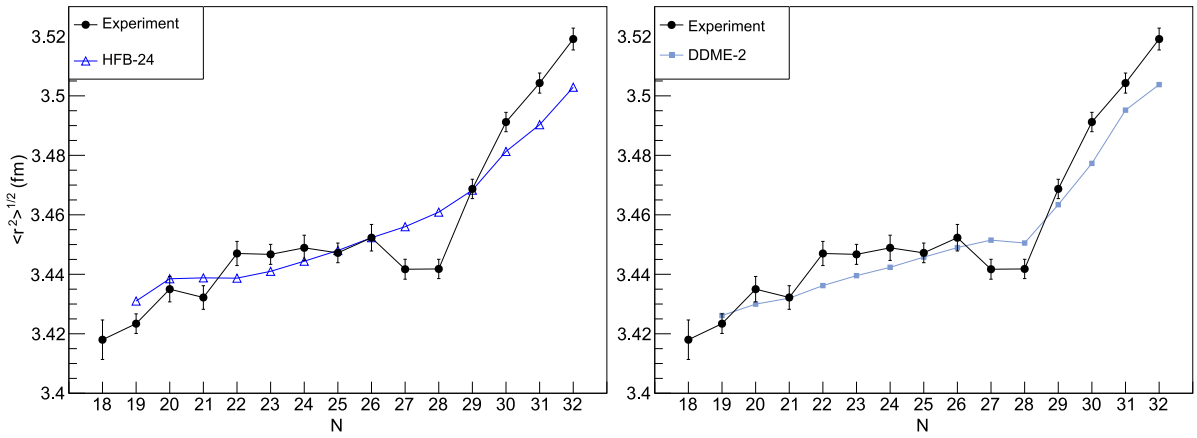

Figure 6.4: Mean square charge radii of potassium as a function of N compared to theoretical models. HFB-24 [97] in the left plot and DDME-2 [98] in the right. For details see text.

Figure 6.4 shows the radii calculated with these models together with the mean square charge radii from table 5.7. Both models describe the overall trend of the radii, but both fail to reproduce the underlying structure, the odd-even staggering and the parabolic shape. Additionally, the HFB-24 model produces radii that show no shell closure effect at $N = 28$, whereas the DDME-2 model produces radii which show a shell closure effect but the effect is not as pronounced as in the experimental data.

7 Summary and Outlook

Within this thesis measurements of the charge radii and ground state spins of $^{48-51}$K have been presented. The measurements were motivated by the discussion of the evolution of the ground state level in potassium and the evolution of the charge radii with increasing neutron number beyond $N = 28$.

The experiments were performed at the ISOLDE facility at CERN, using collinear laser spectroscopy to study radioactive nuclei produced by impact of a 1.4 GeV proton beam. The potassium isotopes were investigated with continuous-wave laser beams as neutral atoms in the 770 nm D1 transition from the ground state $4s\ ^2S_{1/2}$ to the lowest excited state $4p\ ^2P_{1/2}$. The newly developed light collection region was successfully installed, tested and modified for the measurements of the exotic isotope ^{51}K. The hyperfine structure and isotope shift measurements on $^{38,39,42,44,46-51}$K performed in the present work, give insight in the development of the ms charge radii in potassium beyond the $N = 28$ shell closure. Together with previous data on $^{37-47}$K [34,88], the studied isotopic chain of potassium ranges from neutron number N=18 to N=32 and covers the full $f_{7/2}$ and $p_{3/2}$ shells. The result contributes substantially to the systematics of ms nuclear radii in the calcium region beyond the $N = 28$ shell closure. The most striking effect is the different behavior of the difference in ms charge radii below and above $N = 28$.

The measured spins for $^{48-51}$K complement the discussion on the evolution of the $\pi d_{3/2}$ orbital while filling the $\nu p_{3/2}$ orbital. It was shown that the inversion of the ground state levels at $N = 28$ continues until $N = 30$ and that the re-inversion happens at $N = 31$ and stays for $N = 32$. The established region of inversion will contribute to the results of decay spectroscopy measurements by providing a firm spin determination for the identification of the newly found levels. The analysis of the magnetic moments of $^{48-51}$K deduced from the A-factors measured in the frame of this thesis are reported by Papuga *et al.* [104] and [105].

In comparison with theory, it could be shown that different models still have difficulties reproducing the fine structure in the behavior of the charge radii of the potassium isotopic chain. Looking at the mass of the potassium isotopes, a complementary nuclear ground-state property, we can observe a slightly different behavior. To extract structural information from the mass surface, usually the two-neutron separation energy is considered. This is the energy needed to remove the last two neutrons from a nucleus. The general trend of this quantity is also observed in the potassium chain: at neutron number 28 a sudden drop in the two-neutron separation energy of about 5 MeV marks this shell closure [61]. Recent measurements by the ISOLTRAP experiment have extended the isotopic chain to ^{53}K [106]. At neutron number $N = 32$, a similarly strong shell effect could be observed as in the semi-magic calcium chain [107]. This is in contradiction with the charge-radii measurements presented here, where no evidence for a new magic neutron

number at $N = 32$ could be obtained. Furthermore, the mass measurements have been compared to theoretical calculations using three-body forces, which are at the forefront of nuclear-structure theory. An ab initio calculation based on self-consistent Green's functions in the Gorkov formalism has been used where microscopic nuclear interactions are treated explicitly [108]. These calculations show a strong decrease in the two-neutron separation energy of both the calcium as well as the potassium isotopic chain at neutron number $N = 32$, which is consistent with the experimental findings [106]. This illustrates the importance of including two- and three-body nuclear interactions already at the fundamental level. If $N = 32$ were indeed a new magic number, it could still be that one observed another slope increase in the changes in ms charge radii in the potassium chain beyond $N = 32$.

The new light collection region was successfully used also for measurements of the cadmium isotopes and isomers $^{107-129}$Cd [109], the calcium isotopes $^{40-52}$Ca [110], and the manganese isotopes and isomers $^{51-64}$Mn [111]. The data for calcium are currently under analysis. Preliminary results agree with the trends in the radii observed in potassium beyond $N = 28$. New measurements on Ca up to $N = 34$ are planed [110] which will shed light on the discussed shell effect at $N = 32$.

A Basic Formulas for CLS

A.1 Relativistic Doppler Shift in CLS

Using the relativistic Energy increment $E - E_0 = Uq$, one obtains β with:

$$E = Mc^2; E_0 = M_0c^2; M = M_0\gamma = M_0/\sqrt{1 - \frac{\vec{v}^2}{c^2}}$$

in

$$\begin{aligned}
E - E_0 &= Uq \\
\frac{M_0c^2}{\sqrt{1 - \frac{\vec{v}^2}{c^2}}} - M_0c^2 &= Uq \\
\frac{M_0c^2}{\sqrt{1 - \frac{\vec{v}^2}{c^2}}} &= Uq + M_0c^2 \\
\frac{M_0^2c^4}{1 - \frac{\vec{v}^2}{c^2}} &= (Uq + M_0c^2)^2 \\
\frac{M_0^2c^4}{(Uq + M_0c^2)^2} &= 1 - \frac{\vec{v}^2}{c^2} \\
\frac{\vec{v}^2}{c^2} &= 1 - \frac{M_0^2c^4}{(Uq + M_0c^2)^2} \\
\beta = \frac{\vec{v}}{c} &= \sqrt{1 - \frac{M_0^2c^4}{(Uq + M_0c^2)^2}} \qquad \text{(A.1)}
\end{aligned}$$

U is the total acceleration voltage, q the charge of the ions and M_0 is their rest mass. Inserting Eq. (A.1) in eqp. 2.31 results in:

$$\nu = \nu_0 \frac{M_0^2c^4}{(Ue + M_0c^2)^2} \left(1 \pm \sqrt{1 - \frac{M_0^2c^4}{(Ue + M_0c^2)^2}}\right) \qquad \text{(A.2)}$$

B Raw Spectra from 2010 and 2012

B.1 Raw Spectra of ^{39,42,44}K from 2010

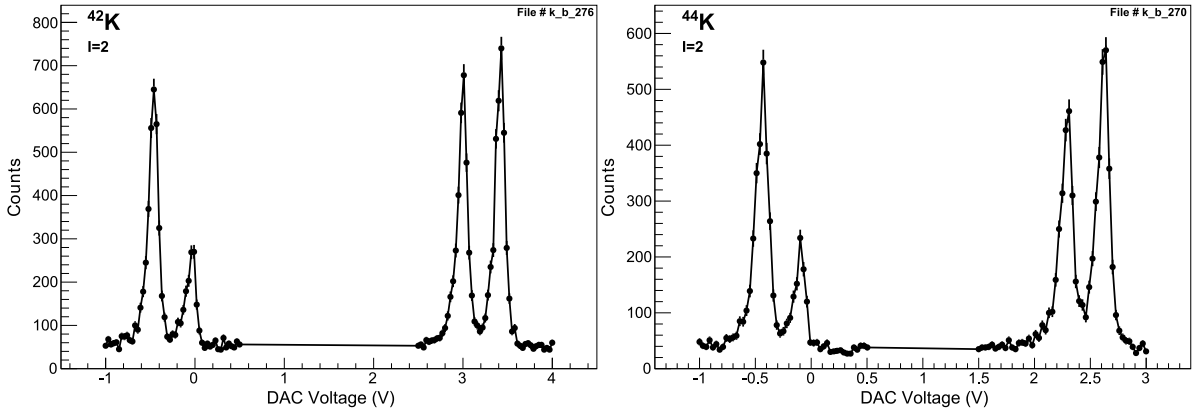

Figure B.1: Gated raw spectra of ^{42,44}K. Shown is the sum of the counts in all four PMTs as a function of the DAC voltage. The data points are connected to guide the eye.

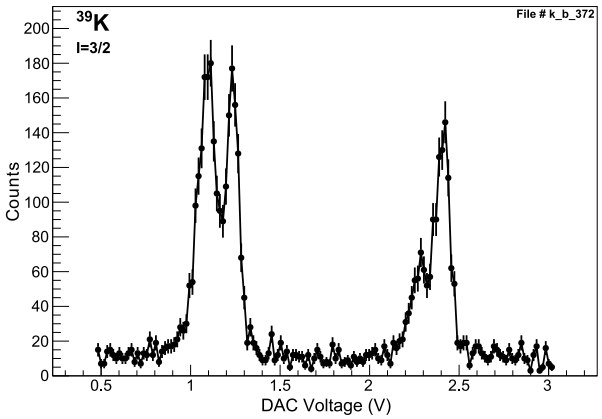

Figure B.2: Gated raw spectrum of ^{39}K. Shown is the sum of the counts in all four PMTs as a function of the DAC voltage. The data points are connected to guide the eye.

B.2 Raw Spectrum of ^{42}K from 2012

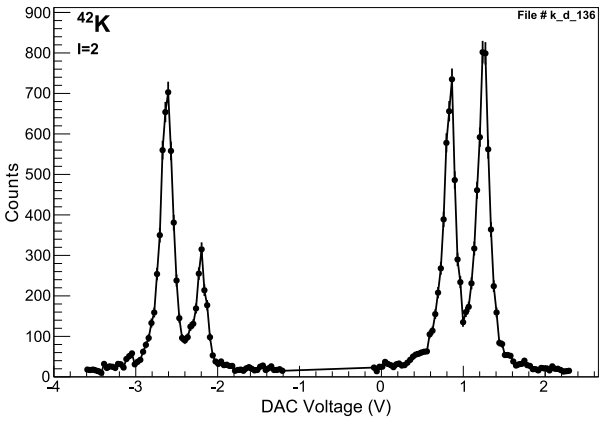

Figure B.3: Gated raw spectrum of ^{42}K. Shown is the sum of the counts in all four PMTs as a function of the DAC voltage. The data points are connected to guide the eye.

C Basic Settings used in the 2010 and 2012 Experiment

Table C.1 gives the full set of settings discussed in chapter 4 for all measured isotopes from the 2010 and 2012 experiments.

Table C.1: Basic settings used in the 2010 and 2012 experiments.

A	Gate Delay (μs)	Gate Width (μs)	# Bunches	Bunch Width (ms)	$U_{off}(\lambda_1)$ (V)	$U_{off}(\lambda_2)$ (V)
2010						
38	42	3.5	6	45		6230
39	41	7	6	45	5330	5330
42	42.5	6.5	6	45	2700	2800
44	43	8	6	45	980	
46	43	8	6	45	-790	
47	45	7	6	45	-1300	-1500
48	45	7	6	45	-2500	
49	47	4	6	45	-3300	
50	47.5	4	6	45	-4250	
2012						
38	42	3.5	4	100	6320	
39	41	7	7	60	5390	
42	42.5	6.5	7	60	2870	
47	46	4	7	60	-1470	
50	47.5	4	4	100	-4110	
51	48	4	2	100	-5000	

Bibliography

[1] R. Neugart, Laser spectroscopy on mass-separated radioactive beams. *Nuclear Instruments and Methods in Physics Research* **186**(1?2), 165 (1981).

[2] R. Neugart, Collinear laser spectroscopy on unstable isotopes - A tool of nuclear physics. *Hyperfine Interactions* **24**, 159 (1985).

[3] E. Otten, *Nuclear Radii and Moments of Unstable Isotopes*, vol. 8 of *Treatise on Heavy-Ion Science*, p. 517. Plenum Press, New York (1989).

[4] J. Billowes, P. Campbell, High-resolution laser spectroscopy for the study of nuclear sizes and shapes. *Journal of Physics G: Nuclear and Particle Physics* **21**(6), 707 (1995).

[5] W. Geithner, *et al.*, Measurement of nuclear moments and radii by collinear laser spectroscopy and by β-NMR spectroscopy. *Hyperfine Interactions* **129**, 271 (2000).

[6] R. Neugart, Lasers in nuclear physics - A review. *The European Physical Journal A - Hadrons and Nuclei* **15**, 35 (2002).

[7] H.-J. Kluge, W. Nörtershäuser, Lasers for nuclear physics. *Spectrochimica Acta Part B: Atomic Spectroscopy* **58**(6), 1031 (2003).

[8] R. Neugart, G. Neyens, *Nuclear Moments*, vol. 700 of *Lecture Notes in Physics*, chap. Nuclear Moments, pp. 135–189. Springer Berlin Heidelberg (2006).

[9] B. Cheal, K. T. Flanagan, Progress in laser spectroscopy at radioactive ion beam facilities. *Journal of Physics G: Nuclear and Particle Physics* **37**(11), 113101 (2010).

[10] H. J. Kluge, Atomic physics techniques for studying nuclear ground state properties, fundamental interactions and symmetries: status and perspectives. *Hyperfine Interactions* **196**, 295 (2010).

[11] W. Nörtershäuser, Recent developments in collinear laser spectroscopy at COLLAPS/ISOLDE. *Hyperfine Interactions* **198**, 73 (2010), 10.1007/s10751-010-0230-3.

[12] K. Blaum, *et al.*, Measurements of ground-state properties for nuclear structure studies by precision mass and laser spectroscopy. *Journal of Physics: Conference Series* **312**(9), 092001 (2011).

[13] K. Blaum, J. Dilling, W. Nörtershäuser, Precision atomic physics techniques for nuclear physics with radioactive beams. *Physica Scripta* **2013**(T152), 014017 (2013).

[14] *Laserspektroskopie von radioaktiven Isotopen - Übersicht*, http://www.uni-mainz.de/FB/Chemie/AK-Noertershaeuser/experiments/laserspectroscopy/survey.html (2013).

[15] W. D. Myers, K.-H. Schmidt, An update on droplet-model charge distributions. *Nuclear Physics A* **410**(1), 61 (1983).

[16] L.-B. Wang, *et al.*, Laser Spectroscopic Determination of the ^{6}He Nuclear Charge Radius. *Phys. Rev. Lett.* **93**, 142501 (2004).

[17] R. Sánchez, *et al.*, Nuclear Charge Radii of ^{9,11}Li: The Influence of Halo Neutrons. *Phys. Rev. Lett.* **96**, 033002 (2006).

[18] P. Mueller, *et al.*, Nuclear Charge Radius of ^{8}He. *Phys. Rev. Lett.* **99**, 252501 (2007).

[19] W. Nörtershäuser, *et al.*, Nuclear Charge Radii of ^{7,9,10}Be and the One-Neutron Halo Nucleus ^{11}Be. *Phys. Rev. Lett.* **102**(6), 062503 (2009).

[20] A. Krieger, *et al.*, Nuclear Charge Radius of ^{12}Be. *Phys. Rev. Lett.* **108**, 142501 (2012).

[21] W. Geithner, *et al.*, Masses and Charge Radii of $^{17-22}$Ne and the Two-Proton-Halo Candidate ^{17}Ne. *Phys. Rev. Lett.* **101**(25), 252502 (2008).

[22] K. Marinova, *et al.*, Charge radii of neon isotopes across the *sd* neutron shell. *Phys. Rev. C* **84**, 034313 (2011).

[23] F. Touchard, *et al.*, Electric quadrupole moments and isotope shifts of radioactive sodium isotopes. *Phys. Rev. C* **25**, 2756 (1982).

[24] D. T. Yordanov, *et al.*, Nuclear Charge Radii of $^{21-32}$Mg. *Phys. Rev. Lett.* **108**, 042504 (2012).

[25] K. Blaum, *et al.*, Nuclear moments and charge radii of argon isotopes between the neutron-shell closures $N = 20$ and $N = 28$. *Nuclear Physics A* **799**(1-4), 30 (2008).

[26] E. Caurier, K. Langanke, G. Martínez-Pinedo, F. Nowacki, P. Vogel, Shell model description of isotope shifts in calcium. *Phys. Lett. B* **522**(3?4), 240 (2001).

[27] C. W. P. Palmer, *et al.*, Laser spectroscopy of calcium isotopes. *Journal of Physics B: Atomic and Molecular Physics* **17**(11), 2197 (1984).

[28] L. Vermeeren, *et al.*, Ultrasensitive radioactive detection of collinear-laser optical pumping: Measurement of the nuclear charge radius of ^{50}Ca. *Phys. Rev. Lett.* **68**, 1679 (1992).

[29] A.-M. Martensson-Pendrill, *et al.*, Isotope shifts and nuclear-charge radii in singly ionized $^{40-48}$Ca. *Phys. Rev. A* **45**, 4675 (1992).

[30] M. Avgoulea, *et al.*, Nuclear charge radii and electromagnetic moments of radioactive scandium isotopes and isomers. *Journal of Physics G: Nuclear and Particle Physics* **38**(2), 025104 (2011).

[31] G. Lalazissis, A. Farhan, M. Sharma, Light nuclei near neutron and proton drip lines in relativistic mean-field theory. *Nuclear Physics A* **628**(2), 221 (1998).

[32] G. Lalazissis, S. Raman, P. Ring, Ground-State Properties of Even-Even Nuclei in the Reletivistic Mean-Field Theory. *Atomic Data and Nuclear Data Tables* **71**(1), 1 (1999).

[33] Y. P. Gangrsky, *et al.*, Nuclear charge radii of neutron deficient titanium isotopes ^{44}Ti and ^{45}Ti. *Journal of Physics G: Nuclear and Particle Physics* **30**(9), 1089 (2004).

[34] F. Touchard, *et al.*, Isotope shifts and hyperfine structure of $^{38-47}$K by laser spectroscopy. *Phys. Lett. B* **108**(3), 169 (1982).

[35] A. M. Martensson-Pendrill, L. Pendrill, A. Salomonson, A. Ynnerman, H. Warston, Reanalysis of the isotope shift and nuclear charge radii in radioactive potassium isotopes. *Journal of Physics B: Atomic, Molecular and Optical Physics* **23**(11), 1749 (1990).

[36] F. Charlwood, *et al.*, Nuclear charge radii of molybdenum fission fragments. *Phys. Lett. B* **674**(1), 23 (2009).

[37] I. Angeli, A consistent set of nuclear rms charge radii: properties of the radius surface $R(N, Z)$. *Atomic Data and Nuclear Data Tables* **87**(2), 185 (2004).

[38] D. M. Benton, E. C. A. Cochrane, J. A. R. Griffith, Optical isotope shifts in the iron atom. *Journal of Physics B: Atomic, Molecular and Optical Physics* **30**(23), 5359 (1997).

[39] I. Angeli, *et al.*, N and Z dependence of nuclear charge radii. *Journal of Physics G: Nuclear and Particle Physics* **36**(8), 085102 (2009).

[40] O. Haxel, J. H. D. Jensen, H. E. Suess, On the "Magic Numbers" in Nuclear Structure. *Phys. Rev.* **75**, 1766 (1949).

[41] M. G. Mayer, On Closed Shells in Nuclei. II. *Phys. Rev.* **75**, 1969 (1949).

[42] M. Honma, T. Otsuka, B. Brown, T. Mizusaki, Shell-model description of neutron-rich pf-shell nuclei with a new effective interaction GXPF 1. *The European Physical Journal A - Hadrons and Nuclei* **25**, 499 (2005), 10.1140/epjad/i2005-06-032-2.

[43] A. Gade, T. Glasmacher, In-beam nuclear spectroscopy of bound states with fast exotic ion beams. *Progress in Particle and Nuclear Physics* **60**(1), 161 (2008).

[44] O. Sorlin, M.-G. Porquet, Nuclear magic numbers: New features far from stability. *Progress in Particle and Nuclear Physics* **61**(2), 602 (2008).

[45] T. Otsuka, T. Suzuki, R. Fujimoto, H. Grawe, Y. Akaishi, Evolution of Nuclear Shells due to the Tensor Force. *Phys. Rev. Lett.* **95**(23), 232502 (2005).

[46] T. Otsuka, T. Matsuo, D. Abe, Mean Field with Tensor Force and Shell Structure of Exotic Nuclei. *Phys. Rev. Lett.* **97**(16), 162501 (2006).

[47] A. Gade, *et al.*, Evolution of the $E(1/2_1^+) - E(3/2_1^+)$ energy spacing in odd-mass K, Cl, and P isotopes for N = 20-28. *Phys. Rev. C* **74**, 034322 (2006).

[48] R. Broda, *et al.*, Proton-hole states in the $N = 30$ neutron-rich isotope ^{49}K. *Phys. Rev. C* **82**, 034319 (2010).

[49] F. Perrot, *et al.*, β-decay studies of neutron-rich K isotopes. *Phys. Rev. C* **74**, 014313 (2006).

[50] W. Królas, *et al.*, Coupling of the proton-hole and neutron-particle states in the neutron-rich ^{48}K isotope. *Phys. Rev. C* **84**, 064301 (2011).

[51] T. Burrows, Nuclear Data Sheets for A = 48. *Nuclear Data Sheets* **107**(7), 1747 (2006).

[52] L. Carraz, *et al.*, The 49K beta decay. *Phys. Lett. B* **109**(6), 419 (1982).

[53] P. Baumann, *et al.*, Meson-exchange enhancement in first-forbidden β transitions: The case of ^{50}K and ^{38}Ca. *Phys. Rev. C* **58**, 1970 (1998).

[54] H. Crawford, *et al.*, Beta-Decay Studies of Neutron-Rich Nuclei Near ^{52}Ca. *Acta Physica Polonica B* **40**(3), 481 (2009).

[55] H. Haken, H. Wolf, *Molekülphysik und Quantenchemie: Einführung in die experimentellen und theoretischen Grundlagen*. Springer, 8 edn. (2003).

[56] R. Kurucz, B. Bell, *Atomic Line Data Kurucz CD-ROM No. 23. Cambridge, Mass.: Smithsonian Astrophysical Observatory*, http://www.cfa.harvard.edu/amp/ampdata/kurucz23/sekur.html (1995).

[57] I. I. Sobelman, *Atomic Spectra and Radiative Transitions*. Springer (1996).

[58] R. D. Cowan, *The theory of atomic structure and spectra*, Los Alamos Series in Basic and Applied Sciences. Calif. Univ. Press, Berkeley, CA (1981).

[59] P. C. Magnante, H. H. Stroke, Isotope Shift between ^{209}Bi and 6.3-day ^{206}Bi. *J. Opt. Soc. Am.* **59**(7), 836 (1969).

[60] P. Aufmuth, K. Heilig, A. Steudel, Changes in mean-square nuclear charge radii from optical isotope shifts. *Atomic Data and Nuclear Data Tables* **37**(3), 455 (1987).

[61] M. Wang, *et al.*, The AME2012 atomic mass evaluation (II). *Chinese Physics C* **36**(12), 1603 (2012).

[62] S. Kaufman, High-resolution laser spectroscopy in fast beams. *Optics Communications* **17**(3), 309 (1976).

[63] W. H. Wing, G. A. Ruff, W. E. Lamb, J. J. Spezeski, Observation of the Infrared Spectrum of the Hydrogen Molecular Ion HD^+. *Phys. Rev. Lett.* **36**, 1488 (1976).

[64] P. Vingerhoets, *et al.*, Nuclear spins, magnetic moments, and quadrupole moments of Cu isotopes from $N = 28$ to $N = 46$: Probes for core polarization effects. *Phys. Rev. C* **82**(6), 064311 (2010).

[65] D. T. Yordanov, *From ^{27}Mg to ^{33}Mg: transition to the Island of inversion*, Ph.D. thesis, Katholieke Universiteit Leuven (2007).

[66] N. Bendali, H. T. Duong, P. Juncar, J. M. S. Jalm, J. L. Vialle, Na + -Na charge exchange processes studied by collinear laser spectroscopy. *Journal of Physics B: Atomic and Molecular Physics* **19**(2), 233 (1986).

[67] A. Klose, *et al.*, Tests of atomic charge-exchange cells for collinear laser spectroscopy. *Nuclear Instruments and Methods in Physics Research Section A: Accelerators, Spectrometers, Detectors and Associated Equipment* **678**(0), 114 (2012).

[68] F. Buchinger, *et al.*, Fast-beam laser spectroscopy on metastable atoms applied to neutron-deficient ytternium isotopes. *Nuclear Instruments and Methods in Physics Research* **202**(1-2), 159 (1982).

[69] A. Mueller, *et al.*, Spins, moments and charge radii of barium isotopes in the range $^{122-146}$Ba determined by collinear fast-beam laser spectroscopy. *Nuclear Physics A* **403**(2), 234 (1983).

[70] K. R. Anton, *et al.*, Collinear Laser Spectroscopy on Fast Atomic Beams. *Phys. Rev. Lett.* **40**, 642 (1978).

[71] B. Jonson, K. Riisager, The ISOLDE facility. *Scholarpedia* **5**(7), 9742 (2010).

[72] *The ISOLDE homepage*, http://isolde.web.cern.ch/ISOLDE/ (2013).

[73] E. Kugler, The ISOLDE facility. *Hyperfine Interactions* **129**(1-4), 23 (2000).

[74] A. Herlert, Laboratory Portrait: The ISOLDE Facility. *Nuclear Physics News International* **20**(4), 5 (2010).

[75] A. Jokinen, M. Lindroos, E. Molin, M. Petersson, RFQ-cooler for low-energy radioactive ions at ISOLDE. *Nuclear Instruments and Methods in Physics Research Section B: Beam Interactions with Materials and Atoms* **204**, 86 (2003), 14th International Conference on Electromagnetic Isotope Separators and Techniques Related to their Applications.

[76] I. Podadera, *et al.*, Design of a second generation RFQ Ion Cooler and Buncher (RFQCB) for ISOLDE. *Nuclear Physics A* **746**, 647 (2004), Proceedings of the Sixth International Conference on Radioactive Nuclear Beams (RNB6).

[77] H. Franberg, *et al.*, Off-line commissioning of the ISOLDE cooler. *Nuclear Instruments and Methods in Physics Research Section B: Beam Interactions with Materials and Atoms* **266**(19-20), 4502 (2008).

[78] E. Mané, *et al.*, An ion cooler-buncher for high-sensitivity collinear laser spectroscopy at ISOLDE. *The European Physical Journal A - Hadrons and Nuclei* **42**(3), 503 (2009).

[79] M. Bissell, Private communication (2013).

[80] R. Zinkstok, E. J. van Duijn, S. Witte, W. Hogervorst, Hyperfine structure and isotope shift of transitions in Yb I using UV and deep-UV cw laser light and the angular distribution of fluorescence radiation. *Journal of Physics B: Atomic, Molecular and Optical Physics* **35**(12), 2693 (2002).

[81] Coherent, *Operators Manual - The Coherent 899-21 Tinanium:Sapphire Ring Laser*.

[82] M. Schug, *Aufbau und Test einer phasensensitiven Laserfrequenz-Langzeitstabilisierung an COLLAPS*, Ph.D. thesis, Johannes Gutenberg-Universität Mainz (2009).

[83] Sirah, *Datasheet Matisse TS*, http://www.sirah.com/ (2013).

[84] *National Nuclear Data Center*, www.nndc.bnl.gov (2012).

[85] S. Falke, E. Tiemann, C. Lisdat, H. Schnatz, G. Grosche, Transition frequencies of the D lines of ^{39}K , ^{40}K , and ^{41}K measured with a femtosecond laser frequency comb. *Phys. Rev. A* **74**(3), 032503 (2006).

[86] J. G. Heinrich, *Coverage of Error Bars for Poisson Data*, CDF/MEMO/STATISTICS/PUBLIC/6438 (2003).

[87] R. Brun, F. Rademakers, ROOT - An object oriented data analysis framework. *Nuclear Instruments and Methods in Physics Research Section A: Accelerators, Spectrometers, Detectors and Associated Equipment* **389**(1-2), 81 (1997), See also http://root.cern.ch/.

[88] J. A. Behr, *et al.*, Magneto-optic Trapping of β-Decaying $^{38}\mathrm{K}^m$, $^{37}\mathrm{K}$ from an on-line Isotope Separator. *Phys. Rev. Lett.* **79**, 375 (1997).

[89] K. H. G. Fricke, *Nuclear Charge Radii*, Landolt-Börnstein: Numerical Data and Functional Relationships in Science and Technology - New Series, Vol. 20. Springer (2004).

[90] L. Zamick, Two body contribution to the effective radius operator. *Annals of Physics* **66**(2), 784 (1971).

[91] I. Talmi, On the odd-even effect in the charge radii of isotopes. *Nuclear Physics A* **423**(2), 189 (1984).

[92] L. Zamick, Relation between a three-parameter formula for isotope shifts and staggering parameters. *Phys. Rev. C* **82**, 057304 (2010).

[93] O. Sorlin, M.-G. Porquet, Evolution of the N = 28 shell closure: a test bench for nuclear forces. *Physica Scripta* **2013**(T152), 014003 (2013).

[94] G. Hagen, M. Hjorth-Jensen, G. R. Jansen, R. Machleidt, T. Papenbrock, Evolution of Shell Structure in Neutron-Rich Calcium Isotopes. *Phys. Rev. Lett.* **109**, 032502 (2012).

[95] G. Hagen, Private communication (2013).

[96] *Database of the Lomonosov Moscow State University, Skobeltsyn Institute of Nuclear Physics*, http://cdfe.sinp.msu.ru/services/radchart/radmain.html (2012).

[97] S. Goriely, N. Chamel, J. Pearson, submitted. *Phys. Rev. C* (2130).

[98] D. Pena-Arteaga, S. Goriely, Private communication (2013).

[99] M. Bender, P.-H. Heenen, P.-G. Reinhard, Self-consistent mean-field models for nuclear structure. *Rev. Mod. Phys.* **75**, 121 (2003).

[100] S. Goriely, F. Tondeur, J. Pearson, A Hartree-Fock Nuclear Mass Table. *Atomic Data and Nuclear Data Tables* **77**(2), 311 (2001).

[101] T. Skyrme, CVII The nuclear surface. *Philosophical Magazine* **1**(11), 1043 (1956).

[102] J. Dechargé, D. Gogny, Hartree-Fock-Bogolyubov calculations with the $D1$ effective interaction on spherical nuclei. *Phys. Rev. C* **21**, 1568 (1980).

[103] S. Goriely, S. Hilaire, M. Girod, S. Péru, First Gogny-Hartree-Fock-Bogoliubov Nuclear Mass Model. *Phys. Rev. Lett.* **102**, 242501 (2009).

[104] J. Papuga, *et al.*, Spins and Magnetic Moments of ^{49}**K** and ^{51}**K**: Establishing the $1/2^+$ and $3/2^+$ Level Ordering Beyond N=28. *Phys. Rev. Lett.* **110**, 172503 (2013).

[105] J. Papuga, Ph.D. thesis, Katholieke Universiteit Leuven, In preparation.

[106] S. Kreim, Private communication (2013).

[107] F. Wienholtz, *et al.*, In press (2013).

[108] V. Somà, T. Duguet, C. Barbieri, *Ab initio* self-consistent Gorkov-Green's function calculations of semimagic nuclei: Formalism at second order with a two-nucleon interaction. *Phys. Rev. C* **84**, 064317 (2011).

[109] D. T. Yordanov, *et al.*, Spins, Electromagnetic Moments, and Isomers of $^{107\text{-}129}$Cd. *Phys. Rev. Lett.* **110**, 192501 (2013).

[110] M. L. Bissell, *et al.*, Spins, Moments and Charge Radii Beyond ^{48}Ca. *CERN-INTC-2011-049* pp. INTC–P–313 (2011).

[111] B. Cheal, *et al.*, Collinear laser spectroscopy of manganese isotopes using optical pumping in ISCOOL. (CERN-INTC-2010-073. INTC-P-286) (2010).

Acknowledgements

First of all, I would like to thank my supervisor Klaus Blaum for offering me the possibility to work at CERN and for his constant support during that time.

Furthermore, thanks to Deyan Yordanov and Mark Bissell for their support, advice and suggestions during the experiments, analysis of the data, proof reading of this thesis and for many fruitful discussions about physics and many other topics. Working with you made life at CERN a great experience.

Special thanks to Rainer Neugart, who knows COLLAPS like nobody else, for his advice and support during the experiments, data analysis and writing of this thesis.

I would like to thank the COLLAPS collaboration for supporting the experiment. Special thanks to Gerda Neyens for her support of the potassium experiment. Thanks to the "Mainzer", Wilfrid Nörtershäuser, Christopher Geppert, Rodolfo Sanchez-Alacron, Andreas Krieger, Michael Hammen und Nadja Frömmgen for their support and a very nice atmosphere during many successful runs at COLLAPS. Thanks as well to Jasna Papuga and Hanne Heylen for their support during the potassium experiments and the discussion during the analysis of the data.

I would like to thank the local ISOLTRAP group for many discussions and activities at and outside of CERN.
Thanks to the ISOLDE Technical Group for helping and supporting the experiments and keeping ISOLDE running. Thanks also to the ISOLDE Physics Group for providing a stimulating environment at CERN.
Special thanks to Magdalena Kowalska for her support during the experiments and as physics coordinator for her flexibility in the schedule.

Ein großer Dank geht an meine Eltern und Schwiegereltern, die mich in der Zeit am CERN immer unterstützt und bestärkt haben, auch wenn es nicht leicht war.

Ein besonderer Dank geht an meine Tochter Magdalena, Du hast mich oft daran erinnert, dass auch die kleinen Dinge furchtbar interessant sein können. "Merci beaucoup!"

Danken möchte ich meiner Frau Susanne: ohne Deine Unterstützung während der gesamten Zeit wäre diese Arbeit nicht möglich gewesen.